8-23-2019

# Point Spread Function and Modulation Transfer Function Engineering

Jacob Wirth
jhw3864@rit.edu

# Point Spread Function and Modulation Transfer Function Engineering

by

Jacob Wirth

B.A. State University of New York at Geneseo, 2014

A dissertation submitted in partial fulfillment of the
requirements for the degree of Doctor of Philosophy
in the Chester F. Carlson Center for Imaging Science
College of Science
Rochester Institute of Technology

August 23, 2019

Signature of the Author _____

Accepted by _____
Coordinator, Ph.D. Degree Program Date

CHESTER F. CARLSON CENTER FOR IMAGING SCIENCE
COLLEGE OF SCIENCE
ROCHESTER INSTITUTE OF TECHNOLOGY
ROCHESTER, NEW YORK

CERTIFICATE OF APPROVAL

---

Ph.D. DEGREE DISSERTATION

---

The Ph.D. Degree Dissertation of Jacob Wirth
has been examined and approved by the
dissertation committee as satisfactory for the
dissertation required for the
Ph.D. degree in Imaging Science

Dr. Grover Swartzlander, Dissertation Advisor

Dr. Stefan Preble, External Chair

Dr. Zoran Ninkov

Dr. Abbie Watnik

Date

DISSERTATION RELEASE PERMISSION
ROCHESTER INSTITUTE OF TECHNOLOGY
COLLEGE OF SCIENCE
CHESTER F. CARLSON CENTER FOR IMAGING SCIENCE

Title of Dissertation:

**Point Spread Function and Modulation Transfer Function Engineering**

I, Jacob Wirth, hereby grant permission to Wallace Memorial Library of R.I.T. to reproduce my thesis in whole or in part. Any reproduction will not be for commercial use or profit.

Signature _____

Date

# Point Spread Function and Modulation Transfer Function Engineering

by

Jacob Wirth

Submitted to the
Chester F. Carlson Center for Imaging Science
in partial fulfillment of the requirements
for the Doctor of Philosophy Degree
at the Rochester Institute of Technology

## Abstract

A novel computational imaging approach to sensor protection based on point spread function (PSF) engineering is designed to suppress harmful laser irradiance without significant loss of image fidelity of a background scene. PSF engineering is accomplished by modifying a traditional imaging system with a lossless linear phase mask at the pupil which diffracts laser light over a large area of the imaging sensor. The approach provides the additional advantage of an instantaneous response time across a broad region of the electromagnetic spectrum. As the mask does not discriminate between the laser and desired scene, a post-processing image reconstruction step is required, which may be accomplished in real time, that both removes the laser spot and improves the image fidelity.

This thesis includes significant experimental and numerical advancements in the determination and demonstration of optimized phase masks. Analytic studies of PSF engineering systems and their fundamental limits were conducted. An experimental test-bed was designed using a spatial light modulator to create digitally-controlled phase masks to image a target in the presence of a laser source. Experimental results using already known

phase masks: axicon, vortex and cubic are reported. New methods for designing phase masks are also reported including (1) a numeric differential evolution algorithm, (2) a PSF reverse engineering method, and (3) a hardware based simulated annealing experiment. Broadband performance of optimized phase masks were also evaluated in simulation. Optimized phase masks were shown to provide three orders of magnitude laser suppression while simultaneously providing high fidelity imaging a background scene.

## Acknowledgements

I would like to first acknowledge the Office of Naval Research for supporting this research. This work was also supported by the Chester F. Carlson Center for Imaging Science at the Rochester Institute of Technology. I would also like to acknowledge American Society for Engineering Education who provided the support allowing me to conduct this work at the Naval Research Laboratory through the Naval Research Enterprise Internship Program.

I am eternally grateful to all the individuals who gave me their time throughout this process. First I would like to thank my advisers: Grover Swartzlander and Abbie Watnik. You both challenged and supported me over the past 5 years. I am truly a better researcher and scientist because of you and I hope to make you both proud with my future accomplishments. I also thank the remainder of my dissertation committee, Zoran Ninkov and Stefan Preble, for their counsel and encouragement. I would also like to thank those who helped me during my temporary internships at the Naval Research Laboratory including Colin Olson and Tim Doster. I would also like to thank the collaborators of this work Erin Fleet and Kyle Novak for many fruitful conversations.

Thank you to my friends and labmates who provided many words of encouragement and laughter. Thank you to my Mom and Dad who supported me in both my accomplishments and failures and who gave me every opportunity to succeed. Finally I am thankful to Maxine who helped make me the best version of myself.

# List of Figures

# List of Tables

# List of Acronyms

**BS** Beam Splitter.

**CCD** Charge-Coupled Device.

**DEA** Differential Evolution Algorithm.

**FT** Fourier Transform.

**GIQE** General Image Quality Equation.

**LC** Liquid Crystal.

**LCOS** Liquid Crystal on Silicon.

**LED** Light Emitting Diode.

**LF** Laserline Filter.

**LSR** Light Suppression Ratio.

**MTF** Modulation Transfer Function.

**NG** Noise Gain.

**NIIRS** National Imagery Interpretability Rating Scale.

**NM** Nelder Mead.

**OTF** Optical Transfer Function.

**PSF** Point Spread Function.

**PTF** Phase Transfer Function.

**RER** Relative Edge Response.

**SF** Spatial Filter.

**SLM** Spatial Light Modulator.

**SNR** Signal to Noise Ratio.

# Contents

# Chapter 1

# Background

## 1.1 Motivation

Since the invention of the laser, there has been concern over its potential to damage and disrupt sensors. For decades, research has been conducted on more compact systems and increasing laser powers including the infamous "Star Wars" strategic defense initiative [1,2]. While in the past the dream of laser weapons have been out of reach, systems have now had successful field tests are now being developed for deployment [3]. The HELIOS program is set to be deployed as soon as 2020 with a power of up to 150 kW - capable of dazzling or damaging imaging sensors more than 3 km away [4, 5]. As laser powers continue to grow, a proliferation of laser weapons should be expected.

As these laser systems become increasingly common, effective countermeasures are necessary for protecting sensors from potential dazzle and damage. Traditional methods for attenuating high intensity lasers in the laboratory such as neutral density filters, bandpass filters, polarizers, or mechanical shutters will equally affect the background scene, require prior knowledge of the laser's wavelength or polarization state, or required detection of

the laser. Coronagraphs, useful for imagining dim exoplanets near a bright overwhelming star, require accurate pointing [6–8]. Mechanisms for deflecting potentially damaging or dazzling laser light using micro mirror devices have been developed, but are bulky and require prior detection of the laser [9, 10]. Optical limiters provide a promising method of laser suppression [11–27]. Such devices leverage nonlinear transmission of materials to limit laser throughput. However, optical limiters have limited spectral bandpass, a nonzero response time, and can degrade the image. New methods are necessary to overcome these issues.

This thesis describes a novel computational imaging approach to sensor protection based on point spread function (PSF) engineering. A mask is introduced to the pupil plane of a traditional imaging system which redistributes the incident laser beam over a larger area of the sensor reducing the peak irradiance and effectively protecting the sensor from damage. As the mask does not discriminate between harmful laser radiation and the desired scene, a post-processing step is required to remove saturated pixels and restore the image.

PSF engineering has been used for improving and adding functionality to imaging systems. Coded apertures using binary patterns have been studied for reducing the affects of aberrations on imaging systems and improving optical resolution [28–31]. More recently, the use of phase-only masks have been used to modify the PSF without affecting the throughput of the imaging system. Phase masks have been demonstrated to extend the depth of field of an imaging system [32–35] and to encode 3D information using rotating PSFs [36–41].

Linear phase elements are capable of providing instantaneous laser suppression over a large bandwidth of the electro-magnetic spectrum. High damage threshold phase elements have been reported for glass and liquid crystal devices [42–50] . Other promising

subwavelength patterned surfaces include polarization diffraction gratings and metasurfaces [51–57]. Each of these have been implemented for designing mask with arbitrary phase patterns.

A desirable point spread function has a low peak amplitude and retains a high amount of information from the scene. These qualities are often considered a trade-off from one another, but this work has found that PSFs with the same peak amplitude can have vastly different fidelity of restored images. This thesis includes significant experimental and numerical advancements in the determination and demonstration of optimized phase masks. Analytic studies of PSF engineering systems in terms of the integrated Strehl ratio with fundamental limits are found. An experimental test-bed was designed to validate imaging performance using a spatial light modulator to create digitally-controlled phase masks to image a target in the presence of a laser source. Experimental results using already known phase masks: axicon, vortex and cubic are reported. Numeric and analytic approaches were taken to optimize the phase mask and PSF including (1) a numeric differential evolution algorithm, (2) a PSF reverse engineering method, and (3) a hardware based simulated annealing experiment. The PSF reverse engineering method was especially successful providing a new family of PSFs: half-ring PSFs which resulted in the highest imaging fidelity relative to level of laser suppression. Broadband performance of optimized phase masks were also evaluated in simulation. Optimized phase masks were experimentally shown to provide three orders of magnitude laser suppression while simultaneously providing high fidelity imaging a background scene.

## 1.2 Fourier Optics

We consider an imaging system as depicted in Fig. 1.1 comprising an incoherently illuminated object or scene, a lens of focal length $f$ and aperture function $A(x, y)$, and a sensor in the image plane. A phase mask having transmittance function $t(x, y)$ is placed at the entrance face of the lens. Superimposed upon the scene is a laser source which diffracts over free space to form a planar wavefront at the entrance face of the lens. Both the scene distance $z$ and the characteristic laser diffraction length $z_R$ are assumed to be much greater than the focal length $f$. For a non-uniform phase mask (e.g., $t(x, y) \neq 1$) the point spread function of the imaging system becomes blurred or distorted, thereby reducing the risk of damage to the focal plane sensor. For a well-designed phase mask, the blurred image of scene can be reconstructed using deconvolution post-processing techniques. The objective of this research is to determine a means of spreading the laser power across a large area, thereby reducing the risk of damage, while simultaneously being able to restore a high fidelity.

The PSF of the system, $h(x', y')$, is the Fourier transform of the pupil of the system

$$h(x', y') = FT[A(x, y)t(x, y)] = \int_{-\infty}^{\infty}\int_{-\infty}^{\infty} A(x, y)t(x, y) \times exp[-i\frac{2\pi}{\lambda f}(x'x + y'y)]dxdy \quad (1.1)$$

where $\lambda$ is the wavelength of light. The incoherent PSF is $|h(x', y')|^2$. Below we assume the maximum value of $A(x, y)$ and $|t(x, y)|$ is unity.

The coherent field at the image plane, $U_l'(x', y')$, is a convolution of the geometric field,

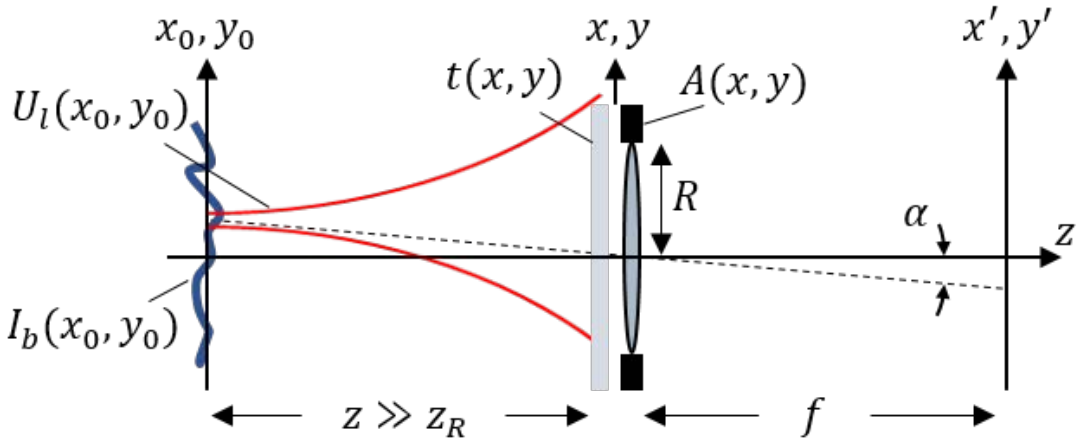


Figure 1.1: Basic PSF engineered imaging system schematic. A distant scene comprised of an incoherent background intensity, $I_b(x_0, y_0)$, and coherent laser field, $U_l(x_0, y_0)$ is imaged with a lens of aperture radius $R$ having an adjacent pupil plane mask $t(x, y)$. The resulting detected image is blurred and is restored in post-processing.

$U_l(x', y')$, and the coherent PSF

$$U_l'(x', y') = \int\int U_l(u, v)h(u - x', v - y')dudv = U_l(x', y') \otimes h(x', y') \tag{1.2}$$

The same is true for the geometric image of the background scene $I_b(x', y')$, and incoherent PSF.

$$I_b'(x', y') = I_b(x', y') \otimes |h(x', y')|^2 \tag{1.3}$$

where $I_b(x', y')$ is the geometric profile of scene $I_b(x_0, y0)$. The measured intensity may be expressed as the sum of the coherent and incoherent components as

$$I_{meas}(x', y') = |U_l'(x', y')|^2 + I_b'(x', y'). \tag{1.4}$$

Let us assume the distance between the laser source and the imaging system is much

greater than the Rayleigh range, $z_R = \pi w_0^2/\lambda$, where $w_0$ is the waist of the laser. The laser field at the pupil of the system may then be represented as a tilted plane wave with uniform illumination over the aperture which may be represented by $U_0 exp[ik(\alpha x + \beta y)]$ where $U_0$ is a scalar amplitude, and $\alpha$ and $\beta$ are tip and tilt angles. This results in a geometric image of a shifted point represented by a dirac delta, $U_l(x', y') = \delta(x' - \alpha f, y' - \beta f)$. The Fourier transform of Eq. 1.4 represents the power spectrum, $S_{meas}(\xi_x, \xi_y)$, of the detected image:

$$S_{meas}(\xi_x, \xi_y) = FT[I_{meas}(x', y')] = \{FT[\delta(x' - \alpha f, y' - \beta f)] + S_b(\xi_x, \xi_y)\} \times H(\xi_x, \xi_y) \quad (1.5)$$

where $\xi_x = x/\lambda f$ and $\xi_y = y/\lambda f$ are spatial frequency coordinates and $S_b(\xi_x, \xi_y)$ is the power spectrum of the geometric background image, and $H(\xi_x, \xi_y)$ is the optical transfer function (OTF) defined as

$$H(\xi_x, \xi_y) = FT[|h(x', y')|^2] = \int_{-\infty}^{\infty} \int_{-\infty}^{\infty} |h(x', y')|^2 exp[-i2\pi(x'\xi_x + y'\xi_y)] dx' dy'. \quad (1.6)$$

The magnitude $|H(\xi_x, \xi_y)|$ is the modulation transfer function (MTF) which provides a measure of how the spatial frequencies of the geometric image are reduced in the final detected image.

The relationship between the pupil function, PSF, and OTF is nonlinear and complex resulting in the difficult problem of optimizing each function to provide the ideal system [58]. Two functions may provide the same laser suppression, but result in different image qualities. The integration of two MTF's may be the same, but their different distributions may result in different noise gains.

## 1.3 Deconvolution

In processing the image, the goal is to restore $I_b(x', y')$ through deconvolution. Using Eq. 1.5, this process can be done by dividing the spectrum of the final recorded image, $S_{meas}(\xi_x, \xi_y)$, by the OTF of the system, $H(\xi_x, \xi_y)$. Subtracting the laser contribution from the result will leave only the the incoherent scene. This process is known as inverse filtering.

In reality, the true recorded spectrum will contain some amount of noise from various sources such as Poisson noise, air turbulence, and detector noise. Adding the noise contribution, the resulting spectrum may be represented as

$$\begin{aligned} S_{meas}(\xi_x, \xi_y) &= [S_l(\xi_x, \xi_y) + S_b(\xi_x, \xi_y)] \times H(\xi_x, \xi_y) + N(\xi_x, \xi_y) \\ &= S_{tot}(\xi_x, \xi_y) \times H(\xi_x, \xi_y) + N(\xi_x, \xi_y) \end{aligned} \quad (1.7)$$

where $N(\xi_x, \xi_y)$ represents the total noise in the image and $S_{tot}(\xi_x, \xi_y)$ is the sum of the laser and scene spectra. Inverse filtering, dividing Eq. 1.7 by the OTF, results in:

$$\frac{S_{meas}(\xi_x, \xi_y)}{H(\xi_x, \xi_y)} = S_{tot}(\xi_x, \xi_y) + \frac{N(\xi_x, \xi_y)}{H(\xi_x, \xi_y)}. \quad (1.8)$$

The contribution $N(\xi_x, \xi_y)/H(\xi_x, \xi_y)$ leaves a high amount of noise gain when $|H(\xi_x, \xi_y)| << 1$ which would greatly degrade the restored image.

A method for restoring the image while considering the added noise must be used. Let $S_e(\xi_x, \xi_y)$ be the spectrum calculated from the experimentally recorded image. Consider the total error between $S_e(\xi_x, \xi_y)$ and Eq. 1.7.

$$E = \int\int |S_e(\xi_x, \xi_y) - [S_{tot}(\xi_x, \xi_y)H(\xi_x, \xi_y) + N(\xi_x, \xi_y)]|^2 d\xi_x d\xi_y \quad (1.9)$$

Minimizing the error and solving for $S_{tot}(\xi_x, \xi_y)$ results in

$$S_b(\xi_x, \xi_y) = S_e(\xi_x, \xi_y)\frac{H^*(\xi_x, \xi_y)}{|H(\xi_x, \xi_y)|^2 + 1/SNR(\xi_x, \xi_y)} = S_e(\xi_x, \xi_y)W(\xi_x, \xi_y) \tag{1.10}$$

where $W(\xi_x, \xi_y)$ is the Wiener filter and $SNR(\xi_x, \xi_y)$ is the signal to noise ratio as a function of spatial frequency. This process, called Wiener deconvolution, seeks to dampen the effect of noise on the final restored image [59]. Note that when the noise is zero, the Wiener filter becomes the inverse filter. In practice, the value of SNR may be an adjustable parameter rather than the experimentally determined function.

## 1.4 Image Quality Metrics

The system performance is categorized by 1) how much the intensity on the sensor is reduced and 2) the quality of the final image. We define a new quantitative metric, the light suppression ratio (LSR), which quantifies how much the sensor is protected. It is defined as the normalized peak value of the incoherent PSF or

$$LSR = \frac{max[|h(x', y')|^2]}{max[|h_0(x', y')|^2]} \tag{1.11}$$

where $|h_0(x', y')|^2$ is the diffraction-limited PSF. Through this work, an LSR is sought which protects a sensor for several orders of magnitude.

To quantify image quality, several metrics were considered. The National Imagery Interpretability Rating Scale (NIIRS) is the method the remote sensing and intelligence community uses for ranking satellite imagery [60]. Traditionally, a value from 0 to 9 is awarded to an image by an analyst based on the identifiable features in the image. To perform regular, consistent tests on simulated imaging systems, the general image quality

equation (GIQE) was created to estimate the NIIRS value by combining several quanitifiable metrics of an imaging system and is defined as

$$NIIRS = c_0 + c_1 log_{10}(GSD) + c_2 log_{10}(RER) - c_3 G/SNR + c_4 H \tag{1.12}$$

where $RER$ is the relative edge response, $GSD$ is the ground sample distance, $H$ is the edge overshoot, and $G$ is the noise gain [61]. The values of $c$ were found by fitting Eq. 1.12 to set of images in which NIIRS values had previously been assigned.

In the case of the PSF engineered system described in this work, the GIQE would be an extreme extrapolation of this fit as none of the images in the data set utilize PSF engineered reconstructions. In fact, the GIQE has been found inaccurate for highly aberrated images and those restored through deconvolution [62]. In addition, the metrics used as input values are empirical and require prior knowledge of the system including $GSD$ and $SNR$. Direct measurements are also required for $RER$ and $H$ for specific edges while the engineered PSF may have a different performance on each edge. In Ref. [62], the $RER$ and $G$ terms are identified as the important parameters of the GIQE for restored imagery. For experimental images, these terms will be used to quantify the image quality. For predicting the fidelity of restored images in simulation, a different, more fundamental image quality metric is sought.

The Strehl ratio is a commonly used method for quantifying image quality. Generally, this value is calculated as the on axis peak intensity of the PSF normalized by the PSF [63]. In this work, an alternate definition of the Strehl ratio is used which is calculated from the MTF [64]

$$Strehl = \frac{\int\int |H(\xi_x, \xi_y)| d\xi_x d\xi_y}{\int\int |H_0(\xi_x, \xi_y)| d\xi_x d\xi_y} \tag{1.13}$$

where $H_0(\xi_x, \xi_y)$ is the diffraction limited OTF. It was found that different phase masks with the same LSR may provide varying values for the integrated Strehl ratio. In addition, no empirical information of the imaging system is required.

A phase function is sought which maximizes the ratio $Strehl/LSR$. This problem containing three functions which are related nonlinearly: the pupil function, OTF, and PSF. As there is no known analytic solution, various numeric and analytic techniques are implemented to optimize the ratio.

## 1.5 Basic Phase Functions

To begin studying PSF engineered imaging systems, phase-only elements with long standing applications are observed. These elements include: axicons used for creating "diffraction free" bessel beams [57, 65], cubics used to enhance the depth of focus for wavefront coded systems [32, 34, 35], and vorticies which contain angular momentum and are used in optical trapping, coronagraphs, and communication [6, 66–68]. The phase functions for these elements are defined as

$$\Phi_{axicon}(x, y) = ar/R \tag{1.14a}$$

$$\Phi_{cubic}(x, y) = 2\pi b(x^3 + y^3)/R^3 \tag{1.14b}$$

$$\Phi_{vortex}(x, y) = m\theta \tag{1.14c}$$

where $a$, $b$, and $m$ are scaling parameters which alter the phase gradient and $R$ is the aperture radius. By increasing the phase gradient, the light is diffracted over a larger area on the focal plane which reduces the peak intensity. To do so comes at a potential cost to the fidelity of a restored image.

Each of these phase functions can be simulated numerically with their PSFs and OTFs

calculated via a Fast Fourier Transform (FFT) [69]. An NxN pixel computational grid is created with N = 4096. The pupil is defined by a circular aperture with radius $a_r = 512$ pixels and is multiplied by the phase function $exp[i\Phi(x, y)]$. The phase functions in Eq. 1.14 are each easily normalized relative to the radius of the aperture $(r/R)$. The FFT of the pupil is taken and the magnitude squared is taken to find the incoherent PSF. The inverse FFT is taken of incoherent PSF to calculate the OTF.

This process was implemented to calculate the PSF and OTF for several phase masks in the pupil: no phase, an axicon with $a = 40$, a cubic with value $b = 15$, and a vortex with value $m = 20$. The results are shown in Fig. 1.2. Each of the images are shown in a normalized coordinate space where the edge of the pupil (first row) is the coherent cutoff frequency, $\xi_0 = 1/2\lambda f\#$ where $\lambda$ is the wavelength of light, $f\# = f/2R$, and $f$ is the focal length. The edge of the MTF (third row) is the incoherent cutoff frequency. The second row shows the PSF and the fourth row the phase transfer function.

The axicon and vortex phase functions produce ring-like PSFs, with the axicon having a narrower annulus. The cubic produces a fan-like structure with an intense peak at the vertex. Both the vortex and axicon MTF's contain zeros as concentric rings. These zeros represent a total loss of information from the scene to the image. The cubic has most of the MTF concentrated on two perpendicular axes which may be good for imaging scenes which have a lot of perpendicular edges, but the PSF has a much greater extent which may limit the field of view, as the PSF may extend beyond the edge of the sensor.

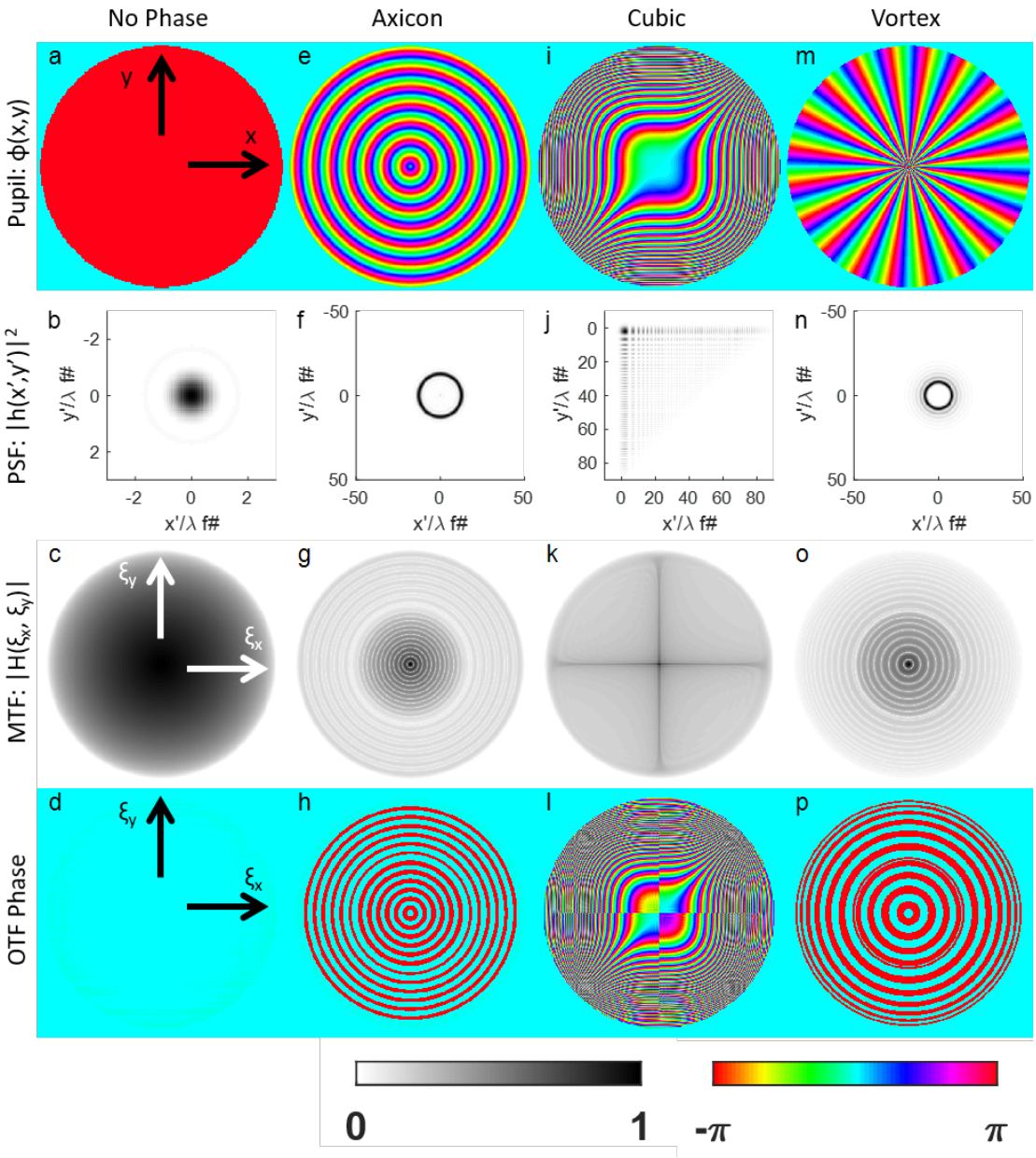


Figure 1.2: Phase Masks, PSF's, MTF's, and OTF phase for the diffraction-limited, axicon, cubic, and vortex cases with $a = 40$, $b = 15$, and $m = 20$. The MTF's are raised to a power of 0.3 (gamma corrected) in order to show hard-to-see details. Each phase mask results in a value of LSR of 0.02.

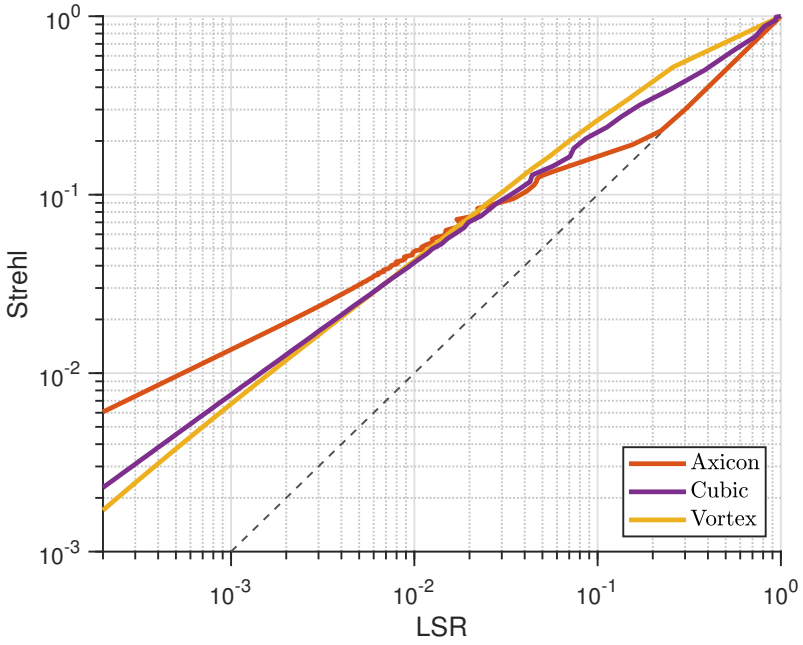


Figure 1.3: A plot of Strehl vs LSR for the axicon, cubic, and vortex phase functions.

The integrated Strehl ratio is calculated from the numeric MTFs by summing the pixel values and normalizing by the sum of the no phase MTF pixels. The LSR is calculated from the peak intensity of the PSF normalized by the no phase case. By altering the phase gradients ($a$, $b$, and $m$), continuous curves are generated for each phase function. The results are shown in Fig. 1.3. At any given value of LSR, Fig. 1.3 shows different phase functions can have vastly different integrated Strehl ratios. For values of LSR greater than 0.02, the vortex phase mask has the highest value of Strehl. For values of LSR less than 0.02, the axicon has the highest value of Strehl. Despite this, the nulls in the MTFs for the vortex and axicon phase functions will result in reconstructed images with a high noise gain.

At the value $LSR = 0.02$, each phase function produces a similar valued Strehl. These

points for the axicon, cubic, and vortex, phase functions were chosen for examples shown in Fig. 1.2. Studying these three masks will provide insight beyond the value for Strehl. The phase functions at a value for LSR of 0.02 are to be compared experimentally to observe their respective performance both qualitatively and quantitatively to better understand the system.

## 1.6 Outline of Thesis

In this thesis, a PSF engineering system is optimized to maintain imaging fidelity while simultaneously suppressing laser intensity by several orders of magnitude. Analytic and numeric methods are employed to improve the performance of the imaging system. Chapter 2 describes theoretical performance limitations of PSF engineered systems. Design of the phase function based on its even and odd symmetry are considered with an advantage to odd symmetries found. Chapter 3 presents the experimental setup designed to validate the imaging performance of the phase functions. A phase-only spatial light modulator is utilized as a digitally controllable phase mask. Challenges associated with the spatial light modulator are discussed and methods to ameliorate these issues are presented. The setup is utilized to image a target with already known phase functions. In chapter 4, numeric and analytic techniques for optimizing the phase masks are presented. These optimized masks are tested using the experimental setup. Chapter 5 considers effects and challenges of imaging a broadband scene. Chapter 6 provides conclusions and future directions.

# Chapter 2

# Point Spread Function Engineering Theory

PSF Engineering seeks to add additional functionality by altering the PSF of the imaging system. Doing so broadens the PSF, which reduces the SNR of the imaging system. As the PSFs studied in this thesis seek to reduce the peak intensity of the PSF by several orders of magnitude, the degradation of the image is expected to be much greater than for other PSF engineered systems. What is more, the introduction of nulls in the optical transfer function will lead to spatial frequencies of the scene that will not be transferred to the image - a complete loss of information at that spatial frequency. By creating a well designed PSF, the degradation may be avoided. In this chapter, PSFs are studied analytically in terms of the integrated Strehl ratio and the newly defined light suppression ratio ($LSR$). Limits of the Strehl ratio are derived relative to the newly defined light suppression ratio. In addition, the odd and even symmetry of PSFs and pupil functions are studied. Pupil functions with odd symmetry are shown to have improved Strehl ratios

and limited MTF nulls making them advantageous. Finally, when imaging with multiple PSFs with a poor performing OTFs, a method of combining the exposures into a single image through a joint deconvolution method is shown with potential to prevent unwanted noise gain.

## 2.1 Strehl Ratio Limits

We seek to maximize the image quality relative to the peak intensity of the PSF or the ratio $Strehl/LSR$. By deriving the fundamental limits in the value of Strehl relative to a given value of LSR, we hope to better understand how to design an ideal phase mask.

First, the minimum value for Strehl/LSR, the worst imaging solution, may be found. Considering the location of the peak intensity of the PSF at the point $(x_p, y_p)$, the following inequality may be made

$$g(x_p, y_p) = \int\int H(\xi_x, \xi_y) exp[2\pi i(x_p\xi_x + y_p\xi_y)] d\xi_x d\xi_y \leq \int\int |H(\xi_x, \xi_y)| d\xi_x d\xi_y. \quad (2.1)$$

Rearranging Eq. 2.1 results in

$$\frac{\int\int |H(\xi_x, \xi_y)| d\xi_x d\xi_y}{g(x_p, y_p)} \geq 1 \quad (2.2)$$

For the no phase case, $\int\int |H_0(\xi_x, \xi_y)| d\xi_x d\xi_y / g(0,0) = 1$, which allows for Eq. 2.2 to be normalized as

$$\frac{\int\int |H(\xi_x, \xi_y)| d\xi_x d\xi_y / \int\int |H_0(\xi_x, \xi_y)| d\xi_x d\xi_y}{g(x_p, y_p)/g(0,0)} = \frac{Strehl}{LSR} \geq 1 \quad (2.3)$$

which defines the lowest attainable value for Strehl/LSR as 1.

The minimum occurs when $|H(\xi_x, \xi_y)| = H(\xi_x, \xi_y)$ or when the OTF is real and positive at all points. A large imaginary portion of the OTF would increase the $Strehl/LSR$. The imaginary portion of the OTF is equal to the Fourier transform of the odd portion of the PSF where the odd portion is equal to

$$g_{odd}(x', y') = 1/2[g(x', y') - g(-x', -y')]. \tag{2.4}$$

Maximizing $\int |g_{odd}(x', y')| dx'dy'$ in turn maximizes the imaginary portion of the OTF. As the PSF is real and positive, the maximum value for the integrated odd PSF is when it is equal to the integrated even PSF where the even portion of the PSF is

$$g_{even}(x', y') = 1/2[g(x', y') - g(-x', -y')]. \tag{2.5}$$

From Eq. 2.4, the maximum integrated odd PSF occurs when, for each nonzero value of the PSF ($\hat{x}$, $\hat{y}$), $g(-\hat{x}, -\hat{y}) = 0$.

While an analytic maximum value for Strehl/LSR is unknown, a maximum for the value of $\int\int |H(\xi_x, \xi_y)|^2 d\xi_x d\xi_y$ may be found. Following Parseval's theorem, the integrated square magnitudes of the OTF and PSF are equivalent

$$\int\int |H(\xi_x, \xi_y)|^2 d\xi_x d\xi_y = \int\int |g(x', y')|^2 dx'dy'. \tag{2.6}$$

For a given value of peak amplitude of the PSF, $g(x_p, y_p) = g_{max}$, the maximum value of $\int\int |g(x', y')|^2 dx'dy'$ occurs when the PSF is uniform over its spatial extent. Solving $\int\int g(x', y') dx'dy' = \int_L g_{max} dA = H(0, 0) = 1$ results in $L = 1/g_{max}$, where $L$ is the spatial extent of the PSF and $dA$ is the integration over an area. Combining this result

with Eq. 2.6 gives

$$\int\int |H(\xi_x,\xi_y)|^2 d\xi_x d\xi_y = \int\int |g(x',y')|^2 dx'dy' \leq \int_L g_{max}^2 dA = g_{max}. \tag{2.7}$$

$$\frac{\int\int |H(\xi_x,\xi_y)|^2 d\xi_x d\xi_y}{g_{max}} \leq 1. \tag{2.8}$$

As previously stated, this maximum occurs for a PSF which is uniform over a finite spatial extent. This theoretical PSF is not possible, but provides a mathematical limit.

The limits described assist in designing an ideal PSF for a given LSR. In addition, to create a broad MTF, the PSF must contain narrow features. The desired attributes of the PSF are:

1. Has a large integrated odd portion
2. Has values close to to its peak intensity and zero otherwise
3. Contains narrow features

Following these points will lead to high performing PSF engineered imaging systems.

## 2.2 Odd and Even Pupil function Taxonomy

As there is no ideal analytic solution to a PSF engineered system, a framework for designing phase masks with high imaging performance relative to LSR is sought. From Sec. 2.1, it was found that a high performing system will have a large imaginary portion of the OTF. This imaginary portion is directly related to the even and odd symmetry of the PSF. Understanding how this symmetry propagates from the pupil all to the OTF will allow for building an understanding of higher performing phase masks and will allow for limiting the search space for a desired phase function.

### 2.2.1 Even and Odd Functions and their Fourier transforms

For a real 2-dimensional function, the function is considered even if

$$f(x,y) = f(-x,-y) \tag{2.9}$$

$$f(r,\theta) = f(r,\theta+\pi) \tag{2.10}$$

and odd if

$$f(x,y) = -f(-x,-y) \tag{2.11}$$

$$f(r,\theta) = -f(r,\theta+\pi). \tag{2.12}$$

The Fourier transform of an even function may be simplified as a cosine transform as follows

$$\begin{aligned} F_E[\xi_x,\xi_y] &= \int f_E(x,y)exp[-2\pi i(x\xi_x+y\xi_y)]dxdy \\ &= \int f_E(x,y)cos[-2\pi(x\xi_x+y\xi_y)]dxdy - i\int f_E(x,y)sin[2\pi(x\xi_x+y\xi_y)]dxdy \\ &= \int f_E(x,y)cos[2\pi(x\xi_x+y\xi_y)]dxdy. \end{aligned} \tag{2.13}$$

where the subscript E represent the even portion of the function. Considering $F_E[-\xi_x,-\xi_y]$, the Fourier transform of an even function may shown to be even.

$$\begin{aligned} F_E[-\xi_x,-\xi_y] &= \int f_E(x,y)cos[-2\pi i(x(-\xi_x)+y(-\xi_y))]dxdy \\ &= \int f_E(x,y)cos[-2\pi i(x\xi_x+y\xi_y)]dxdy \\ &= F_E[\xi_x,\xi_y] \end{aligned} \tag{2.14}$$

The odd function Fourier transforms may similarly be calculated as sine transforms

$$F_O[\xi_x, \xi_y] = -i \int f_O(x,y) sin[2\pi(x\xi_x + y\xi_y)]dxdy \tag{2.15}$$

where the subscript O denotes the odd portion of the function.

$$\begin{aligned} F_O[-\xi_x, -\xi_y] &= \int f_O(x,y) sin[-2\pi i(x(-\xi_x) + y(-\xi_y))]dxdy \\ &= -\int f_O(x,y) sin[-2\pi i(x\xi_x + y\xi_y)]dxdy \\ &= -F_O[\xi_x, \xi_y]. \end{aligned} \tag{2.16}$$

For any function $f(x,y)$, the even and odd portions may be calculated as

$$f_E(x,y) = 1/2[f(x,y) + f(-x,-y)] \tag{2.17a}$$

$$f_O(x,y) = 1/2[f(x,y) - f(-x,-y)]. \tag{2.17b}$$

### 2.2.2 Odd/Even Pupil Functions

As the OTF is the Fourier transform of a real and positive function, it has unique properties limiting its structure. First, the OTF has a real portion that must be even and an imaginary portion that is odd. This may be expressed as

$$H(\xi_x, \xi_y) = H_E(\xi_x, \xi_y) + iH_O(\xi_x, \xi_y). \tag{2.18}$$

The even and odd portions of the incoherent PSF may be calculated as the Fourier transform of the OTF as

$$|h(x', y')|_E^2 = FT[H_E(\xi_x, \xi_y)] \tag{2.19}$$

and

$$|h(x',y')|_O^2 = iFT[H_O(\xi_x,\xi_y)]. \tag{2.20}$$

Now consider breaking the coherent PSF into it's even, odd, real, and imaginary components as

$$h(x',y') = [h_{RE}(x',y') + h_{RO}(x',y')] + i[h_{IE}(x',y') + h_{IO}(x',y')] \tag{2.21}$$

where $R$ and $I$ denote the real and imaginary portions.

From Eq. 2.20, if the incoherent PSF is even, then the OTF is real and even. Geometrically, this occurs when the incoherent PSF is equal to a $180^o$ rotation of itself – giving a qualitative indicator of when this may occur. Combining Eq. 2.17b and 2.21, the odd portion of the incoherent PSF may be calculated in terms of the components of the coherent PSF as

$$\begin{aligned} |h(x',y')|_O^2 &= \frac{1}{2}[|h(x',y')|^2 - |h(-x',-y')|^2] = 0 \\ h_{RE}(x',y')h_{RO}(x',y') &+ h_{IE}(x',y')h_{IO}(x',y') = 0. \end{aligned} \tag{2.22}$$

This provides the framework for creating imaging systems with a real-only OTF. This occurs only for the trivial solutions where both $h_{RE}(x',y')h_{RO}(x',y')$ and $h_{IE}(x',y')h_{IO}(x',y')$ are equal to zero. Relating this property to the pupil function results in

$$FT[P_{RE}(x,y)]FT[P_{IO}(x,y)] + FT[P_{IE}(x,y)]FT[P_{RO}(x,y)] = 0. \tag{2.23}$$

When Eq. 2.23 is true, then the OTF is both even and entirely real. No nontrivial solution exists to this where each of the terms are nonzero. Instead, the pupil by may be categorized depending on which of its even, odd, real, and imaginary components are

zero. An overview of these are shown in Tab. 2.1. The table suggests the use of odd phase functions will guarantee a complex OTF.

| | 1 | 2 | 3 | 4 |
|---|---|---|---|---|
| $\phi_E(x,y)$ | $\neq 0$ | $\neq 0$ | 0 | $\neq 0$ |
| $\phi_O(x,y)$ | $0, \pm\pi$ | $\pm\pi$ | $\neq 0$ | $\neq 0$ |
| $t_{RE}(x,y)$ | $\neq 0$ | 0 | $\neq 0$ | $\neq 0$ |
| $t_{RO}(x,y)$ | 0 | $\neq 0$ | 0 | $\neq 0$ |
| $t_{IE}(x,y)$ | $\neq 0$ | 0 | 0 | $\neq 0$ |
| $t_{IO}(x,y)$ | 0 | $\neq 0$ | $\neq 0$ | $\neq 0$ |
| $h_{RE}(x',y')$ | $\neq 0$ | 0 | $\neq 0$ | $\neq 0$ |
| $h_{RO}(x',y')$ | 0 | $\neq 0$ | $\neq 0$ | $\neq 0$ |
| $h_{IE}(x',y')$ | $\neq 0$ | 0 | 0 | $\neq 0$ |
| $h_{IO}(x',y')$ | 0 | $\neq 0$ | 0 | $\neq 0$ |
| $\lvert h(x',y')\rvert^2_E$ | $\neq 0$ | $\neq 0$ | $\neq 0$ | $\neq 0$ |
| $\lvert h(x',y')\rvert^2_O$ | 0 | 0 | $\neq 0$ | $\neq 0$ |
| $H_I(\xi_x,\xi_y)$ | 0 | 0 | $\neq 0$ | $\neq 0$ |

Table 2.1: Table categorizing the different phase masks in terms of odd, even, real and complex functions where $\phi(x,y)$ is the phase function, $t(x,y)$ is the pupil function, $h(x',y')$ is the coherent PSF, $|h(x',y')|^2$ is the incoherent PSF, and $H(\xi_x,\xi_y)$ is the OTF. The subscripts $E$, $O$, $R$, and $I$ . The end result is whether The OTF of such an imaging system is real or complex.

## 2.3 Joint Deconvolution

A method for combining multiple images of the same scene with different point spread functions was developed for improving fidelity of restored images. By reducing the peak intensity of the PSF, regions of the MTF will often have low magnitude or contain zeros or nulls. A potential correction for these nulls is a joint deconvolution method. Multiple images of the same scene using different phase elements may be combined to remove zeros. This may be implemented by exposing multiple sensors to the same scene using a

beamsplitter or by alternating elements of each frame through a filter wheel. The proposed method may use any number of elements to create an estimate of the scene.

Restoring the scene using the joint method requires a generalized version of the Wiener filter. The process has previously been used for wavefront sensing using phase diversity and for recovering depth information [70, 71]. Consider the mean square error, $E$, between the power spectrum of the detected image and the expected image. For two images of the scene resulting in

$$E = \int\int |S_1(\xi_x, \xi_y) - S_b(\xi_x, \xi_y)H_1(\xi_x, \xi_y)|^2 d\xi_x d\xi_y + \int\int |S_2(\xi_x, \xi_y) - S_b(\xi_x, \xi_y)H_2(\xi_x, \xi_y)|^2 d\xi_x d\xi_y \quad (2.24)$$

This error is minimized and results in an estimate for the power spectrum of the scene

$$S_b(\xi_x, \xi_y) = \frac{S_1(\xi_x, \xi_y)H_1^*(\xi_x, \xi_y) + S_2(\xi_x, \xi_y)H_2^*(\xi_x, \xi_y)}{|H_1(\xi_x, \xi_y)|^2 + |H_2(\xi_x, \xi_y)|^2 + \gamma(\xi_x, \xi_y)} \quad (2.25)$$

where $\gamma(\xi_x, \xi_y)$ is the average of the expected SNR of the two images. This estimate may be extended for any number of images

$$S_b(\xi_x, \xi_y) = \frac{\sum_{n=1}^{N} S_n(\xi_x, \xi_y)H_n^*(\xi_x, \xi_y)}{\gamma(\xi_x, \xi_y) + \sum_{n=1}^{N} |H_n(\xi_x, \xi_y)|^2} \quad (2.26)$$

The final image may be restored through an inverse Fourier transform. The MTF of this system may be estimated as the average of the component MTF's. Ideally, MTF's of the combined cases would result in an MTF with near diffraction-limited performance. In this case, the vortex and axicon cases are combined with the goal of removing their nulls. The resulting theoretical and experimental MTF's are shown in Fig. 2.1. Also shown is

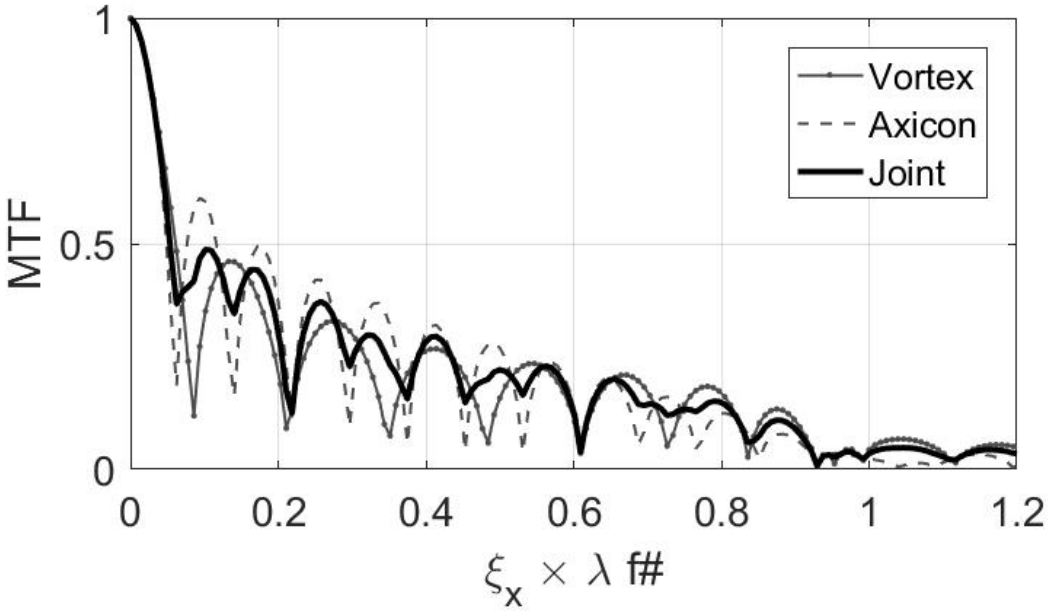


Figure 2.1: Line profiles of the MTFS for the vortex with $m = 20$ and axicon with $a = 40$ and an estimate of the their joint MTF. The cutoff frequency $2\xi_x \times \lambda f/2R$ is not shown. The minima for the vortex case is compensated by the axicon to remove minimums in the joint case, thereby removing information loss at nulls.

a cross-section of the experimental vortex, axicon and joint result along the $\xi_x$ axis. The figure shows many of the nulls from the axicon fall along the peaks of the vortex and vice versa.

## 2.4 Summary

In this chapter, PSF engineered systems were studied in order to identify desirable features for the pupil phase. Limits of PSFs, independent of the use of phase-only masks, were found relative to the integrated Strehl ratio. OTFs with only real and positive values were identified as the lowest performing. In contrast, OTFs should have phase which may

be accomplished with a PSF with a high odd portion. The information, the integrated MTF squared, was found to be maximized by a PSF which is uniformly illuminated over its spatial extent. Also, PSFs with narrow features result in MTFs with greater high frequency content.

Noting that OTFs with greater odd components result in high performing Strehl ratios, optical functions were studied relative to their odd and even symmetry. Pupils with odd phase functions were identified as giving this result.

Finally a joint deconvolution method was described which allows for multiple low performing PSFs to overcome their low performance by combining multiple exposures into a single reconstruction. An example was shown using the axicon and vortex phase function which results in nulls that do not coincide with one another.

# Chapter 3

# Experimental System and Implementation

In this thesis, both previously studied phase masks and newly optimized ones are to be tested and validated experimentally. As it is not feasible to manufacture thin transparent masks for each phase function studied, a liquid crystal on silicon (LCOS) spatial light modulator (SLM) is used as the pupil-phase mask in experiment. These advanced electro-optic devices can produce arbitrary phase functions on its reflective surface by leveraging the birefringent properties of liquid crystals. While the SLM allows for these experiments to be possible, they also introduce challenges which would not be present in a static, transparent phase mask. In this chapter, the experimental setup is discussed which seeks emulate a PSF engineered imaging system imaging a distant scene with a laser present. Challenges of using the SLM are discussed as well as methods from overcoming them. Lastly, the setup will be implemented to test the previously mentioned axicon, cubic and vortex phase functions.

## 3.1 Experimental Setup

An experimental setup is designed to validate the performance of the studied phase functions. The setup seeks to emulate each component of the theoretic schematic in Fig. 1.1 consisting of a distant scene consisting of an intense laser source and an incoherent background scene, a pupil containing a phase-only mask, and the detector. The setup is shown in Fig. 3.1.

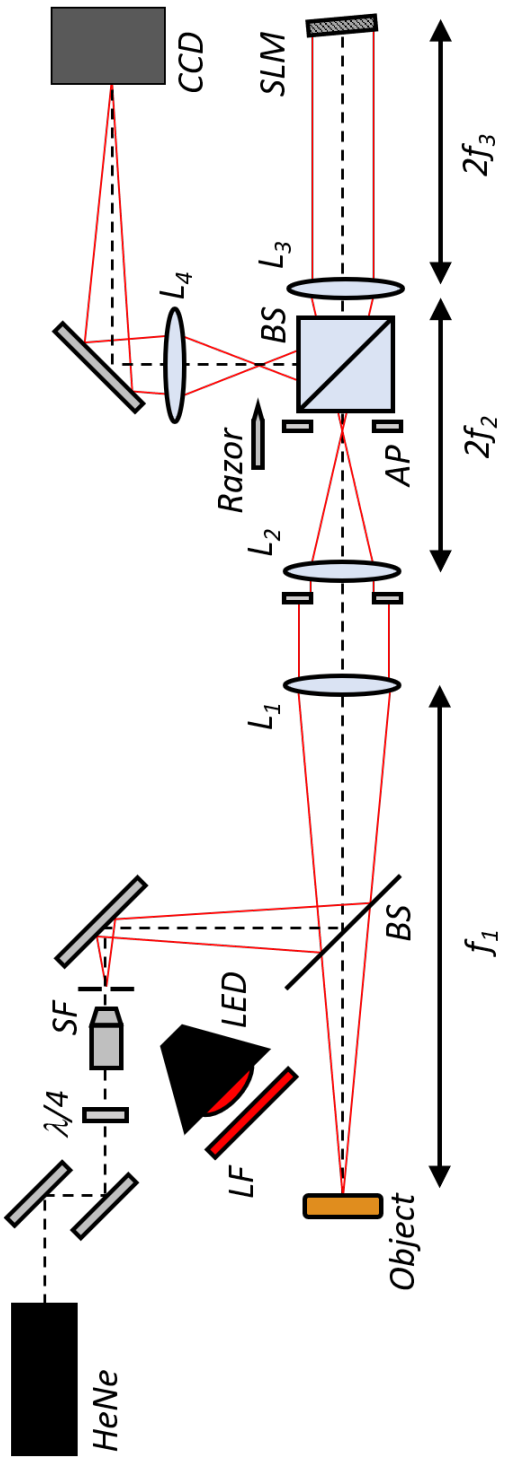


Figure 3.1: Experimental optical setup of the experiment. A coherent HeNe laser source and incoherently illuminated object (T) are simultaneously imaged onto a CCD camera and modulated by a spatial light modulator (SLM). A laserline filter (LF) is attached to the CCD camera to record quasi-monochromatic light. Quarter wave plate ($\lambda/4$), Light emitting diode (LED), Diffuser (D), Spatial Filter (SF), Beamsplitter (BS), focal length of $n^{th}$ lens ($f_n$).

The setup may be considered in two parts: the scene consisting of the laser source and incoherent object, and the imaging system with the phase element in the pupil. For the scene, a HeNe laser is spatially filtered (SF) using a microscope objective and 10 $\mu$ m pinhole, expanded, and collimated by $L_1$ with a focal length of $f_1 = 40\ cm$. The long focal length ensures the beam is expanded enough that pupil may be considered evenly illuminated. Several objects and illumination sources are used through the work presented in this thesis including trasmissive resolution bar targets and small model figurines. In each case, the object is illuminated by incoherent light filtered by a laserline filter ($LF$) to ensure only quasi-monochromatic light centered at 633 nm is imaged. The filter has a full width at half max of 10 nm. A diffuser is place on the back side of the transmissive object when used to better emulate a distant object. A pellicle beamsplitter (BS) is used to combined the incoherent object and laser source.

The pupil of the imager is at $L_2$ with focal length $f_2 = 10\ cm$. The light from the object and the laser evenly illuminate a circular aperture placed in front of the lens. The pupil is imaged onto the SLM by $L_3$ with focal length $f_3 = 10\ cm$. The reflection off the SLM is altered by a predetermined phase function. The reflection passes through $L_3$ again, reflects off of a non-polarizing beam splitter (BS) where a blurred intermediate image is filtered by a razor blade. This blurred imaged is reimaged and magnified onto a CCD sensor by $L_4$ with focal length $f_4 = 30\ cm$. An aperture between $L_2$ and the beam splitter limits the field of view of the setup.

Two experimental setups were implemented during the course of this work. One at the Naval Research Laboratory (NRL) used to produce the results in Sec. 3.3 and 4.1.1. Another setup at the Rochester Institute of Technology was used to produce the results in Sec. 4.5. A photo of this second setup is shown in Fig. 3.2.

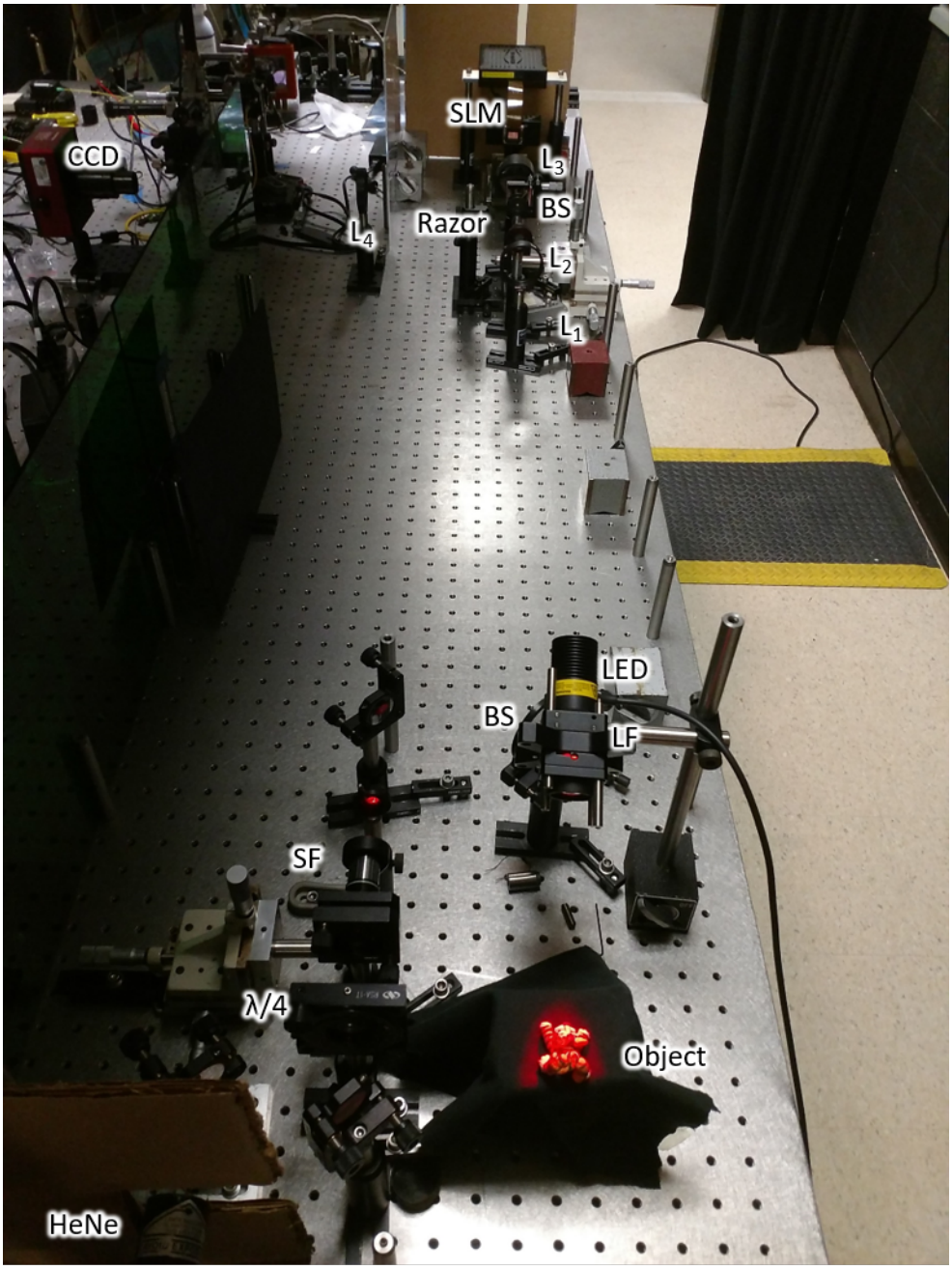


Figure 3.2: Photo of the experimental setup.

## 3.2 Spatial Light Modulator

The SLM acts as a digitally-controllable phase mask. The device allows for testing arbitrary phase functions, but leads to complications due to its diffractive, pixelated surface that must be resolved to successfully emulate the PSF engineered imaging system. SLM's are studied in order to determine how to properly implement them into the experimental setup.

### 3.2.1 SLM Background

The SLM leverages the electro-optic properties of liquid crystals (LC) to effectively produce a programmable phase mask. Depending on the orientation of a LC relative to incident light, the index of refraction is altered. The difference between the ordinary refractive index, $n_o$, and the extraordinary refractive index, $n_e$ is the birefringence and is the defining optical characteristic of the LC.

$$\Delta n = n_e - n_o \tag{3.1}$$

By altering the bend angle of the crystal, the refractive index may be altered between $n_o$ and $n_e$. A diagram of a liquid crystal is shown in Fig. 3.3. The thickness of a liquid crystal

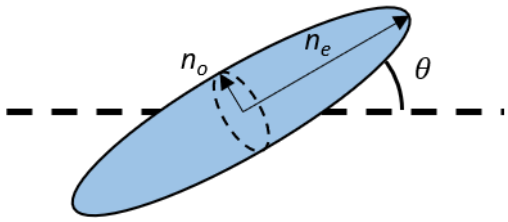


Figure 3.3: Diagram of liquid crystal showing the ordinary refractive index $n_o$, extraordinary refractive index $n_e$, and bend angle $\theta$.

material, $d$, may be increased to allow for a greater change to the wavefront with the total

phase change determined by

$$\delta = 2\pi\Delta nd/\lambda \tag{3.2}$$

where $\delta$ is the phase change in radians and $\lambda$ is the wavelength of light. On a diffractive surface, a phase change of only $2\pi$ is required. As typical birefringence ranges from 0.05 to 0.45 [72] and considering the desired $2\pi$ phase change, the liquid crystal layer would need minimum ranges in thickness from 1.4-13 $\mu m$ at a wavelength of 633 nm.

Liquid crystals align themselves with strong electric field, leading to their application in electro-optical systems. For spatial light modulators, the electric field within the liquid crystal is varied spatially to produce arbitrary phase patterns. A basic schematic for an SLM is shown in Fig. 3.4. A liquid crystal layer is sandwiched between two alignment layers which are mechanically rubbed along a specific direction. The LC's will self align along this direction and only modify the phase of light which matches this polarization. The front facing side has an anti-reflection coated transparent electrode which is connected to an electrical ground. The back layer has an aluminum pixel array whose voltage can be controlled individually by a CMOS chip. Increasing the voltage of a pixel increases the electric field running perpendicularly between the pixel and the transparent electrode. The greater the electric field, the greater the bend angle of the LCs. The aluminum pixel array also acts as a reflective surface for incident light. Light first pass through the transparent electrode, then the LC layer, and then reflects off the pixel array, ultimately passing through the LC layer twice [73].

The pixelated surface of the SLM leads to many challenges which must be overcome to properly emulate a PSF engineered system. Some SLMs (not used in this thesis) have an added dielectric reflective surface in front of the array which improves the diffractive efficiency and protects the back plane from high power lasers [74, 75], but even these still

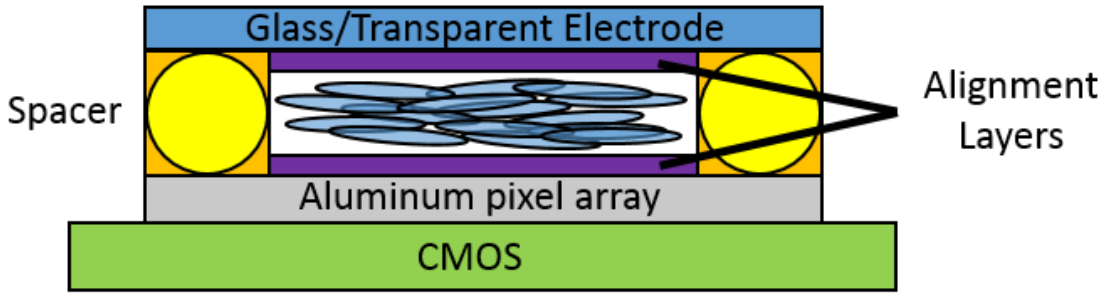


Figure 3.4: Cross section of the liquid crystal on silicon (LCOS) SLM.

| Manufacturer | Holoeye | |
|---|---|---|
| Model | Pluto | GAEA-2 |
| Pixel Pitch | 8 $\mu$m | 3.74 $\mu$m |
| Resolution | 1920x1080 | 4096x2160 |
| Frame Rate | 60 Hz | 60 Hz |
| Fill Factor | 93% | 90% |

Table 3.1: Specifications for spatial light modulators used in this work.

have effects from the pixelated surface.

In this work, two spatial light modulators were used from Holoeye Photonics [75]. The specifications of these are shown in Tab. 3.1

### 3.2.2 Limitations of the SLM

The SLM provides a programmable pupil mask which allows for testing arbitrary phase functions. Despite it's versatility, the SLM has drawbacks that would not be present in a static phase mask due to limited fill factor and diffraction efficiency. These drawbacks and their solutions are discussed in this section.

Due to the phase quantization, spatial quantization, and dead regions of the SLM between pixels, there is a zero order reflection from the SLM [76, 77]. In the case of beam shaping where the source is a collimated laser, the zero order results in a bright point on

the optical axis. In the case of PSF engineered imaging, a ghost image of the scene is present on top of the desired blurred image when the SLM is aligned with the optical axis. The effect is shown in Fig. 3.5. The image with a zero order artifact does not properly resemble the desired imaging system.

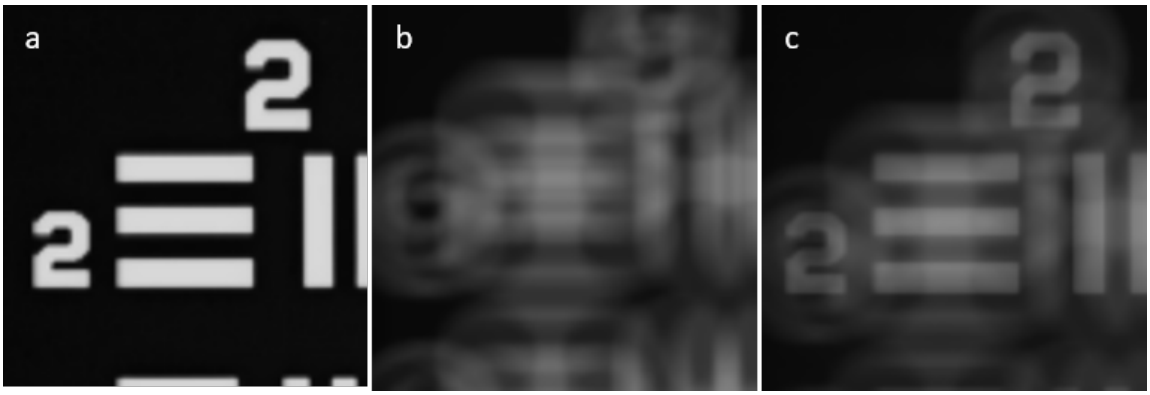


Figure 3.5: Simulation illustrating the issue from zero order reflection of the SLM. a) Scene to be imaged. b) Desired image using axicon phase mask. c) Image with zero order ghost image.

Several methods have been previously studied for suppressing the zero order which involve adding a corrective phase to the SLM. One method is adding a spherical wavefront to the existing phase to move the focal plane of the diffractive light along the optical axis [78]. This method greatly reduces the peak intensity of the zero order, but does not remove the unwanted light from the detector. As the image will also have a reduced intensity, this method would not be effective. Another method would add a phase function which produces a beam which destructively interferes with the zero order [79]. This method is not possible with the Holoeye SLM which has a high speed flicker which would inconsistently eliminate the zero order. The chosen method adds a tilt function to the SLM and rotates the angle of the SLM to retro reflect the diffracted light while deflecting the zero order away from the desired image [78, 80]. This method is shown in Fig. 3.6. For the experiments performed in

this work, a sawtooth function with period of 4 SLM pixels is used requiring a tilt angle of $\theta_t = 2.43^o$ tilt of the SLM to retro-reflect the desired light. The deflected zero-order image is blocked by the razor blade at an intermediate image as shown in Fig. 3.1.

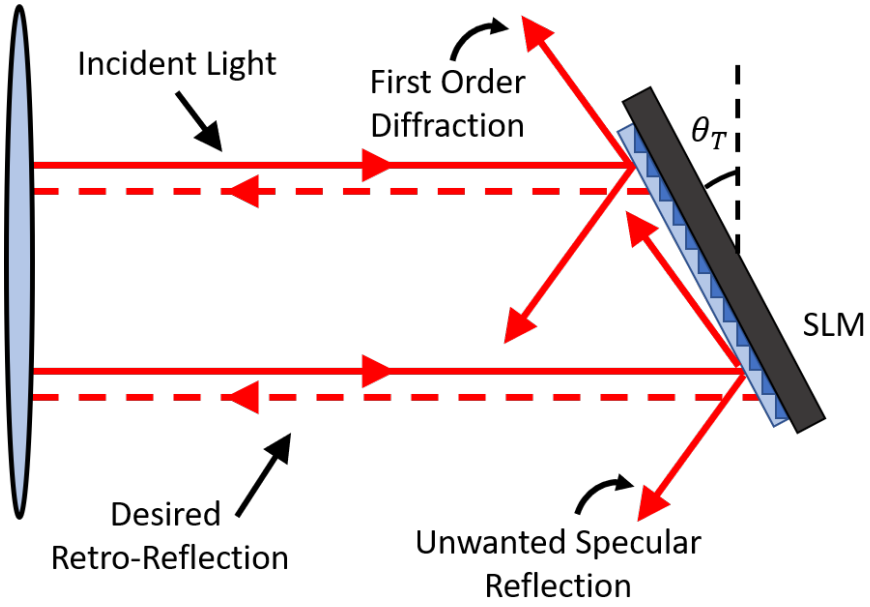


Figure 3.6: SLM configuration with sawtooth phase function addressed to SLM and the SLM tilted to retro-reflect desired diffraction pattern. The angle $\theta_t$ is exaggerated in the figure with a value of $2.6^o$ used in experiment.

SLM is limited in field of view due to the pixelation of the SLM as reflected light is diffracted into multiple orders. These multiple orders form multiple images of the scene as shown in the ray trace in Fig. 3.7. The object of length $d$ is brought to a distance by lens $L_3$ with focal length $f$. Light is reflected off the SLM and is diffracted into multiple diffractive orders separated by angle $\theta_D = \lambda/p$ where $p$ is the pixel pitch of the SLM. The light passes through $L_3$ again and forms an image of the object. Because of the diffractive orders, multiple images of the object will occur. If $f\lambda/p < d$ (Image 1), then these images

will overlap with one another. Because of this, the system must limit the field of view in order to achieve $f\lambda/p > d$. In addition, because of the zero order light, the desired image must fit between two diffractive orders with the desired image fitting in between. Thus, the intermediate object size a focal length in front of $L_3$ must fulfill $d < f\lambda/2p$. As the extended PSF will enlarge the image, the constraints are even tighter, but is dependent on the extent of the PSF. This limit may be enforced using an aperture at the intermediate image before $L_3$.

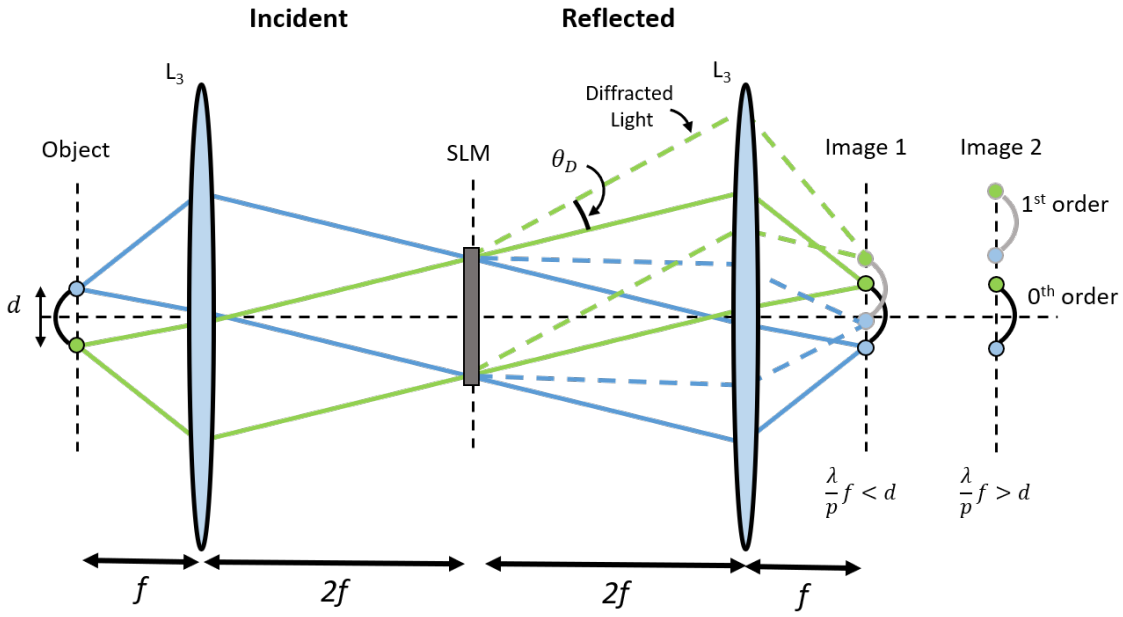


Figure 3.7: Ray trace from a selected region of the experimental setup. When $\lambda f/p < d$, there is overlap in the image plane between the subsequent diffractive orders.

Additional issues occur due to a duty cycle of the SLM. The SLM is advertised with a refresh rate of 60 Hz. To analyze any effects the refresh rate may have on testing a static phase function, a high speed Edgertronic SC1 record is used in lieu of the CCD in Fig. 3.1. The sensor records the focal spot of a laser at a rate of 1972.39 Hz. A tilt correction is

applied to the SLM to separate the zero order for the diffracted light. A duty cycle of 50% was found where the liquid crystals are in a relaxed state leaving only the zero order diffraction for 50% of the time. The on state, off state, and a line profile as a function of time are shown in Fig. 3.8. In the line profile, a flicker can be seen where the intensity of the desired light is oscillating. The oscillation appear consistent and does not affect imaging as long as an integer number of periods of the duty are recorded in a single exposure.

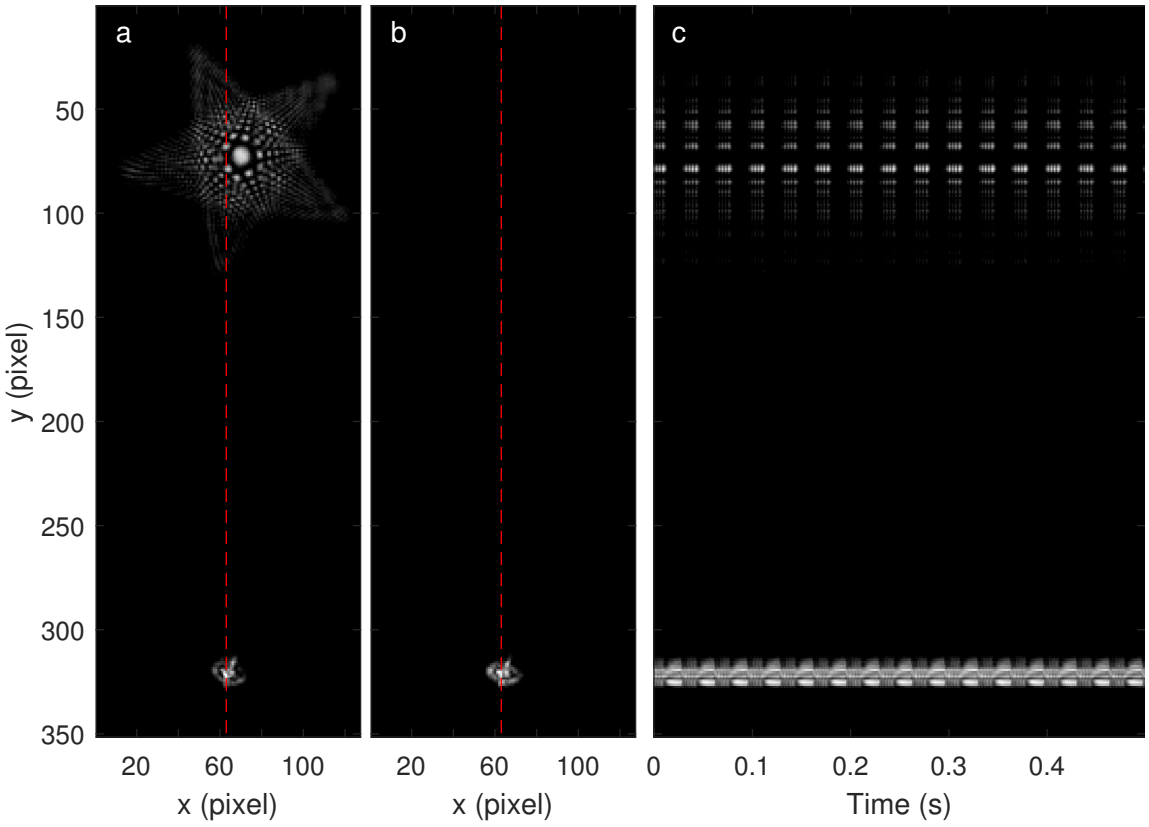


Figure 3.8: Images recorded with high speed camera to image effects of flicker and duty cycle on the SLM. The phase function $7.5 \times 2\pi r^2 cos[5\theta]$ is applied to the SLM and a sawtooth function is added as well to separate the diffracted light from the zero order. a) image of the laser with the duty cycle on, b) with the duty cycle off, and c) a line profile (red dashed line) as a function of time.

SLM's typically contain surface errors which leads to wavefront errors and aberrations in the imaging system [76, 77]. The PSF of the experimental system including the Holoeye GAEA SLM was recorded by imaging the laser spot in Fig. 3.1 alone with only the tilted phase function on the SLM. The resulting aberrated PSF is shown in Fig. 3.9a. The aberration was verified to be caused by the SLM by replacing the SLM with a flat mirror, resulting in a near diffraction limited PSF. The aberrations will affect the OTF of the system and lead to degradation in the reconstructions. Luckily, if the phase function is known, the wavefront may be corrected using the SLM itself. As an alternative to using a wavefront sensor, a stochastic parallel gradient descent (SPGD) algorithm is used to optimize the PSF and correct aberrations [81, 82]. A random phase perturbation with a maximum phase of about a quarter of a wave is added to the SLM to create a candidate phase correction using a basis of 14 Zernike polynomials (skipping piston). An image of the laser spot is recorded and the sharpness is calculated as

$$Sharpness = \sum [I(x,y)^2] / [\sum I(x,y)]^2 \tag{3.3}$$

where $I$ are the intensity values of the image in counts. If the sharpness of the PSF increases, then the candidate phase is retained and the same perturbation is added again. If the sharpness is reduced, a new random perturbation is added to the current phase of the SLM. The process is repeated until the PSF is satisfactory. The algorithm was tested using the Holoeye GAEA SLM for 2000 iterations. The resulting corrected PSF and wavefront correction is shown in Fig. 3.9b and 3.9c.

In experiment, the phase function of applied to the SLM ($\Phi_{SLM}[x,y]$) is the sum of the tilt function ($\Phi_{Tilt}[x,y]$), wavefront correction ($\Phi_{Corr}[x,y]$), and the desired phase function ($\Phi_{Des}[x,y]$). This sum is shown in Fig. 3.10 using $\Phi_{Des}[x,y] = 20\pi r$ as an example. In

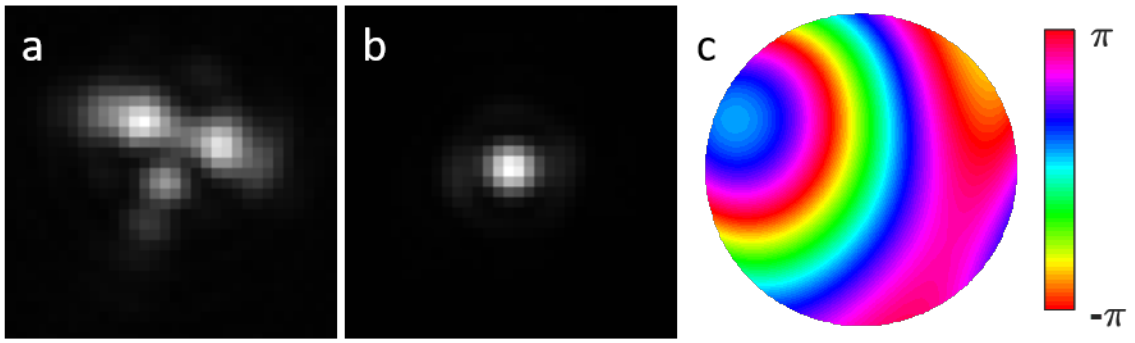


Figure 3.9: a) The experimentally recorded PSF aberrated by the surface errors of the SLM. b) The experimentally recorded PSF after the SPGD algorithm. c) The phase function for correcting the SLM wavefront error.

experiment, the reflected wavefront emulates just the desired phase function.

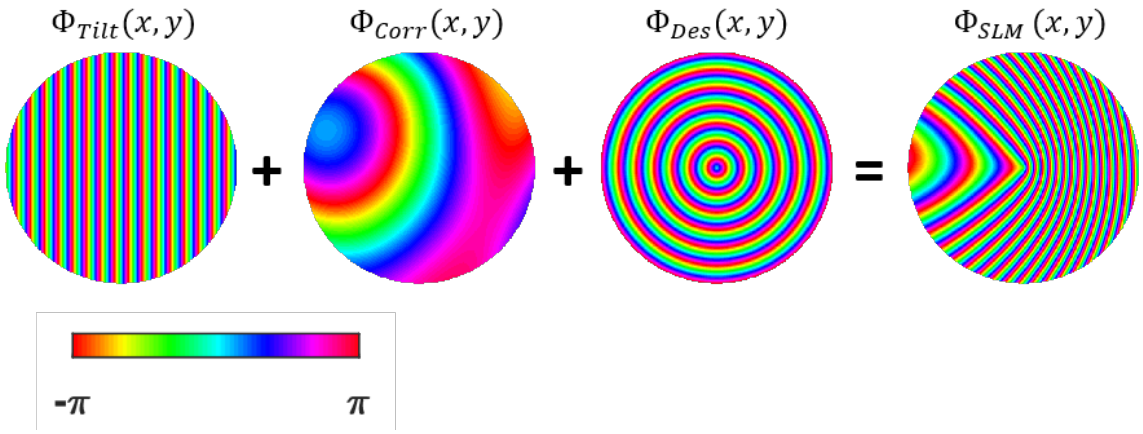


Figure 3.10: Sum of tilt correction, aberration correction, and desired phase functions to produce phase on SLM. The sum creates the desired phase function in experiment.

## 3.3 Experimental Validation

An experiment is performed to observe the performance of the phase masks from Eq. 1.14 using the setup shown in Fig. 3.1. Five images of the laser spot with only the sawtooth

function are recorded and averaged to be treated as the diffraction limited imaging performance. The same is repeated with the desired phase function added to the SLM. These images represent the PSF of the system.

The experiment is first performed with the axicon, vortex, and cubic phase functions with $a = 40$, $b = 15$, and $m = 20$ as these each provide the same theoretical laser suppression of 0.02. The phase patterns, along with their experimental and theoretical PSF's and MTF's, are shown in Fig 3.11.

While the expected laser suppression is 0.02, the measured suppression using the images from Fig. 3.11 varied and are shown in Tab. 3.2.

| Vortex | Axicon | Cubic $0^o$ | Cubic $45^o$ |
|---|---|---|---|
| 0.0216 | 0.0155 | 0.0175 | 0.0184 |

Table 3.2: Measured laser suppression. See peak intensities of Fig. 3.11 (k-o).

The target used in the experiment is a transmissive Air Force bar target. The target is rear illuminated by a diffuse halogen lamp and filtered by a laser line filter to ensure quasi-monochromatic light as the SLM is wavelength sensitive. The target and laser are imaged simultaneously with each of the phase functions along with the sawtooth function. The resulting images are deconvolved with their respective measured PSF's.

The detected and restored results are shown in Fig. 3.12. The images are displayed on a log scale to show faint noise artifacts that are difficult to see. Fig. 3.12 (a) and (f) are the detected and restored images of the no phase case and represent the peak imaging capabilities of the system. The no phase detected image was deconvolved to provide a fair comparison for each of the modulated phases cases. The vortex and axicon cases show ringing artifacts around the bars and are more prevalent around the restored laser spot. This is attributed to the nulls in the MTF. The artifacts around the laser spot for both

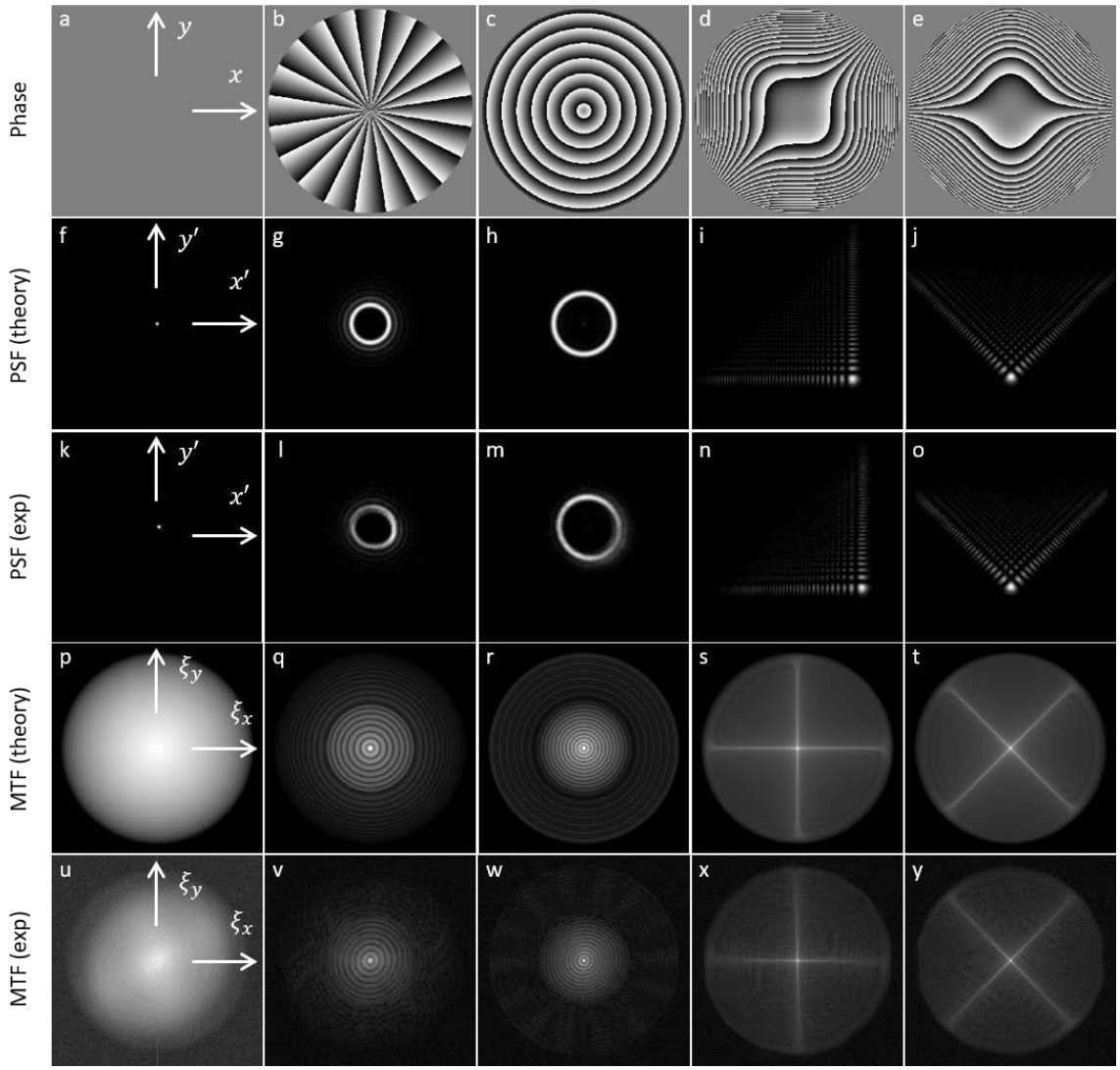


Figure 3.11: Pupil plane phase profiles (a-e) for no phase, vortex, axicon, cubic, and rotated cubic. Corresponding theoretical (f-j) and experimental (k-o) PSF's and theoretical (p-t) and experimental (u-y) MTF's. The MTF's are gamma corrected to aid the eye.

cubic cases are much smaller and have less of an effect on the image. There also appears to be less background noise which can be observed by looking at the uniformity of the bars and of the dark regions of the images. In terms of target resolution, there is no obvious difference between the images qualitatively.

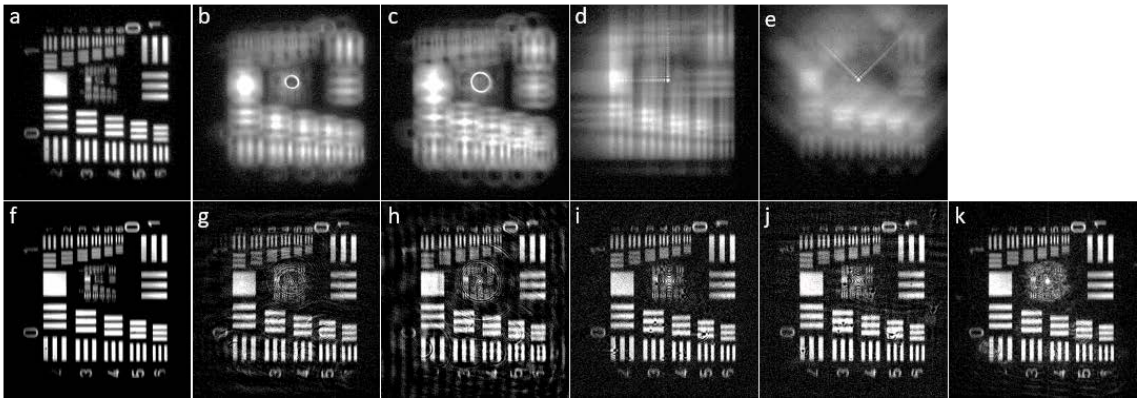


Figure 3.12: Experimentally recorded images using a) no phase, b) vortex, c) axicon, d) cubic, and e) rotated cubic masks. Corresponding restored images (f-j) and joint deconvolution (k). Images are gamma corrected to aid in viewing artifacts in the dark regions of the images and around the laser spot.

The vortex and axicon detected images and PSF's were combined to create a joint restoration using Eq. 2.26. The resulting image is shown in Fig. 3.12 k. While there are more artifacts around the laser spot, there are much fewer artifacts around the bars and in the dark regions of the image. The artifacts around the laser spot show that there may be noise artifacts in the coherent light not accounted for. The dampening parameter, $\gamma(\xi_x, \xi_y)$ is also much smaller than $1/SNR(\xi_x, \xi_y)$ for both the vortex and axicon case which leads to a much brighter laser spot for the joint reconstruction. The intensity of the artifacts versus the peak brightness of the laser spot is lower for that of the joint reconstruction then it is for the vortex or axicon.

Quantitative measures of the final image quality are necessary to give a more rigorous

comparison of each mask's performance. Observing the images, both the resolution of the system and the added noise are important measures for the system. The General Image Quality Equation (GIQE) seeks to combine these metrics into a single quantity [61] with $GIQE = c_1 + c_2 \times log_{10}(RER/GSD) - c_3 \times H - G/SNR$ where $c_1$, $c_2$, and $c_3$ are scalar coefficients, $RER$ is the relative edge response, $GSD$ is the distance between samples in the scene, $H$ is the edge overshoot and $G$ is the noise gain. This metric relies on subjective testing and was not intended for PSF's whose performance varies depending on the angle of the edge. In this report, the edge response and noise gain are presented separately.

To quantify the system resolution, the relative edge response is measured. Using the line profile of the bars from Fig. 3.13, the maximum slope of the right most edge is taken. The relative edge response is then calculated as the slope for the modulated cases divided by the unmodulated case. The value is expected to be between 0 and 1, with 0 having the bars blurred uniformly over the image and 1 a perfect reconstruction of the diffraction limited image. To quantify the noise gain, an RMS error was measured. Using the area of the square from Fig. 3.13, the RMS error is calculated as

$$\text{Noise Gain} = \sqrt{\sum (I-1)^2}/N \tag{3.4}$$

where $I$ is the intensity at a given pixel and $N$ area the number pixels in the are of the square. The error of each mask was divided by the error of the unmodulated case. This value is expected to be greater than 1 and provides a measure of how much greater the noise is for this system than the diffraction limited system. A larger value represents a worse image with more noise. The edge response and noise gain are shown in Fig. 3.14.

The average line profile of the bars and a line profile of the square are both shown in Fig. 3.13.

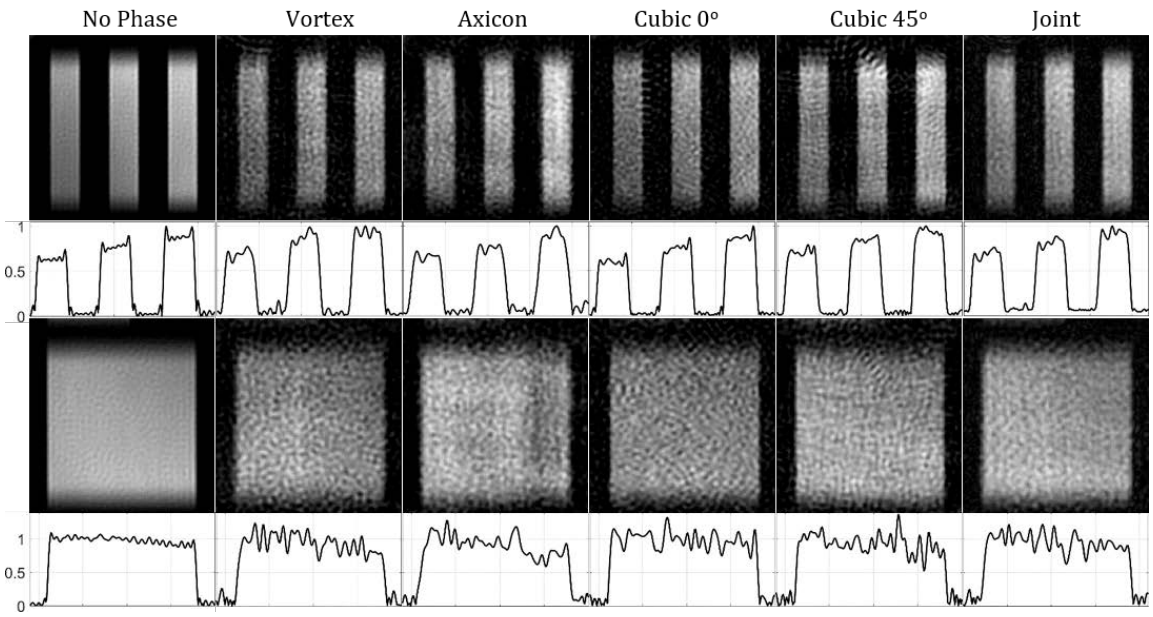


Figure 3.13: Same as Fig. 3.12, zoomed view of upper right hand bars (top) and middle left solid square (bottom), along with corresponding normalize line profiles.

As expected, the cubic phase mask, which has an MTF that performs best along the horizontal and vertical edges of the bar target, produces the greatest edge response. The vortex, rotated cubic, and the joint case each perform similarly. Each of the vortex, axicon, and cubics have similar noise gain. The vortex and axicon, however, will produce greater low frequency noise which is more prevalent to a human observer. The noise is apparent in the line profiles for the squares shown in Fig. 3.13. The joint case produces the lowest noise gain which supports the new deconvolution method for removing nulls in the MTF.

## 3.4 Summary

In this chapter, an experimental testbed was designed to validate the theoretic imaging system. A distant scene combining a diffuse and incoherent object was combined with a

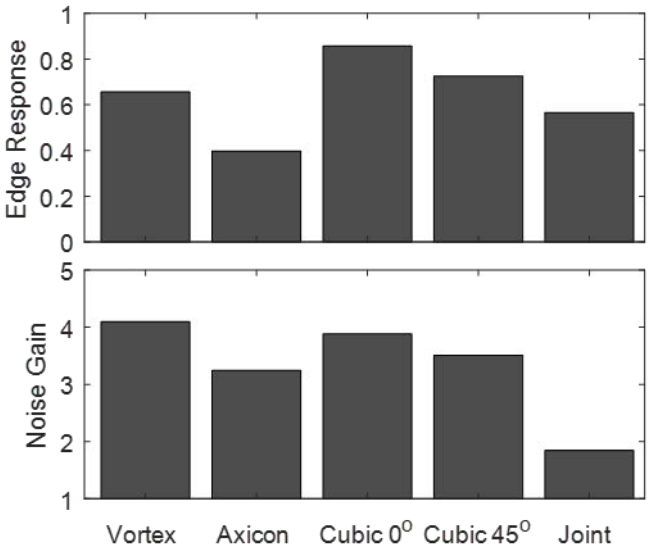


Figure 3.14: The relative edge response and noise gain measurements with each mask, showing improved noise suppression in the joint case.

powerful laser source using a beam splitter. The pupil with an arbitrary phase function was tested using a phase-only SLM. Challenges associated with the SLM which would not be present in the theoretic system including zero-order diffraction, limited field of view, and added aberrations were discussed and overcome.

The experimental setup was implemented to image a resolution bar target with the previously know phase functions: axicon, cubic, and vortex. The cubic was shown to provide the greatest imaging fidelity with the lowest noise gain giving evidence an odd phase function is advantageous over an even one. Exposures from the axicon and vortex phase function were combined through a joint deconvolution operation, allowing for their respective nulls to be compensated by one another. The result was a significant improvement in noise gain over each of the individual reconstructions.

In total, the experimental setup was shown as a success with each of the phase masks

providing the expected PSFs and blurred images. Each reconstructions resulted in images with suitable fidelity. Suffice to say that for each of the images, it is the goal to improve upon the performance of these masks either in significantly lower $LSR$ or a high imaging fidelity.

# Chapter 4

# Pupil Phase Optimization

Using knowledge of PSF engineering, an optimal phase mask is sought which maximizes the post-processed imaging fidelity for a fixed $LSR$. Using the integrated Strehl ratio as a quantitative metric of image quality, numeric and analytic approaches are taken to produce a desired phase mask. Simple techniques are not sufficient for optimizing the phase mask. Consider a basis set consisting of:

$$\Phi_1(r,\theta) = v_1 \times 2\pi \frac{r}{R} cos^3[\theta] \tag{4.1a}$$

$$\Phi_2(r,\theta) = v_2 \times 2\pi \frac{r}{R} cos^5[\theta] \tag{4.1b}$$

where $v_1$ and $v_4$ are scalar constants, $r$ and $\theta$ are the radial and azimuthal coordinates, and $R$ is the aperture radius. The values for $Strehl$ and $LSR$ can then be calculated for the pupil function $exp[i(\Phi_1(r,\theta) + \Phi_2(r,\theta))]$ and in turn the ratio $Strehl/LSR$ may be calculated. The values for $Strehl/LSR$ are shown as a function of $v_1$ and $v_2$ in Fig. 4.1.

This "topology" map for $Strehl/LSR$ shows a peak value for the basis set at $v_1 = 17.4$

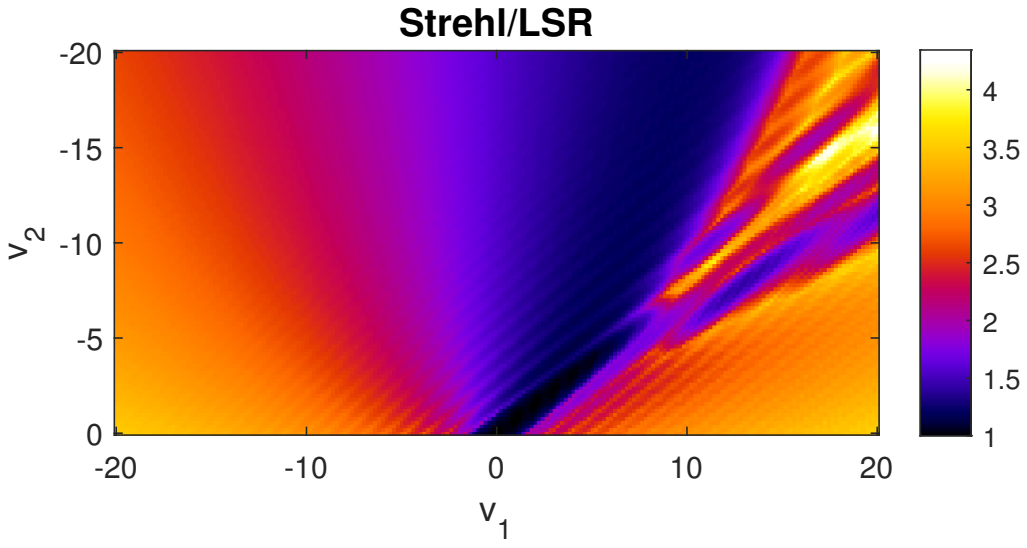


Figure 4.1: The value for the ratio $Strehl/LSR$ as a function of $v_1$ and $v_2$ given the phase functions in Eq. 4.1. The maximum value occurs in a region that a numeric gradient descent algorithm would not find unless the starting point was near the maximum.

and $v_2 = -14.8$. Because of the complexity of the topology map, numeric algorithms which rely on the calculation of the gradient around the initial guess such as the SPGD described in Sec. 3.2.2 or a Nelder-Mead optimization [83] would be unable to optimize to this solution. For example, if the initial guess had a negative value for $v_1$, the algorithm would seek a more negative value for $v_1$. For three or more basis functions, these solution spaces become even more complex. Because of this, a more advanced global optimization algorithm is required to find the ideal phase function.

In this chapter two numeric algorithms are implemented to optimize a set of basis functions: a differential evolution algorithm to optimize numerically and a simulated annealing algorithm to optimize in experiment. Odd functions are chosen as the basis functions for these optimizations to improve the Strehl ratio and reduce the number of zeros in the MTF (Sec. 2.2).

In addition to the numeric algorithms, another method is implemented where the PSF was designed using desirable traits. The inverse problem of finding the pupil function which creates the PSF is solved. The result is a new family of high performing PSFs called the half ring PSFs.

The optimized PSF from the differential evolution algorithm, the simulated annealing experiment, and the inverse problem method were each tested experimentally to image two diffuse targets in the presence of laser. Each mask was shown to successfully image the objects while suppressing the laser source by 3 orders of magnitude. The half ring PSFs were shown to provide the highest quality reconstructions.

## 4.1 Global Optimization: Differential Evolution

A differential evolution algorithm [84, 85] is implemented to optimize both image quality and coherent source suppression. Differential Evolution is a global optimization technique that is not limited by the region near an initial guess. This is needed as the relationship between image quality and suppression contains many low performing local minima.

To quantify the imaging performance with pupil-plane phase masks, the Strehl ratio ($Q_A$) and modified Strehl ratio ($Q_B$) is used

$$Q_A = \int\int |H(\xi_x, \xi_y)| d\xi_x d\xi_y / \int\int |H_0(\xi_x, \xi_y)| d\xi_x d\xi_y \tag{4.2}$$

$$Q_B = [\int\int (|H_0(\xi_x, \xi_y)|/|H(\xi_x, \xi_y)|) d\xi_x d\xi_y]^{-1} \times \pi R^2 \tag{4.3}$$

where $H_0(\xi_x, \xi_y)$ is the diffraction-limited OTF and $R$ is the aperture radius. The modified Strehl ratio weighs specific spatial frequencies comparatively to the diffraction-limited MTF and also has a greater penalty for near-zero values at specific frequencies by using an inverse relationship unlike the standard Strehl ratio.

Suppression, defined as how much the peak intensity of the point source is reduced by the introduction of the phase mask, may be represented by the suppression ratio, $I/I_0$. Both the image quality suppression ratios are combined into a single cost function

$$C = \alpha/Q + \beta|I_g - I/I_0|^2 \tag{4.4}$$

where $\alpha$ and $\beta$ are scalar weights, $I_g$ is the desired laser suppression, and $Q$ is the desired image quality metric. The goal is to minimize the cost by achieving higher values for image quality and a suppression close the the goal value. During the progression of the algorithm,

early iterations will have the suppression term dominating the value of the cost function due to the parabolic relationship. As the suppression approaches the goal value, the image quality metric becomes dominant. A higher value for $\beta$ causes the algorithm to reach the goal suppression value quicker, but reduces the tolerance of the image quality. The scalar weight parameters are tuned to achieve a higher convergence rate of the final algorithm which produce low values of the cost function.

The differential evolution algorithm is shown in detail through pseudocode in Algorithm 1 and in Ref. [84]. A set of random vectors act as inputs to the differential evolution algorithm. The components of these vectors correspond to inputs of the desired basis functions. The cost associated with each of these vectors is calculated by Eq. 4.4. The population is varied through mutation and crossover operations to create new vectors. These replace the original if the cost is reduced. The algorithm converges when the average cost for the entire population is equal to the minimum cost of the population which occurs when each vector in the population has an equivalent cost.

The output is an input vector for the given basis function which minimizes the cost function. This output is then used as the input of a Nelder-Mead minimization algorithm to find the local minimum to further improve the result [83]. The result is the local minimum near the output vector of the Differential Evolution algorithm that further improves the mask.

Four implementations of the algorithm were conducted with varying input parameters. For the algorithm, the following phase functions were chosen:

$$\Phi_1(x,y) = v_1 r/R + v_2(r/R)^3 cos(3\theta + v_3) \tag{4.5a}$$

**Algorithm 1** Differential Evolution

**Inputs:** $P$, the initial population, $b$, length of vector in population, $s$, the size of the population, g, the maximum generation **Outputs:** $v_{min}$, the basis vector with minimum cost

**begin**
$V \leftarrow P$
**for** $j = 1 : g$ **do** ▷ loop until maximum generation
  $r_1 \leftarrow$ random vector from V
  $r_2 \leftarrow$ random vector from V
  $r_3 \leftarrow$ random vector from V
  $m = r_1 - 0.9(r_2 - r_3)$ ▷ mutation
  **for** $k = 1 : s$ **do** ▷ for each population vector
    **for** a $= 1 : b$ **do** ▷ for each vector component
      **if** rand $< 0.5$ **then** ▷ crossover
        $w(a) \leftarrow v_k(a)$ ▷ $v_k$, the $k$th vector in $V$
      **else**
        $w(a) \leftarrow m(a)$ ▷ $w$, a candidate vector
      **end if**
    **end for**
    **if** cost[w] $<$ cost[$v_k$] **then** ▷ calculated from desired cost function
      $v_k \leftarrow w$
    **end if**
  **end for**
**end for**
$v_{min} \leftarrow Minimum(V)$
**return** $v_{min}$

$$\Phi_2(x,y) = [v_1 r/R + v_2(r/R)^2][v_3 cos(\theta) + v_4 cos(3\theta) + v_5 cos(5\theta) + v_6 sin(\theta) + v_7 sin(3\theta) + v_8 sin(5\theta)] \quad (4.5b)$$

$$\Phi_3(x,y) = v_1[sign(x)x^2 + sign(y)y^2] + v_2(x^3 + y^3) + v_3[sign(x)x^4 + sign(y)y^4] + v_4(x^5 + y^5) \quad (4.5c)$$

| Mask | 1 | 2 | 3 | 4 |
|---|---|---|---|---|
| **Input Parameters** | | | | |
| Basis | $\Phi_1$ | $\Phi_2$ | $\Phi_2$ | $\Phi_3$ |
| Quality Metric | $Q_A$ | | $Q_B$ | $Q_A$ |
| $\alpha$ | 1 | | | |
| $\beta$ | $10^6$ | $10^7$ | $10^5$ | $10^7$ |
| $I_g$ | 0.01 | | | |
| Population | 20 | | | |
| **Evaluation Parameters** | | | | |
| Max Iterations | 500 | 3987 | 1496 | 1285 |
| Cost after DE | 13.29 | 13.49 | 3.31 | 14.14 |
| Cost after NM | 13.26 | 13.02 | 3.29 | 14.14 |
| $Q_A$ | 0.076 | 0.077 | 0.065 | 0.071 |
| $Q_B$ | 0.30 | 0.38 | 0.31 | 0.28 |

Table 4.1: Parameters and results for each implementation of the Differential Evolution algorithm. Both the Strehl ratio ($Q_A$) and the new modified Strehl ($Q_B$) are reported even though the results were optimized for a single metric.

The functions weer chosen to prevent an even pupil function which result in additional nulls and potentially low SNR. The other input parameters: basis, population size, maximum generation, image quality metric, goal suppression, and scalar coefficients are shown in Table. 4.1. The resulting costs after Differential Evolution (DE), Nelder Mead (NM), and the quality metrics after Nelder Mead are also shown.

The final optimized phase mask for each implementation is visualized in Fig. 4.2. Their respective incoherent PSF's and MTF's are also shown. The diffraction-limited mask, Fig. 4.2a, represents the system with no phase function where $t(x, y) = 1$ and also represents the peak imaging performance of the system. The PSFs resulting from the optimized masks are shown in Fig. 4 g-j. The PSF spatial extents are similar, with Fig. 4 i being much larger than the others. The larger PSF's may lead to the blurred images bleeding over the edge of the sensor – losing information of the scene. The setup was

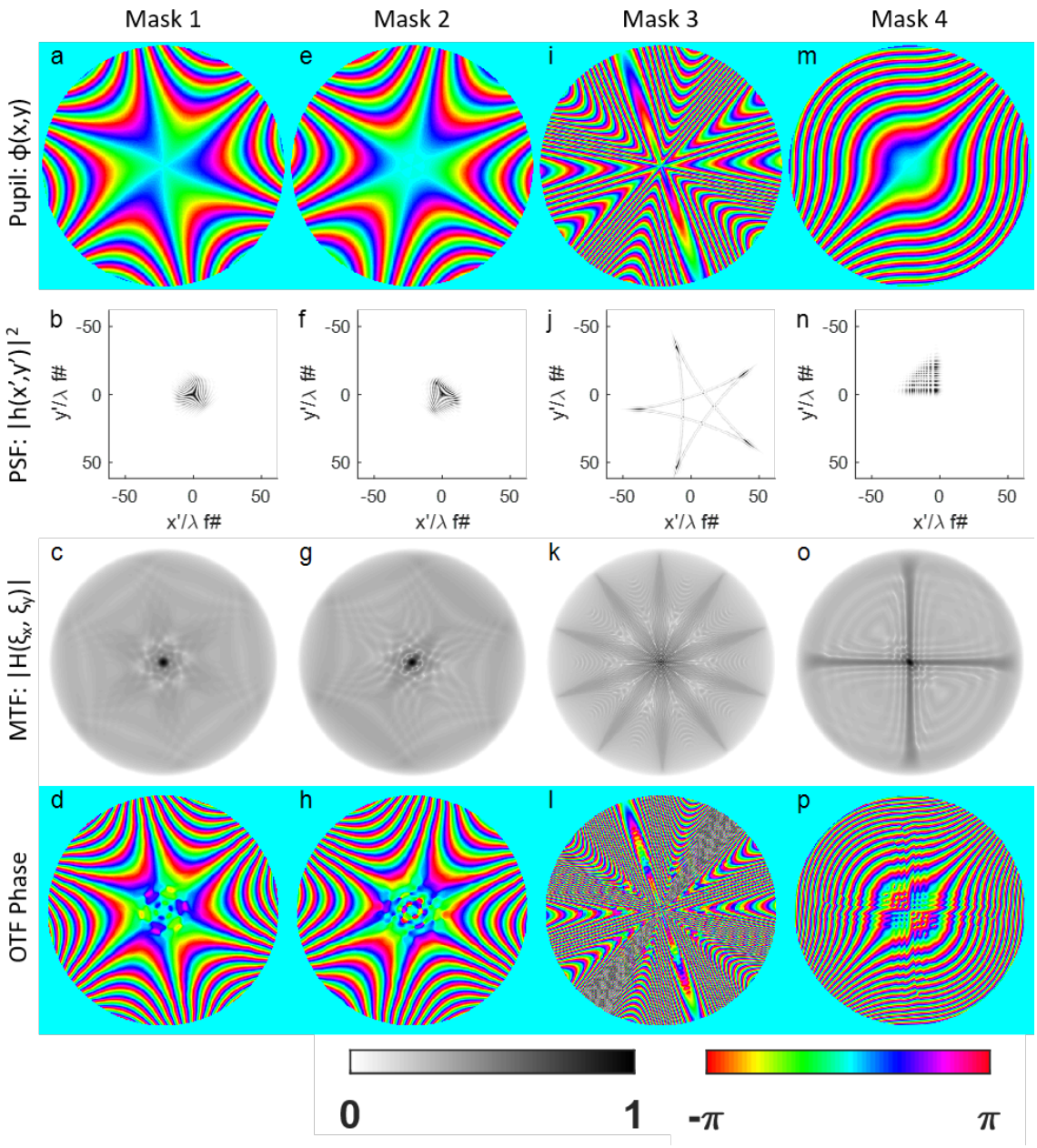


Figure 4.2: Simulated images of the phase functions (a-e), PSF's (f-j), MTF's (k-o), and OTF phases (p-s). These are shown for the no phase case as well as the four optimized masks.

specifically designed such that the background image and laser PSFs did not overfill the sensor. Careful consideration should be made for future wavefront coding systems as was done here in order to avoid losing information of the scene.

The MTFs show the impact on the spatial frequency content prior to deconvolution. The MTF for Mask 4, Fig. 4.2 o, has performance that is optimal for two perpendicular lines which allows for a greater image reconstruction for edges in these directions which may be useful if information about the scene is previously determined and the mask can be aligned to it. Mask 3, Fig. 4.2 n, is also directional but for more edges allowing for less precision in potential alignment. Masks 1 and 2 do not have a directional preference but may be better for general performance.

The OTF phases, Fig. 4.2 p-q, have the desired complex phase having both a real and imaginary component, but there are nulls in the OTF's for Masks 2-4 which are evident from the singularities in the OTF phase. Despite the high quality metrics, these nulls may lead a noisy reconstruction for Mask 2 and further deters the use of Mask 3 and 4.

The performance of each of the optimized phase masks is compared to that of the individual phase basis functions. The Strehl, $Q_A$, and modified Strehl, $Q_B$, and suppression were calculated for the axicon, vortex, and cubic examples for varying values of $m$, $a$, and $b$ from Eq. 1.14. Doing so achieves a curve of image quality vs. suppression for each of the individual phase basis masks. This is shown along with the results of the optimized phase masks in Fig. 4.3.

An optimal solution has a greater image quality metric and a lower suppression ratio, resulting in a point towards the top left of Fig. 4.3. A vortex, cubic, or axicon mask of the same suppression ratio as the optimized masks have half the Strehl ratio ($Q_A$). Similarly, to achieve the same image quality, the vortex, cubic, and axicon would have

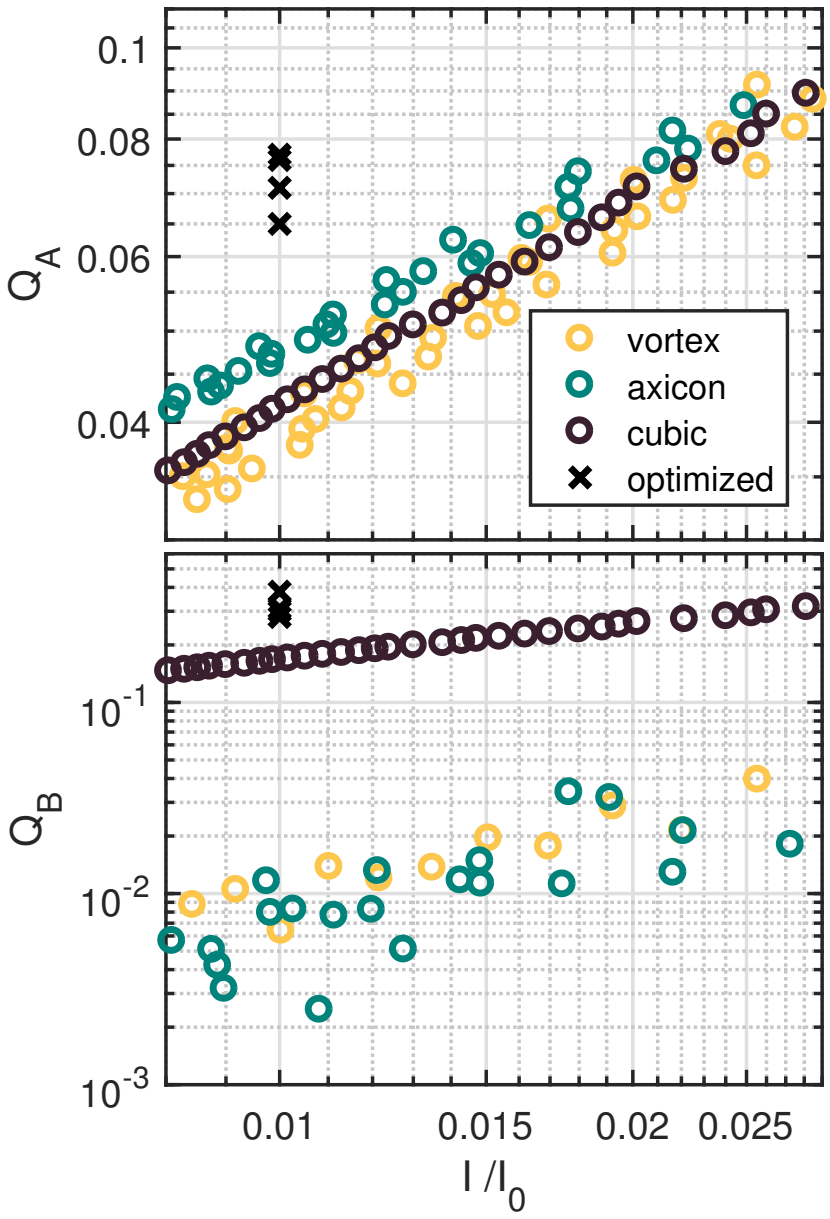


Figure 4.3: The image quality metrics for the optimized phase masks and the phase masks from Eq. 1.14. The values for the vortex, cubic, and axicon masks was calculated by varying the $m$, $a$, and $b$ parameters. The optimized masks are all shown to result in a higher Strehl and modified Strehl than the individual phase basis masks for the same suppression ratio.

twice the suppression ratio. This shows the optimized masks produced by the algorithm outperforms the previously studied masks.

The modified Strehl ($Q_B$) better represents the effect of nulls in the MTF on the final processed image. This result is shown in Fig. 4.3 as the cubic, which has no nulls, outperforms the vortex and the axicon by an order of magnitude. The optimized masks are shown to have twice the the modified Strehl as the cubic phase mask for an equivalent suppression. While optimized masks 2-4 do contain nulls as singularities, there are much fewer than the axicon and vortex. The result shows that for both metric, the optimized masks outperform the individual phase basis functions.

### 4.1.1 Differential Evolution Validation

The same experiment performed in Sec. 3.3 is repeated for the phase masks developed by the Differential Evolution Algorithm. Instead of a resolution bar target, a game token is used to demonstrate imaging an object with some depth of field. The system is first characterized by imaging just a laser point with each of the phase functions on the SLM with 5 images of each averaged. An image of the token and laser present is also taken and deconvolved using the measured PSF. The experimental PSF's, MTF's, blurred detected images and final restored images are shown in Fig. 4.4. To emphasize the difference in the noise artifacts, the blurred and restored images are displayed with their intensities raised to the 0.3 power which accentuates low intensity information for qualitative visual inspection.

Each mask is shown to successfully restore the image of the car with its features still recognizable by a human observer including lower frequency information such as the gradual illumination change on the hood and higher frequencies such as the grill and the surface textures. There is added noise from the deconvolution which is visible in the dark regions.

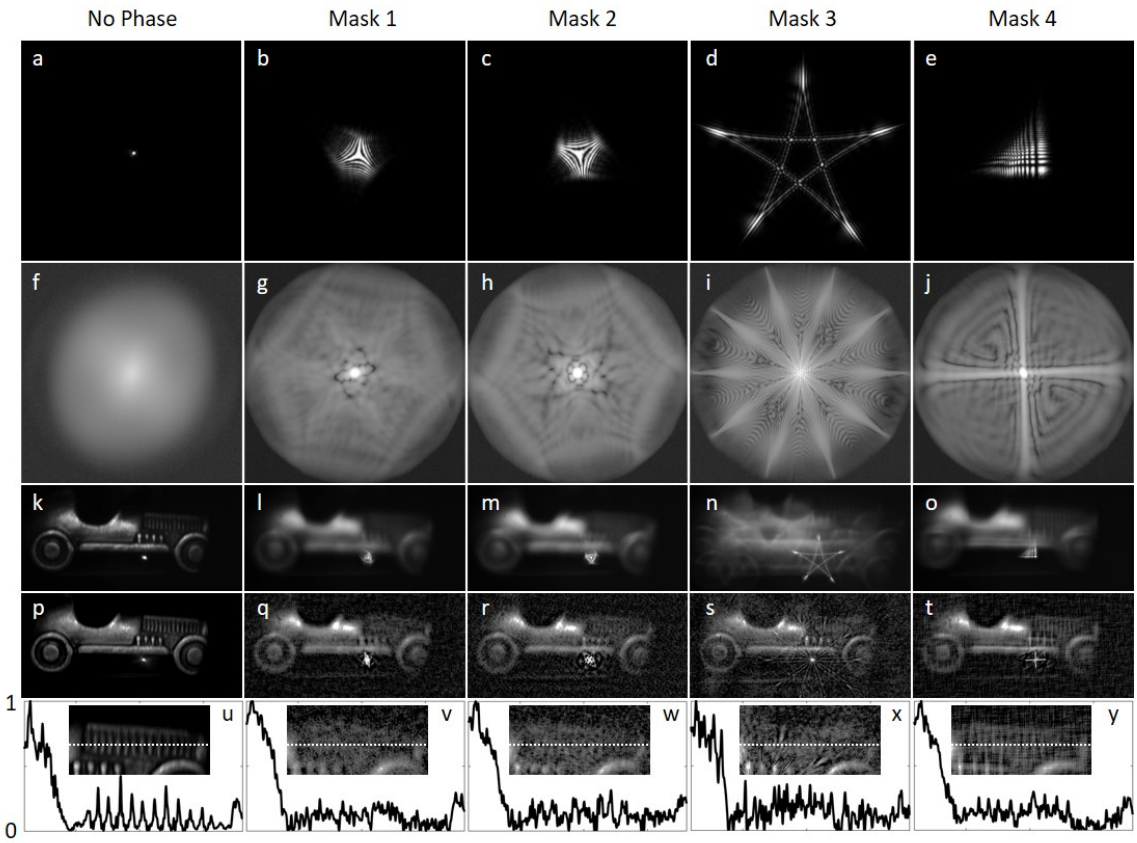


Figure 4.4: The experimental results achieved with no phase on the SLM and with each of the four optimized phase masks. The PSF's (a-e) recorded from imaging the spatially filtered laser spot. The MTF's (f-j) were calculated as the Fourier transform of their respective PSF's. The detected blurred images (k-o) and the images restored via Wiener deconvolution (p-t). Line profiles of the high frequency grill normalized to have maximum intensity of 1 and minimum of 0 (u-y).

Ignoring the noise artifacts, the recovered image using Mask 3 has finer features and sharper edges than the other processed images. It is difficult to determine subjectively though which mask produces the best reconstruction of the object and which preserves the most detail.

A horizontal line profile of the high frequency grill region is shown in Fig. 4.4 u-y for the no phase case and each of the optimized masks. The no phase case shows the expected high frequency pattern. These features are only visible for mask 4 whose SNR is greatest for horizontal and vertical edges. For masks 1-3, it is difficult to distinguish features from the noise floor. Mask 3 has a greater noise than either of mask 1 or 2.

The Strehl and modified Strehl were calculated using the experimentally calculated OTF's in Fig. 4.4. The results are shown in Fig. 4.5. Both the Strehl and modified Strehl

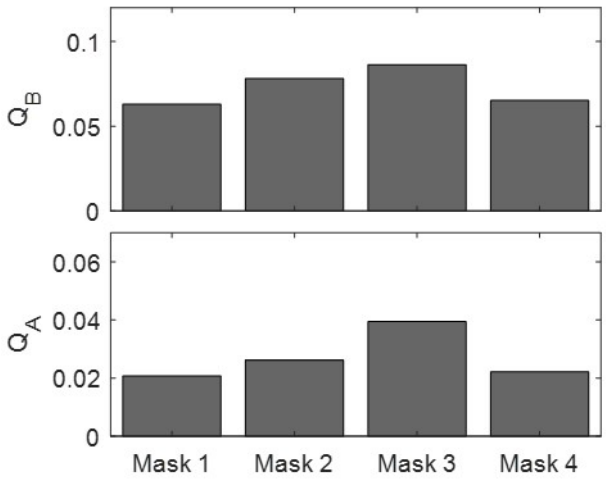


Figure 4.5: Plots of the Strehl ($Q_A$) and modified Strehl ($Q_B$) for each of the four optimized phase masks which were calculated from the experimentally obtained MTF's.

follow similar trends with Mask 3 being the highest performer. This matches the qualitative analysis. Despite this, Mask 3 has more noise in the image.

**Differential Evolution Discussion**

Four masks were designed using different input parameters of a differential evolution algorithm with each reducing the peak intensity of a point source by a factor of 100. They each also outperformed previously tested masks in terms of two metrics: Strehl and modified Strehl. The latter was designed to penalize nulls in the OTF.

Each mask was also experimentally tested using a phase-only SLM as the pupil mask to image an incoherent object in the presence of a coherent point source. Images of the target were successfully recovered with each mask with varying levels of noise and added artifacts. Using the experimentally recorded PSF's, the expected performance was compared using both metrics. These assessments agreed with a qualitative analysis of the images.

### 4.1.2 Azimuthal Harmonic Phase Functions

One newly defined basis set, the azimuthal harmonic set, outperformed others in the ratio $Strehl/LSR$. The set is defined as

$$\phi(x,y) = \sum_{j=1}^{J} 2\pi a_j r^{j+1} cos(n\theta). \tag{4.6}$$

where $n$ is the azimuthal frequency. This basis set was optimized using the differential evolution algorithm for values of $J$ from 1-5 and $n = 3$ and $n = 5$. The fitness function was redefined as

$$fitness = \begin{cases} Strehl/LSR & LSR \geq 10^{-3} \\ Strehl/10^{-3} & LSR < 10^{-3} \end{cases}. \tag{4.7}$$

As the ratio Strehl/LSR increases for decreasing LSR, the algorithm will converge to a solution such that LSR = $10^{-3}$. The resulting values of Strehl ratio are shown in Fig. 4.6.

The pupil function, PSF, MTF, and phase transfer function for $J = 1, 5$ and $n = 3, 5$ are shown in Fig. 4.7. As more terms are added (a higher value of J), the PSF becomes more evenly illuminated leading to a PSF with a smaller spatial extent.

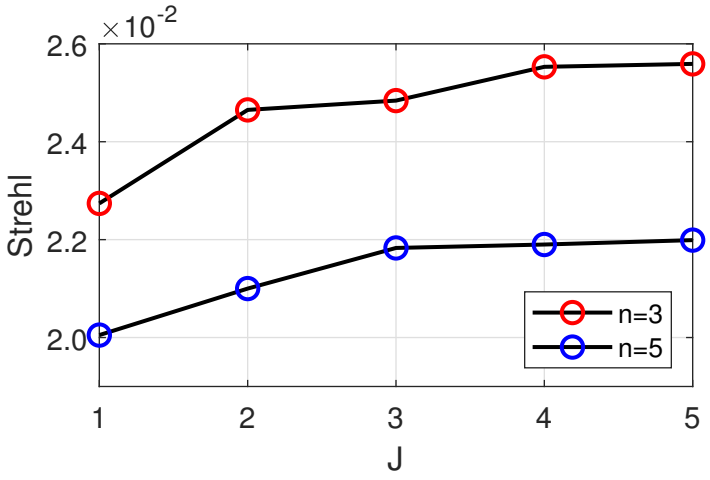


Figure 4.6: The Strehl ratio for the azimuthal harmonic basis set optimized at a value of $LSR$ of $10^{-3}$.

## 4.2 Hardware Based Optimization: Simulated Annealing

A closed-loop feedback system is sought for optimizing the phase mask in experiment. An experiment was designed using the same setup as Sec. 3.1 Fig. 3.1 with only the laser light source. The experimental setup will leverage the SLM to alter the phase and in real time the PSF will be recorded and the cost may be calculated from the image. This method allows for making no assumptions in the relationship between the phase mask in the pupil plane and the PSF in focal plane.

While Differential Evolution provides a robust method for optimizing in simulation, it is unfeasible to perform in experiment as algorithm is computationally expensive and

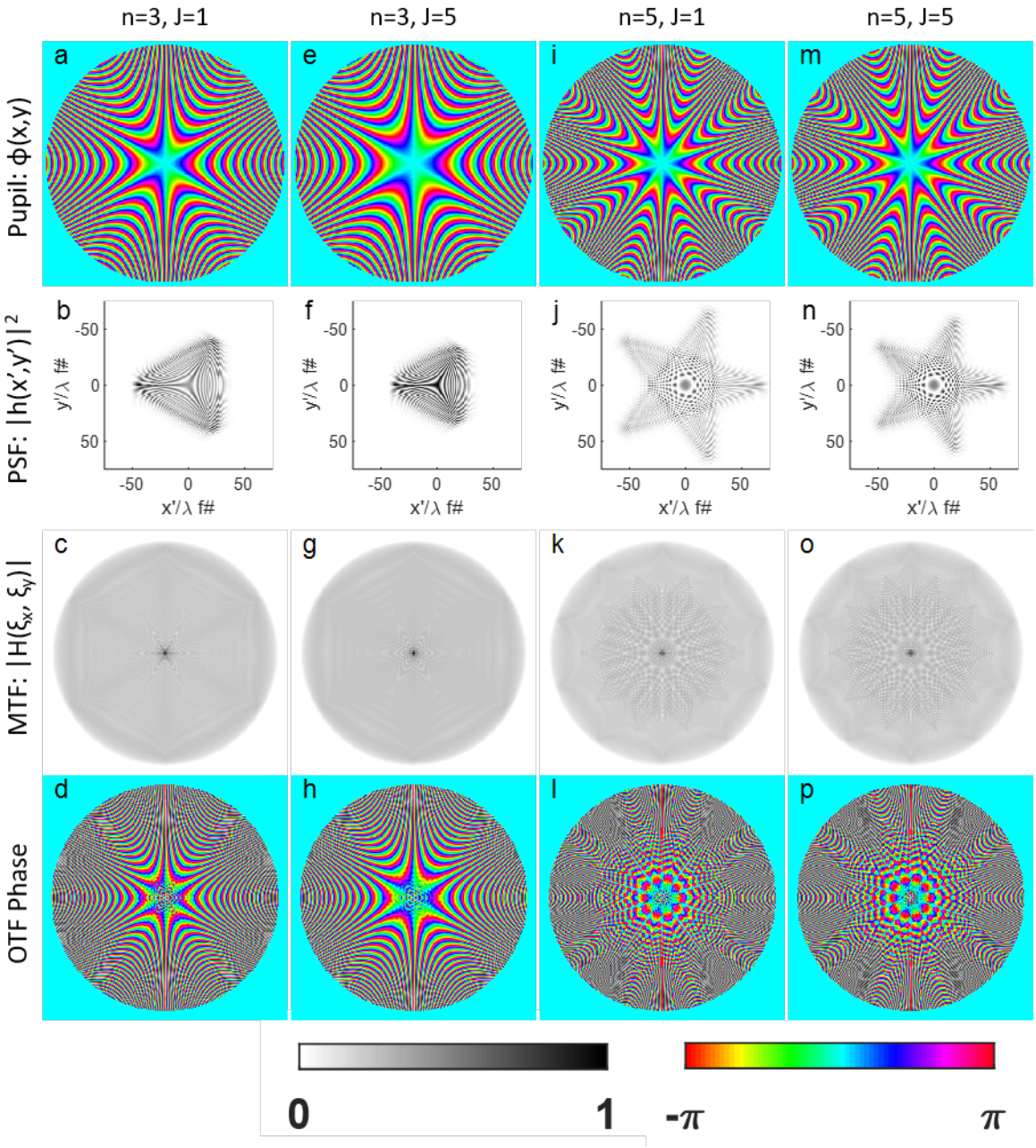


Figure 4.7: Pupil phase, PSF, MTF, and phase transfer functions for the azimuthal harmonic phase functions with $J = 1, 5$ and $n = 3, 5$.

slow. The algorithm requires up to 400,000 Fourier transforms and would be too inefficient to implement in experiment as recording the PSF and calculating quality metrics take in experiment than in simulation. A new global optimization algorithm must be used which is more efficient.

A simulated annealing algorithm is implemented. Simulated annealing is an iterative global optimization routine with similarity to a gradient descent algorithm. The algorithm begins with an input phase on the SLM. An image of the laser spot is recorded and normalized to calculate the PSF and OTF. A small stochastic change is made to the SLM to create a new candidate phase. A new PSF and OTF are recorded and calculated.

The cost from the first image ($Cost_1$) and second image ($Cost_2$) are calculated in the following manner

$$Cost = \begin{cases} -Strehl/I & I \geq 10^{-3} \\ -Strehl/10^{-3} & I < 10^{-3} \end{cases}. \tag{4.8}$$

This cost function measures image quality ($Strehl$), relative to the laser suppression ($I$). The cost will continue to rise as $I$ decreases. To remedy this, the cost function treats all $I < 10^{-3}$ the same which should have the algorithm converge to a laser suppression of $10^{-3}$.

If $Cost_1 + P[Temp] > Cost_2$, then the new candidate phase is passed to the next iteration where $P[temp]$ is a uniform probability distribution ranging from 0 to $temp$. The value $temp$ represents the "temperature" of the system and allows for the phase to move to a higher cost phase or a worse performing intermediate solution which prevents the algorithm from converging to a poor performing local solution. The process is repeated with the temperature reducing linearly with iteration. Once $temp = 0$ the algorithm becomes a gradient descent algorithm and searches for a local minimum of the cost function.

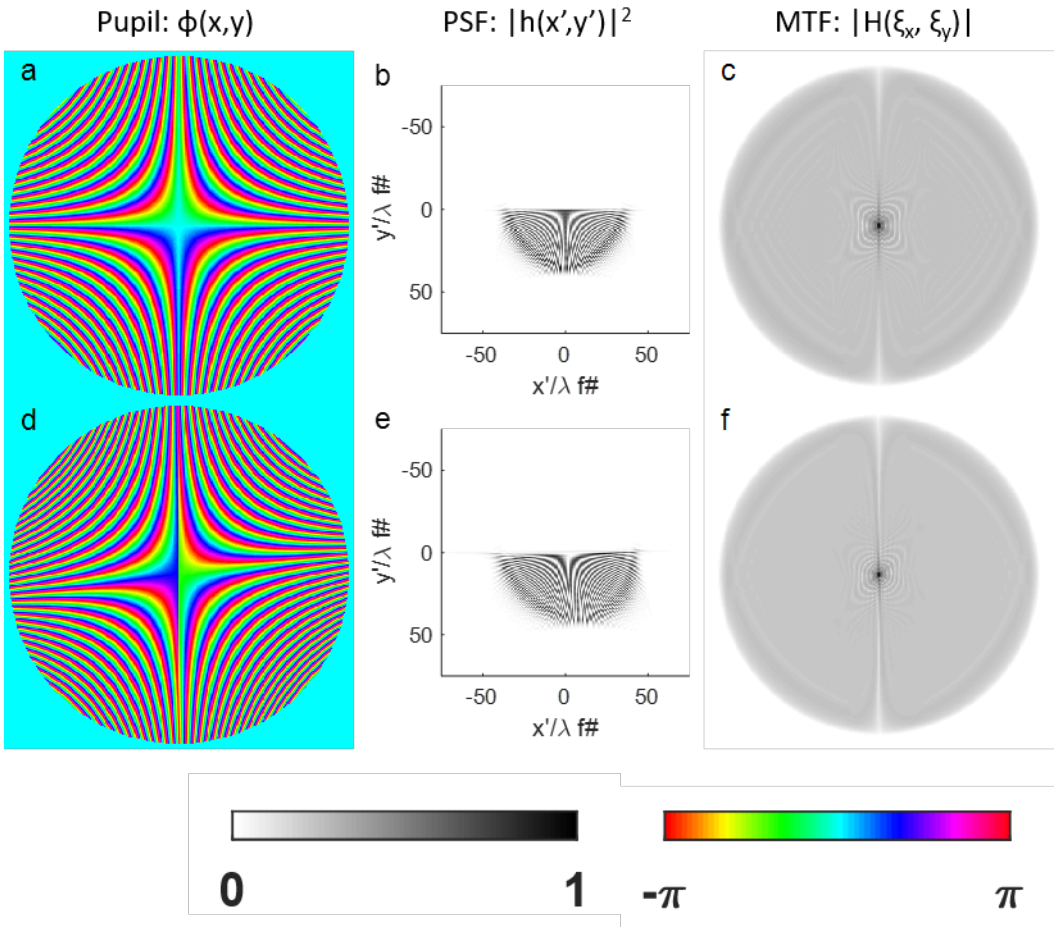


Figure 4.8: The pupil phase, PSF, and MTF of the (a-c) initial and (d-f) final points of the simulated annealing algorithm

A new even half-Zernike basis set is designed using six even Zernike functions (3 second and 3 fourth order polynomials) multiplied by the signum function. The initial phase is $10 \times 2\pi Z_2^2 sign[x]$ and is shown in Fig. 4.8a-c along with its respective PSF and MTF. The algorithm begins with a temperature of 5 and is reduced linearly to 0 over 2500 iterations. The algorithm is followed by 1500 iterations of gradient descent to seek a local minimum.

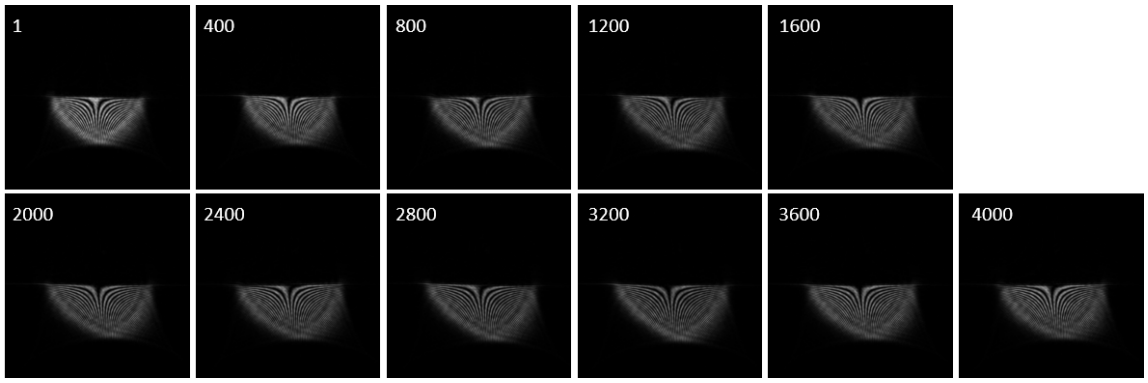


Figure 4.9: Select experimental images of the laser spots for the simulated annealing algorithm. The iteration of the algorithm is shown for each subfigure.

At each iteration, five images of the current and candidate laser spots are recorded, averaged, and normalized to form the current and candidate PSFs. The LSR and Strehl are calculated from the PSFs and a determination if the candidate phase is retained based on the cost and temperature. Select retained images of the laser spot are shown in Fig. 4.9. The Strehl, LSR, and cost (Strehl/LSR) as a function of iteration are shown in Fig. 4.10. The values are calculated using the experimental images. Earlier iterations show more variation in the PSF while the temperature is higher. The final simulated pupil phase, PSF, and MTF are shown in Fig. 4.8 d-f. The experimental Strehl/LSR improved from 20.9 to 25.5, a 22.0% improvement. The Strehl and LSR vary from their expected values due to noise and limited sampling of the images. In simulation, the cost improved from

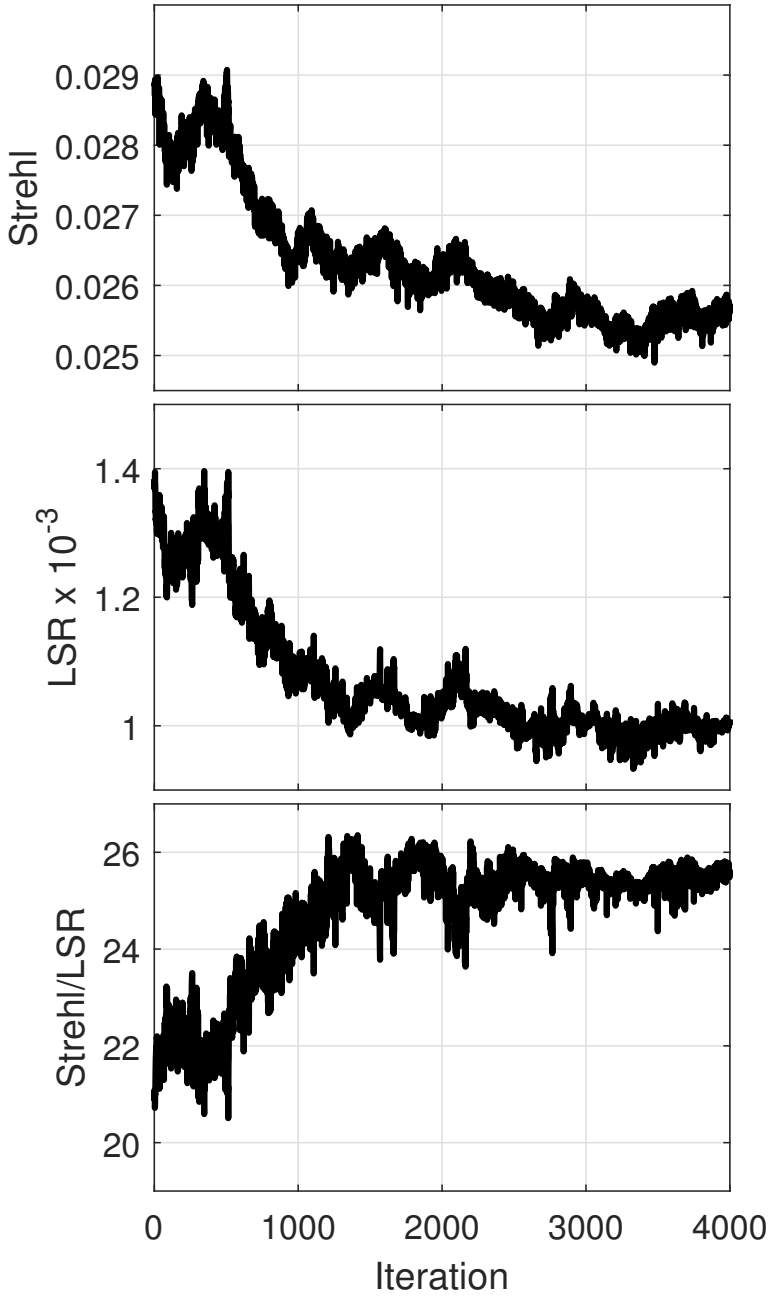


Figure 4.10: Strehl, LSR, and Strehl/LSR as a function of iteration as calculated from the experimental images.

20.2 to 23.0, a 13.8% improvement.

## 4.3 PSF Reverse Engineering

Previous methods for optimizing imaging fidelity involved altering the pupil phase from an input set of basis functions. Aside from limiting to odd basis sets, there are no other known constraints or analytic solutions for producing an optimal phase function. Instead, we look to optimize the PSF and reverse engineer a pupil phase which produces the desired PSF.

In studying PSF engineered systems in Sec. 2.1, we have found that the desired PSF:

1. Has a large integrated odd component
2. Has values close to its peak intensity and zero otherwise
3. Contains narrow features

A half ring PSF is designed to contain these features. It consists of a semi-annulus convolved with the diffraction limited PSF and is defined as

$$|h(r',\theta')|^2 = \frac{1}{2a}|h_0(r',\theta')|^2 \otimes [\delta(r'-a)U(\theta')]. \tag{4.9}$$

where $a$ is the radius of the half ring, $h_0(r',\theta')$ is the no phase PSF, $\delta(r)$ is the two dimensional dirac delta function, and $U(\theta')$ is the step function defined as

$$U(\theta') = \begin{cases} 1 & 0 < \theta' < \pi \\ 0 & otherwise \end{cases}. \tag{4.10}$$

Note that the incoherent PSF is normalized such that $\int\int |h(r',\theta')|^2 r' dr' d\theta' = 1$.

The even and odd components of the PSF are approximately

$$|h_{even}(r',\theta')|^2 = \frac{1}{2\pi a}|h_0(r',\theta')|^2 \otimes \delta(r'-a) \tag{4.11a}$$

$$|h_{odd}(r',\theta')|^2 = \frac{1}{2\pi a}|h_0(r',\theta')|^2 \otimes [\delta(r'-a)G_{odd}(\theta')] \tag{4.11b}$$

where

$$G_{odd}(\theta') = \begin{cases} 1 & 0 < \theta' < \pi \\ -1 & otherwise \end{cases}. \tag{4.12}$$

The half ring PSF along with its even and odd components are shown in Fig 4.11 with a $= 10\lambda f\#$. The even component consists of only positive values while the odd consists of positive and negative values. The odd component has an equal magnitude with the even component which leads to a large imaginary component of the OTF.

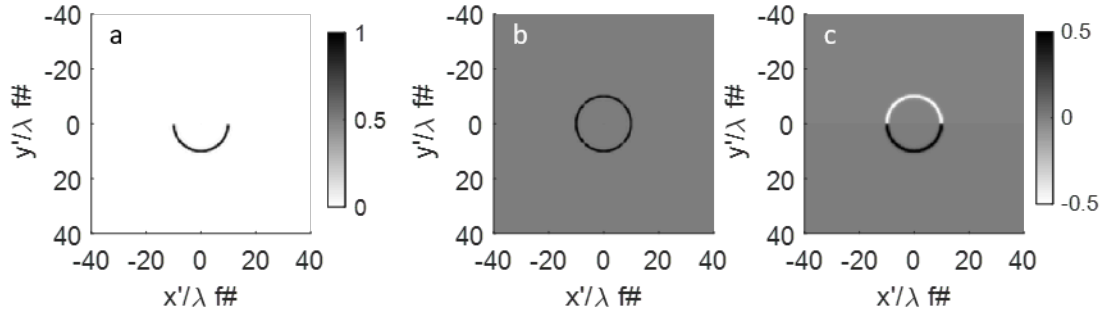


Figure 4.11: a) Half ring PSF with $a = 10\lambda f\#$, b) even component of a, c) odd component of a.

The real and imaginary portions of the OTF may be calculated as the inverse Fourier transforms of the even and odd components of the PSF as

$$FT^{-1}[|h_{even}(r',\theta')|^2] = H_0(\xi_r,\phi)\hat{H}_{real}(\xi_r,\phi) \tag{4.13a}$$

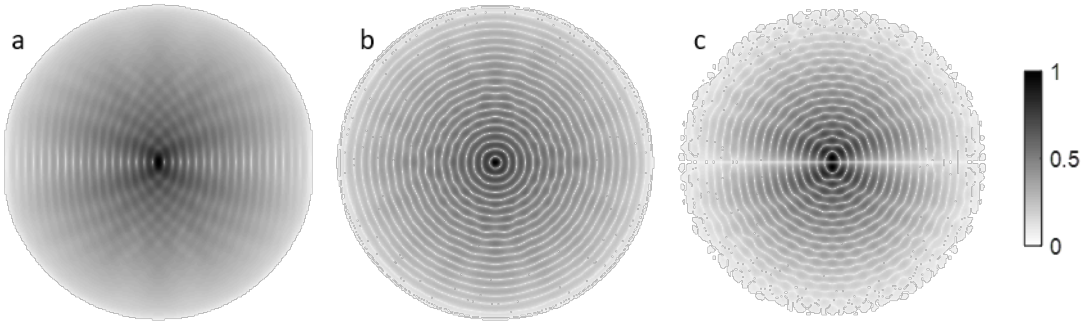


Figure 4.12: a) Half ring MTF with $a = 10\lambda f\#$, b) real component of the OTF, c) imaginary component of the OTF.

$$FT^{-1}[|h_{odd}(r',\theta')|^2] = iH_0(\xi_r,\phi)\hat{H}_{imag}(\xi_r,\phi). \tag{4.13b}$$

The OTF, its real component, and imaginary component for $a = 10\lambda f\#$ are shown in Fig. 4.12.

An additional benefit of the half ring PSF is the limited number of nulls in the OTF. Zero crossings, locations where a function transitions from positive to negative value or vice versa, give the location of the nulls. Finding these spots for the real and imaginary components of the OTF and finding where these spots match give the nulls of the half ring PSF. These spots where found numerically and are shown in Fig. 4.13. The nulls of the half ring PSF are limited to a single edge, and unlike the simulated annealing output, are only found in a finite number of locations and not a continuous line.

The OTF of the half ring PSF may be calculated analytically. For the even component, the Fourier transform is calculated by a zero order Hankel transform as

$$\hat{H}_{real}(\xi_r,\phi) = FT[\delta(r'-a)] = 2\pi\int_0^\infty \delta(r-a)J_0(2\pi f_r r')r'dr' = 2\pi a J_0(2\pi f_r a). \tag{4.14}$$

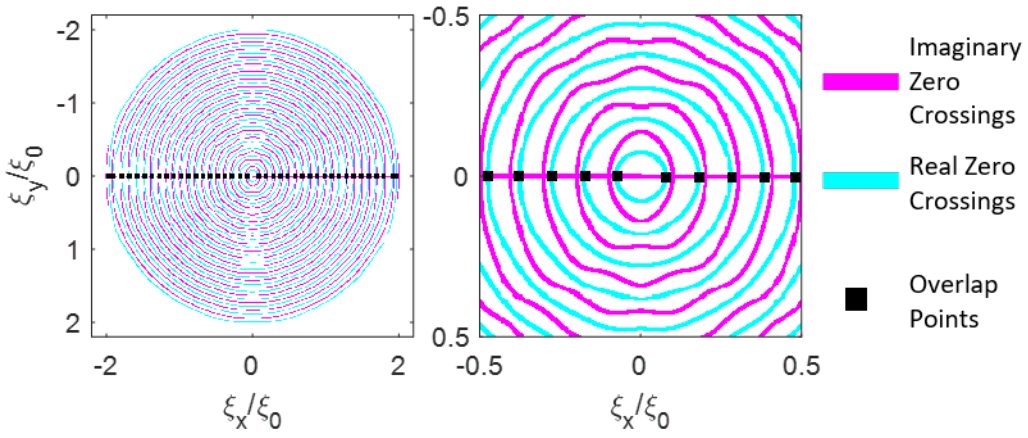


Figure 4.13: Locations for the zeros crossings of the real and imaginary component of the half ring OTF for a = $10\lambda f\#$. Locations where these two cross represent the nulls of the OTF and are also displayed.

For the odd portion, the step function, $G_{odd}(\theta')$, is expanded to the Fourier series

$$G_{odd}(\theta') = \sum_m g_m sin(m\theta') \tag{4.15}$$

where

$$\begin{aligned} g_m(\theta) &= \int_{-\pi}^{\pi} G_{odd}(\theta) sin(m\theta) d\theta = \int_0^{\pi} sin(m\theta) d\theta - \int_{-\pi}^{0} sin(m\theta) d\theta \\ &= 2\int_0^{\pi} sin(m\theta) d\theta = \begin{cases} 4/m & m\ odd \\ 0 & m\ even \end{cases}. \end{aligned} \tag{4.16}$$

The odd portion may be expressed as

$$\begin{aligned}
\delta(r'-a)G_{odd}(\theta') &= \sum_{m=0}^{\infty}\frac{4}{2m+1}sin[(2m+1)\theta']\delta(r'-a) \\
&= \sum_{m=0}^{\infty}\frac{2}{i(2m+1)}[e^{i(2m+1)\theta'}-e^{-i(2m+1)\theta'}]\delta(r'-a) \\
&= \sum_{m=0}^{\infty}\frac{2}{i(2m+1)}e^{i(2m+1)\theta'}\delta(r'-a) \\
&\quad + \sum_{m=0}^{\infty}\frac{2}{i(2m+1)}e^{-i(2m+1)\theta'}\delta(r'-a). \qquad (4.17)
\end{aligned}$$

The Fourier transform of a circularly symmetric function may be calculated as (See Appendix A)

$$FT[\sum_m f_m(r)exp(m\theta)] = 2\pi\sum_m i^m e^{im\phi}\int_0^{\infty} f_m(r)J_m(2\pi\xi_r r)rdr. \qquad (4.18)$$

Combining Eq. 4.17 and 4.18 results in

$$\begin{aligned}
&FT[\sum_m \frac{2e^{i(2m+1)\theta'}}{i(2m+1)}\delta(r'-a)] \\
&\qquad = 2\pi\sum_m \frac{2i^{2m+1}e^{i(2m+1)\phi}}{i(2m+1)}\int_0^{\infty}\delta(r'-a)J_{2m+1}(2\pi\xi_r r')r'dr' \\
&\qquad\qquad = 2\pi\sum_m \frac{2ai^{2m+1}e^{i(2m+1)\phi}}{i(2m+1)}J_{2m+1}(2\pi\xi_r a). \qquad (4.19)
\end{aligned}$$

The value of $i\hat{H}_{imag}(\xi_r, \phi)$ is then

$$
\begin{aligned}
&i\hat{H}_{imag}(\xi_r, \phi) FT[\delta(r' - a) G_{odd}(\theta')] \\
&= 2\pi \sum_m \frac{2a i^{2m+1} e^{i(2m+1)\phi}}{i(2m+1)} J_{2m+1}(2\pi\xi_r a) - 2\pi \sum_m \frac{2a i^{2m+1} e^{-i(2m+1)\phi}}{i(2m+1)} J_{2m+1}(2\pi\xi_r a) \\
&= \sum_m \frac{4\pi a i^{2m+1}}{i(2m+1)} [e^{i(2m+1)\phi} - e^{-i(2m+1)\phi}] J_{2m+1}(2\pi\xi_r a) \\
&= \sum_m \frac{8\pi a i^{2m+1}}{2m+1} sin[(2m+1)\phi] J_{2m+1}(2\pi\xi_r a) \quad (4.20)
\end{aligned}
$$

Combining 4.14, and 4.20 results in the OTF for the half ring PSF as

$$
\begin{aligned}
H(\xi_r, \phi) &= H_0(\xi_r, \phi)[\hat{H}_{real} + i\hat{H}_{imag}] \\
&= H_0(\xi_r, \phi)\{J_0(2\pi f_r a) + \sum_m \frac{4 i^{2m+1}}{2m+1} sin[(2m+1)\phi] J_{2m+1}(2\pi\xi_r a)\} \quad (4.21)
\end{aligned}
$$

The result found in Eq. 4.21 may be validated by comparing to a numerically calculated OTF. A thin half ring PSF from Eq. 4.9 is created in simulation with $a = 10\lambda f\#$. The width of the ring has a thickness of 3 pixels, enough to create a smooth circumference. Trying to make the thickness smaller results in jagged edges and inconsistencies in intensity. The ring is then convolved with the no phase incoherent PSF. The OTF is then calculated by Fourier transform. The OTF is calculated analytically summing 6 Bessel terms from the imaginary portion of Eq. 4.21. The numerically calculated PSF, MTF, and analytically calculated MTF are shown in Fig. 4.14. The numeric and analytic MTFs appear in good agreement.

Line profiles of the OTF for $a = 10\lambda f\#$ are shown in Fig. 4.15. The line profile of the real portion is shown in Fig. 4.15a and the imaginary portion are shown in Fig. 4.15b-e for

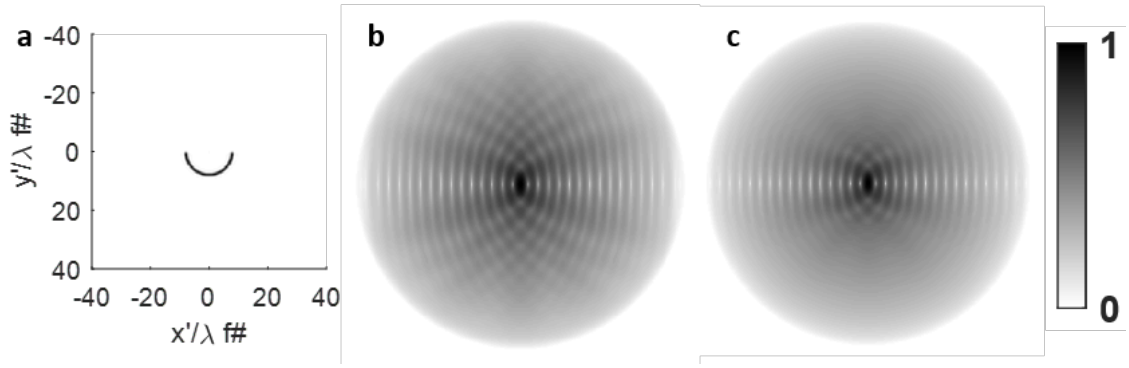


Figure 4.14: a) Numerically calculated half ring PSF with $a = 10\lambda f\#$. b) Numerically calculated MTF. c) Analytically calculated MTF.

3, 6, 9, 16 terms. These line profiles further validate the analytically calculated OTF. In addition, the OTF may be accurately calculated using 9 terms of the imaginary portion as there is little change between the 9 and 16 term line profiles. There may be some disparity between the numeric and analytic OTFs due to the finite thickness used for the PSF in the numerically calculated OTF.

### 4.3.1 Multi Ring PSF

To achieve an LSR of $10^{-3}$, the half ring PSF would need to have a radius $a = 455\lambda f\#$. Such a large PSF would severely limit the field of view of the imager and may not fit on a sensor. Instead, a multi ring PSF is considered consisting of several half rings defined as

$$h(r', \theta') = \frac{1}{2\pi \sum_j a_j} \{h_0(r', \theta') \otimes \sum_j [\delta(r' - a_j) U(\theta' - \hat{\theta}_j)]\} \tag{4.22}$$

where $a_j$ and $\hat{\theta}_j$ are the radius and angular displacement of the $jth$ half ring. Such a PSF would have an LSR scaled by $1/N$ where $N$ is the number of half rings. The OTF is

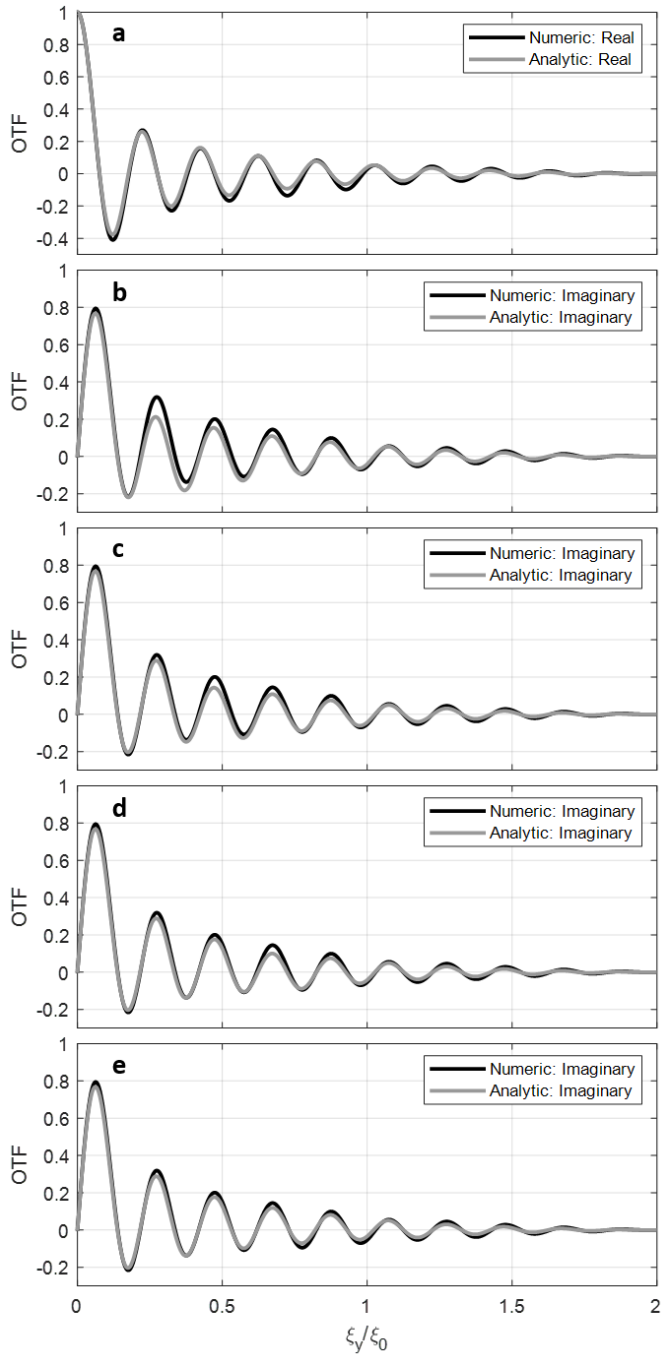


Figure 4.15: a) Line profile of the real portion of the OTF. b) Line profile of the imaginary portion of the OTF calculated with 3 terms, c) 6 terms, d) 9 terms, and e) 16 terms.

calculated similarly to a single half ring as

$$H(\xi_r, \phi) = \frac{1}{\sum_j a_j} H_0(\xi_r, \phi) \sum_j \{a_j J_0(2\pi\xi_r a_j) + \sum_m \frac{4a_j i^{2m+1}}{\pi(2m+1)} sin[(2m+1)(\phi - \hat{\theta}_j)] J_{2m+1}(2\pi\xi_r a_j)\}. \tag{4.23}$$

The multi ring PSF is tested on a 3 ring PSF with radii 5, 10, and 15 $lambdaf\#$ and azimuthal offsets 0, $\pi/4$, and $\pi/2$ radians. The PSF, numerically calculated MTF, and the OTF calculated MTF are shown in Fig. 4.16a-4.16c. The analytic portion is calculated with 9 odd order bessel terms for each ring. Line profiles of the real and imaginary portions of the OTF are shown in Fig. 4.16d and 4.16e. The MTF and line profiles show good agreement between the numeric and analytic OTFs.

The Strehl and LSR of the the multi ring are optimized by altering the radius and angle of the rings. The differential evolution algorithm [84] is used to optimize a five ring PSF. The resulting radii and angular offsets (in radians) are

$$a = [13.6,\ 105.4,\ 111.7,\ 122.0,\ 126.2] \times \lambda f\# \tag{4.24}$$

$$\hat{\theta} = [0.597,\ 0.348,\ 0.367,\ 0.387,\ 0.389]\ radians. \tag{4.25}$$

The PSF and MTF are shown in Fig. 4.17 and has a value for Strehl/LSR of 29.5.

### 4.3.2 Half Ring Pupil Phase

The pupil phase required to create the half ring PSFs is unknown. An inverse approach must be taken to find the phase function. Holographic methods, iterative phase retrieval,

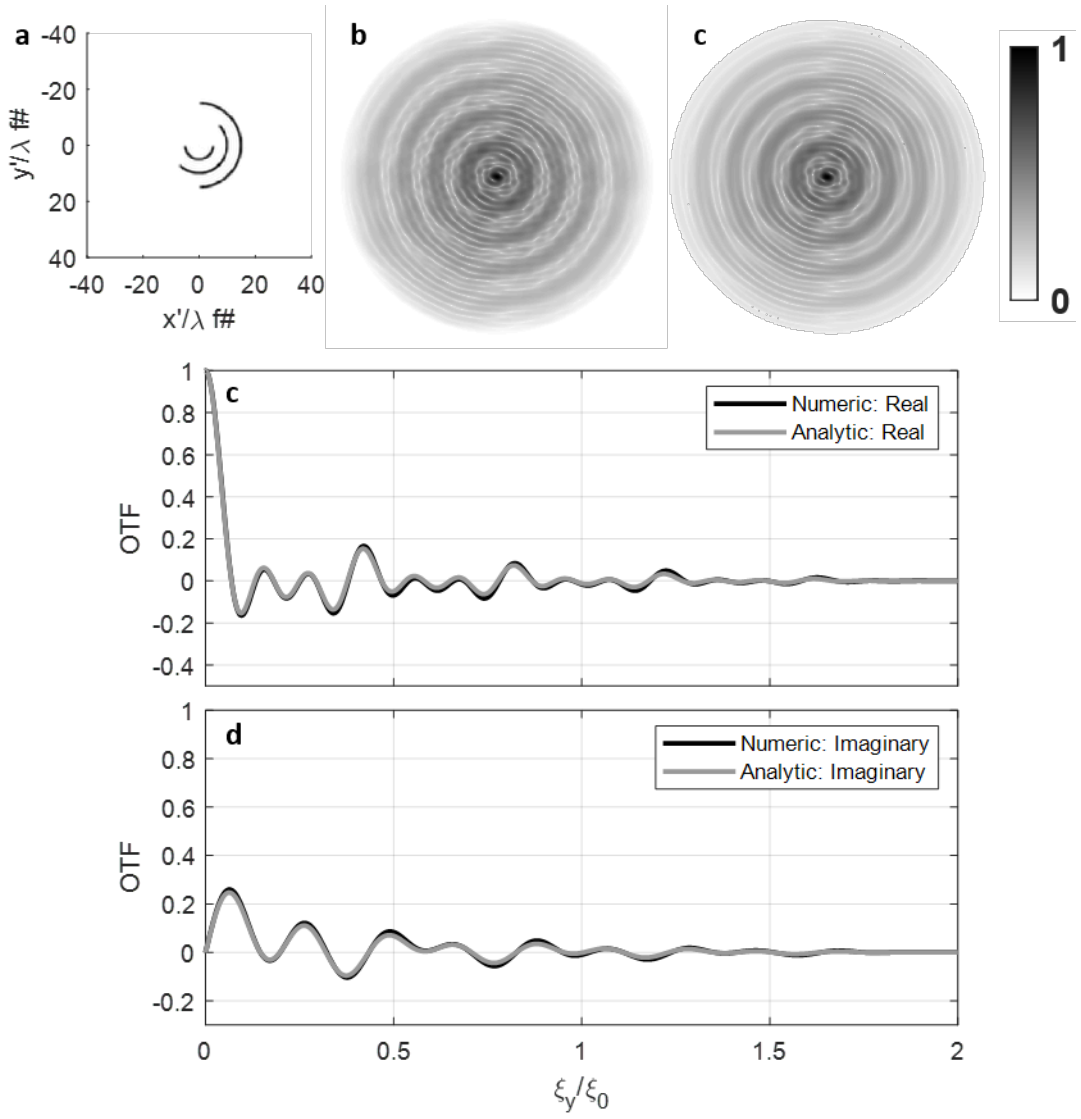


Figure 4.16: a) Numerically calculated multi ring PSF with radii 5, 10, and $15\lambda f\#$ and azimuthal offsets of 0, $\pi/4$, and $\pi/2$ radians. b) The numerically calculated MTF and c) analytically calculated MTF. numeric and analytic line profiles for $\xi_y$ axis of the OTF are shown in d and e.

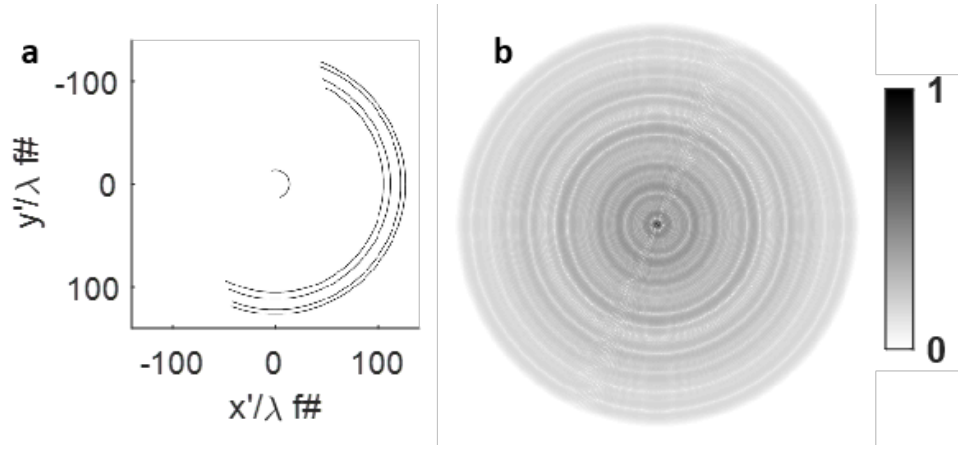


Figure 4.17: a) Five ring PSF optimized via a differential evolution algorithm and b) its accompanied MTF.

and scientific intuition were used to find the appropriate pupil phase.

The first attempt at designing a half ring point spread function was with a "half axicon" pupil phase. A semicircle pupil, with an axicon phase function produce a half ring-like PSF. Noting that for a coherent PSF $h(x', y')$ and pupil function $P(\xi_x, \xi_y)$

$$FT[P^*(-\xi_x, -\xi_y)] = h^*(x', y') \tag{4.26}$$

where $*$ denotes the complex conjugate. This equation shows a $180^o$ rotation of the pupil and taking the complex conjugate will result in the complex conjugate of the original PSF. For the half axicon, each half of the pupil would have oppositely sloped phases with the full pupil phase defined as

$$\Phi(x, y) = \begin{cases} 2\pi ar/R & x \geq 0 \\ -2\pi ar/R & x < 0 \end{cases} \tag{4.27}$$

where $R$ is the aperture radius and $a$ is a scalar coefficient which may be tuned to change the size of the PSF and adjust the LSR. Each half of the half axicon pupil results in the half ring structure which interferes with one another. The PSF of each pupil half and their combination is shown in Fig. 4.18 for $a = 20\pi$. An LSR of $10^{-3}$ may be achieved for

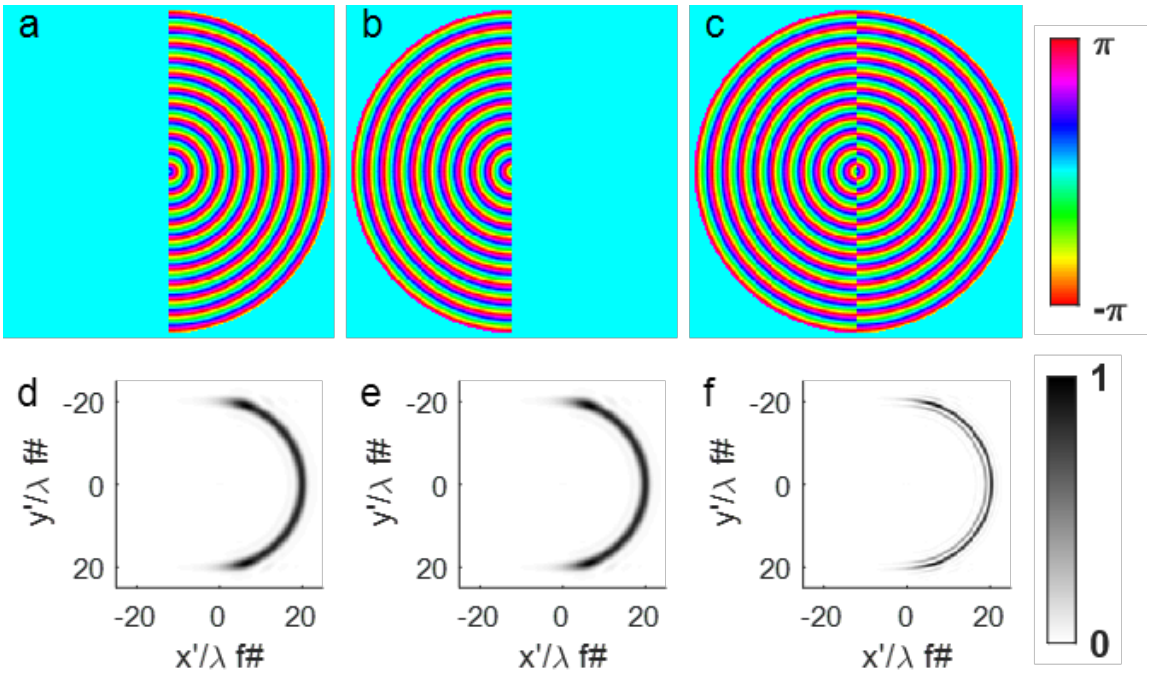


Figure 4.18: The half axicon pupil function which emulates the half ring PSF. a) semicircle pupil with axicon phase and $a = 20\pi$, b) complex conjugate and $180^o$ rotation of a, c) combination of a and b. d) PSF of a, e) PSF of b, and f) PSF of c.

$a = 208$ and results in $Strehl/LSR = 29.0$.

Another method for producing the phase is a method derived from holography in which the Fourier transform of the PSF is taken and the amplitude is disregarded with only the phase information used [86]. The Fourier transform was calculated for the OTF in Eq. 4.23

resulting in the pupil of

$$\Phi(\xi_r, \psi) = tan^{-1}\{\frac{\sum_j \sum_m \frac{4a_j}{(2m+1)\pi} sin[(2m+1)(\psi - \hat{\theta}_j)] J_{2m+1}(2\pi\xi_r a_j)}{\sum_j a_j J_0(2\pi\xi_r a_j)}\}. \tag{4.28}$$

The phase function, to be called the Bessel estimate, may be used to create an arbitrary multi half ring PSF with rings of different radii and azimuthal offset. The PSF differs from the desired PSF from Eq. 4.22 with additional ring in artifacts. These artifacts can be seen in Fig. 4.19 which shows the pupil phase and PSF for a single ring of radius $a = 20\lambda f\#$.

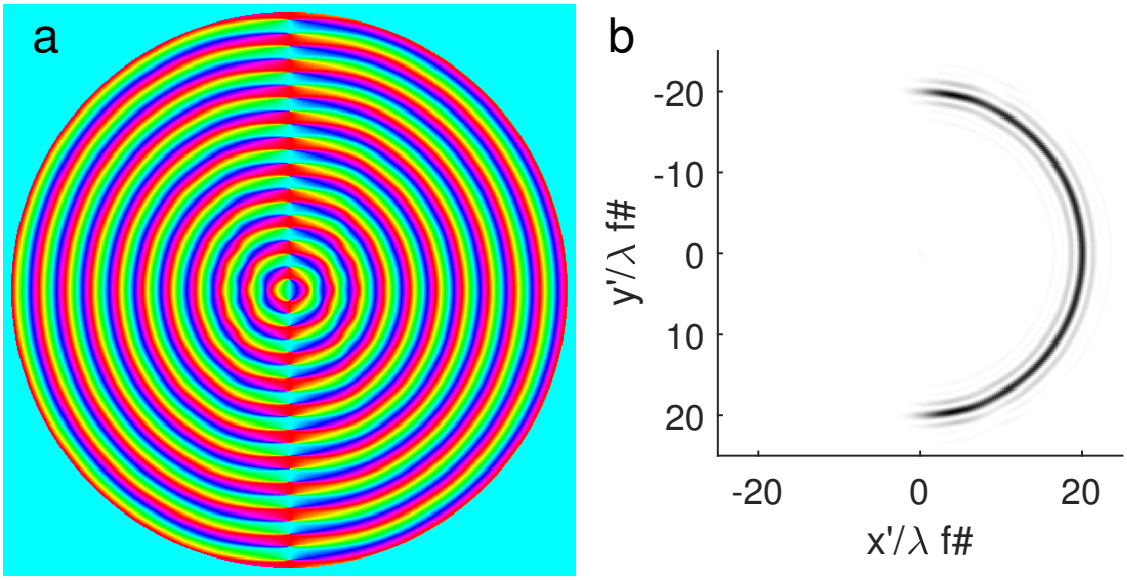


Figure 4.19: a) The pupil phase using Eq. 4.28 with $a = 20\lambda f\#$ and b) the accompanies PSF.

The value for Strehl as a function of LSR for the half ring PSFs is shown in Fig. 4.20. The Strehl ratio for the axicon, vortex, and cubic phase masks are shown for comparison. The Strehl for the half ring, half axicon, and Bessel estimate at an LSR of $10^{-3}$ are 0.0303, 0.0290, and 0.0323 respectively. These values suggest the Bessel estimate outperforms the

original half ring PSF. This may be due to limitations in calculating the Strehl for the half ring. As the pupil phase function is unknown, the PSF is calculated directly on a sampled computational grid where some thickness must be given to prevent jagged edges and ensure the PSF is evenly illuminated. Regardless if this would change the value of Strehl for the half ring, the performance of the Bessel estimate is a positive outcome as this PSF is realizable as the phase function is known. Each of the half ring PSF variants outperform the original axicon, vortex, and cubic phase masks.

### 4.3.3 Multi Half Ring Pupil Phase

For the five ring case, Eq. 4.28 may be used to estimate the pupil phase. The resulting phase function is shown in Fig. 4.21.

In general, the more rings added to the PSF, the more disparity there is between the Bessel estimate PSF and the desired PSF. A numeric Gerchberg-Saxton phase retrieval algorithm may be used to numerically correct the phase function [87,88]. The algorithm is shown graphically on Fig. 4.22. Starting with an input PSF, the inverse Fourier transform is taken, the intensity of this value is replaced with the desired amplitude – a circular pupil function. The Fourier transform is taken and the intensity is replaced with the desired PSF. The process is iterated until there is a converged solution.

Twenty iterations were taken with the output phase function shown in Fig. 4.21. Qualitatively, the phase mask designed through Eq. 4.22 and the phase mask designed through the Gerchberg-Saxton algorithm appear similar. It is not clear if there are definitive features which separate the two functions. Zoomed insets of the resulting PSFs and for the original five half ring PSF with no known phase function are shown in Fig. 4.23. Each of the PSFs have an $LSR$ of $10^{-3}$. In both estimates, there are additional artifacts that are

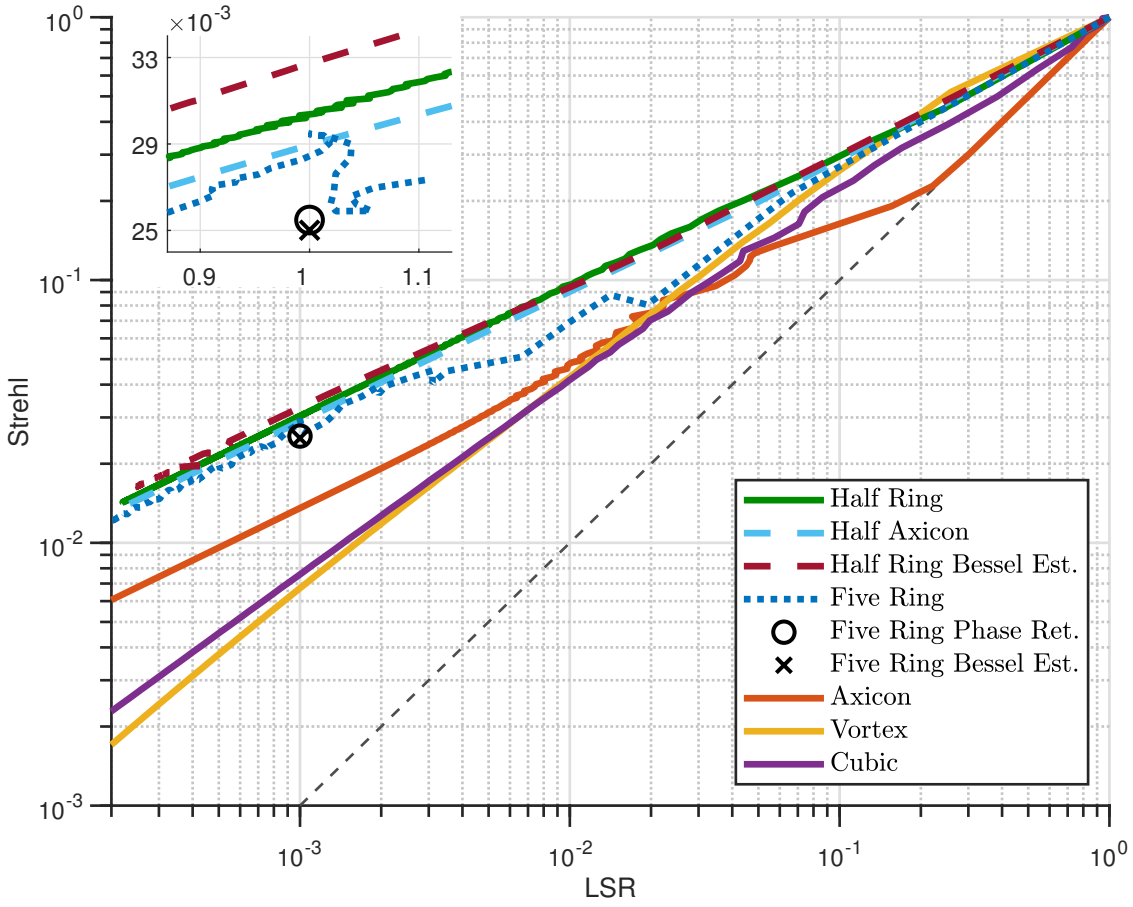


Figure 4.20: Plot of the integrated Strehl ratio as a function of LSR highlighting the half ring PSF variants. Each of the half ring PSFs greatly outperform the originally studied axicon, vortex, and cubic phase masks.

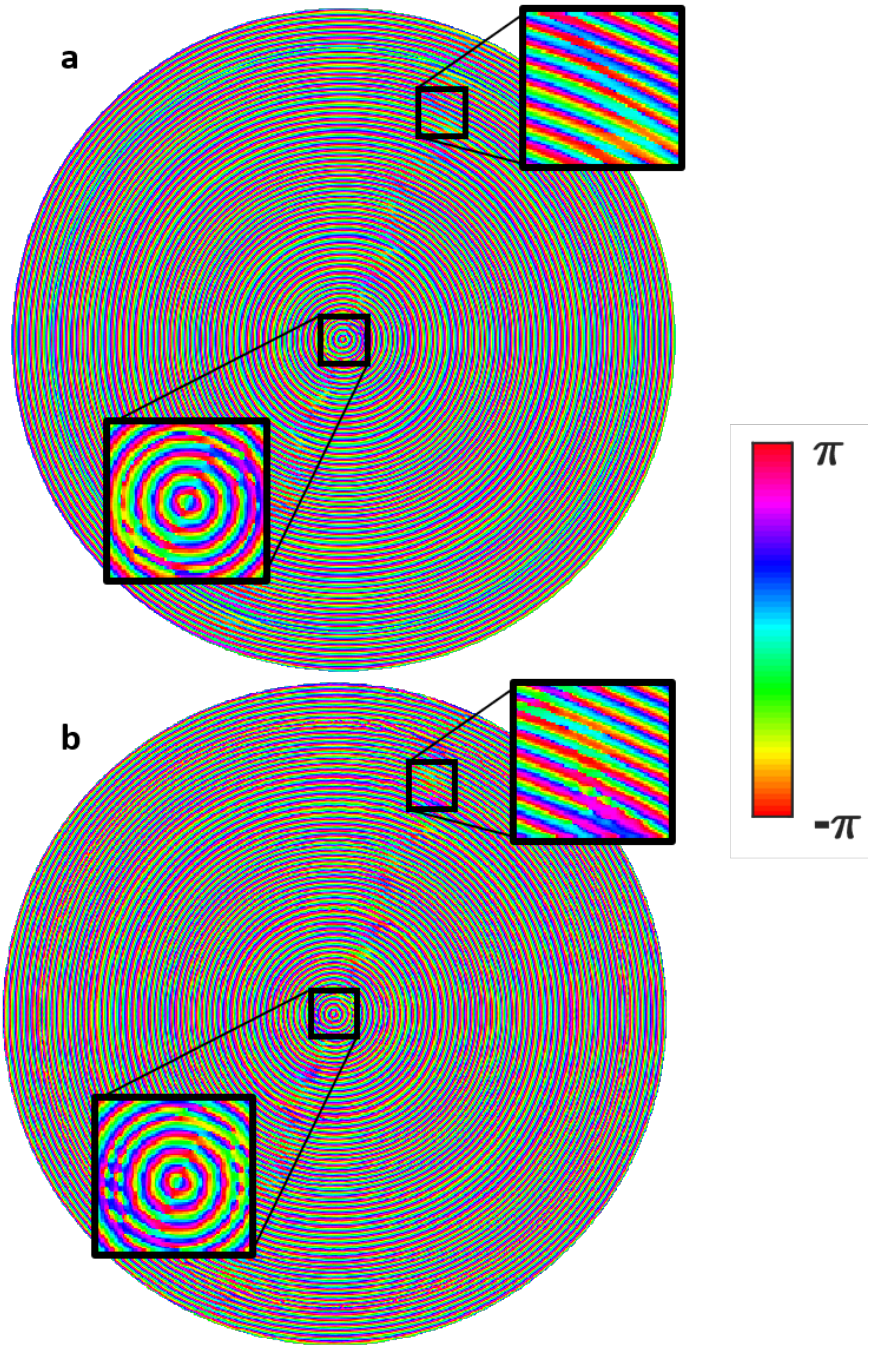


Figure 4.21: a) Five ring pupil phase estimate calculated with Eq. 4.28 and b) the five ring pupil phase estimated using a Gerchberg-Saxton phase retrieval algorithm.

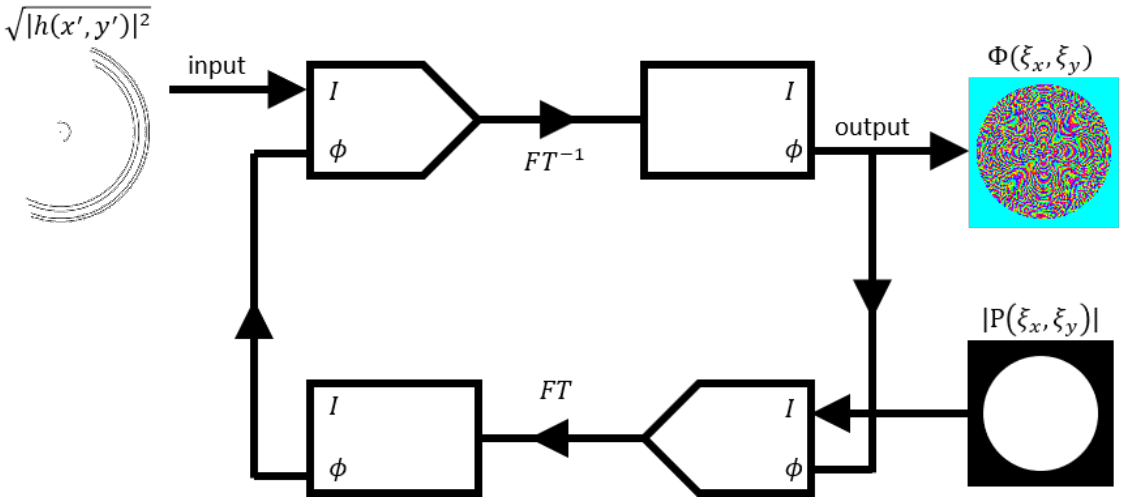


Figure 4.22: Graphical representation of the Gerchberg-Saxton phase retrieval algorithm. The coherent PSF, $\sqrt{|h(x',y')|^2}$, is the input. The pupil function, $P(\xi_x,\xi_y)$ is constrained to a circular pupil. 'the output is the desired phase function $\Phi(\xi_x,\xi_y)$.

not present in the original PSF. Comparing the two estimates, they both appear the same radially, but azimuthally the PSF resulting from the phase retrieved mask has a sharper edge.

The Strehl ratio for each of the five half ring PSF variants is shown in Fig. 4.20. The five half ring PSF has a curve generated by scaling the radii of the rings to adjust the size of the PSF. At an $LSR$ of $10^{-3}$, the value at which the five half ring PSF was optimized, the PSF has a Strehl ratio of 0.0295 – exceeding the half axicon. The Bessel estimate and phase retrieved PSF are represented by single points and have a Strehl of 0.0250 and 0.0255 respectively. The phase retrieval is shown to give a small improvement over the Bessel estimate.

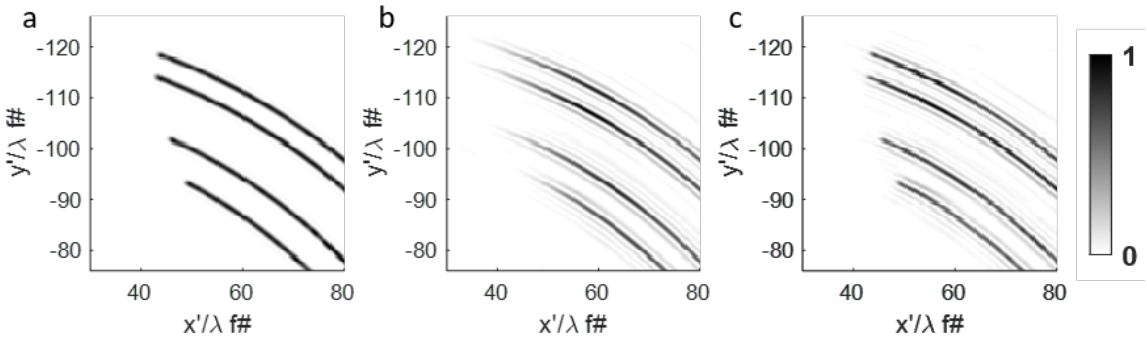


Figure 4.23: Zoomed region of the five ring PSF variants. a) PSF as designed by Eq. 4.22, b) PSF resulting from the pupil phase function in Eq. 4.28, c) PSF resulting from the Gerchberg-Saxton phase retrieval algorithm. Each PSF has a peak amplitude 3 orders of magnitude lower than the diffraction limited PSF.

### 4.3.4 Half Ring PSF Summary

A new family of half ring PSFs were designed keeping in mind the desired qualities of a PSF: having a large integrated odd component, having values close to to its peak intensity and zero otherwise, and containing narrow features. These PSFs were studied analytically resulting in the calculation of their OTFs. A five half ring psf was optimize through a differential evolution algorithm by altering the rings radii and azimuthal offsets. The pupil phases to produce the single or five half ring PSFs are unknown leading to a difficult inverse problem. Various estimates were found including a half axicon pupil phase, an estimate using a sum of Bessel functions, and a numeric solution calculated via an iterative phase retrieval algorithm.

Comparing the single and five half ring PSFs, the single half rings have a stronger Strehl ratio. Despite this, the half ring PSFs are less feasible to use due to their large spatial extent and would not fit on the sensor in the experimental setup. The five half ring has a maximum radius that is 3.6 times smaller than the single half ring case. As for selecting

between the two five ring estimates, there is an advantage in selecting the Bessel estimate as there is an analytic solution to the pupil phase function which may allow for more easily manufacturing the mask. This advantage is not present when using the SLM and so the phase retrieved mask will be used as it provides an improvement in Strehl Ratio.

## 4.4 Optimized PSF Summary

The previous sections illustrated incremental work in optimizing a phase mask for improved fidelity. A differential evolution algorithm optimized an azimuthal harmonic basis set. A hardware-based simulated annealing algorithm optimized a half Zernike basis set. Finally, a family of half ring PSFs were designed considering ideal characteristics of the desired PSF and the inverse problem was solved to find a pupil phase. A summary plot of these basis functions, the half ring PSFs, and the optimized results are shown in Fig 4.24. Also shown are the axicon, cubic, and vortex curves.

For values of LSR less than $10^{-2}$, the axicon, cubic, and vortex have the lowest Strehl. The single term azimuthal harmonic functions are the next lowest, then the half Zernike functions ($sign[x]Z_2^0$, and $sign[x]Z_2^0$), and the highest performing are the half ring PSFs. This shows steady improvement in integrated Strehl as the methods have progressed. The 5 term azimuthal harmonic, simulated annealing output, five ring, and five ring found via iterative phase retrieval are each represented by a single point. Each of these (except the five ring) represent the highest performing phase mask mask which may be tested experimentally for the value $LSR = 10^{-3}$. These each have a similar value for integrated Strehl.

There is an apparent power law for low values of LSR less than $10^{-2}$. As each PSF converges to the point Strehl = LSR = 1, the linear region of the plot may be represented

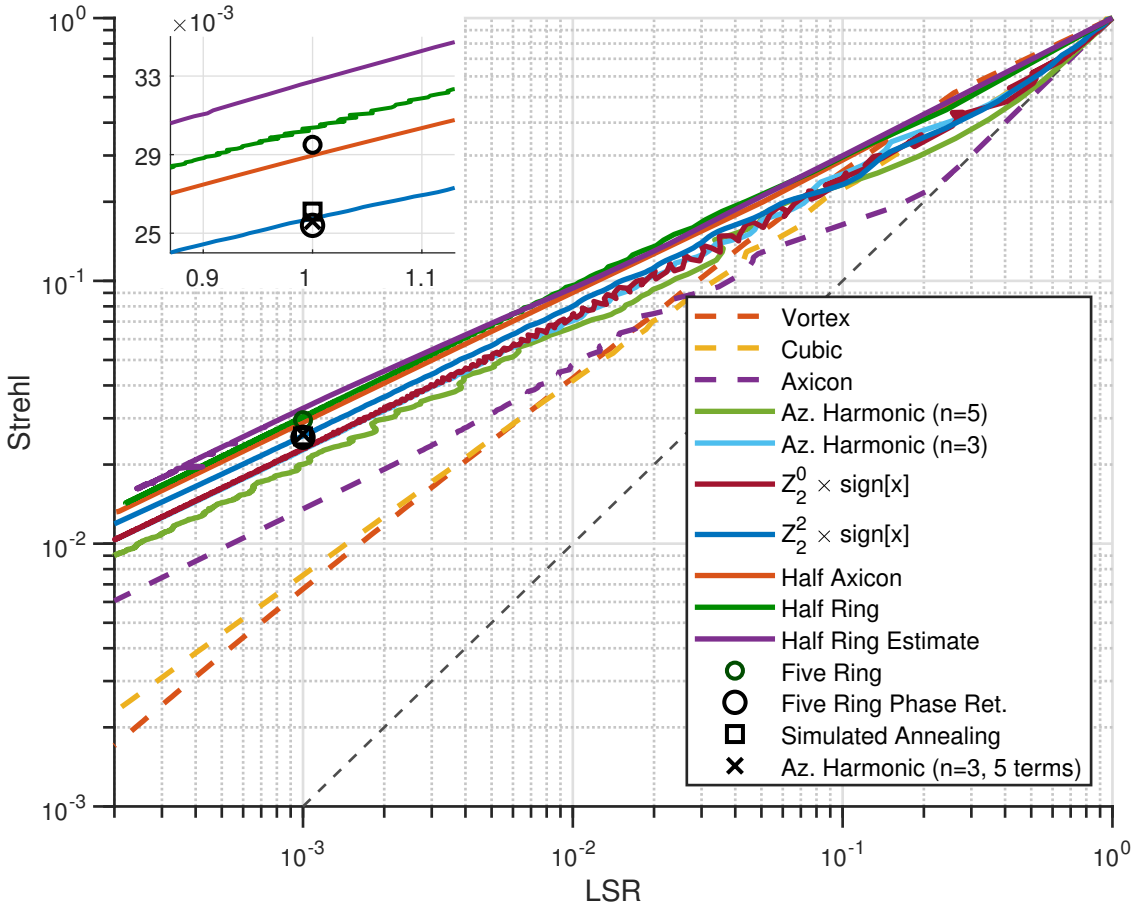


Figure 4.24: Strehl vs LSR plot summarizing the performance of each of the optimized PSFs. The inset shows the Strehl vs LSR on a linear scale. The black dashed line represents the minimum attainable value of Strehl.

by

$$Strehl = LSR^{\gamma} \tag{4.29}$$

where $\gamma$ represents the slope of the line on Fig. 4.24. The lower the value for $\gamma$ the higher the integrated Strehl with the highest value for $\gamma$ being 1 (Strehl = LSR) and the ideal, but unrealistic value of 0 (Strehl = 1).

Previously, the Strehl was given for the desired value of LSR to compare each of the phase functions. Using the power law gives a single value independent of the value of LSR allowing a more general method for comparing integrated Strehl. Each curve on Fig. 4.24 was fit to Eq. 4.29 using values of $LSR < 10^{-2}$. The value of $\gamma$ was directly calculated for the single point cases. The results are shown in Tab. 4.2.

| PSF | $\gamma$ |
|---|---|
| Half Ring Estimate (Eq. 4.28) | 0.496 |
| Half Ring | 0.506 |
| Five Ring* | 0.510 |
| Half Axicon | 0.514 |
| Simulated Annealing* | 0.528 |
| Half Zernike (2,2) | 0.531 |
| Azimuthal Harmonic (n=3, 5 terms)* | 0.531 |
| Five Ring Phase Retrieved* | 0.532 |
| Half Zernike (0,2) | 0.550 |
| Azimuthal Harmonic (n=3, 1 term) | 0.557 |
| Azimuthal Harmonic (n=5, 1 term) | 0.567 |
| Axicon | 0.636 |
| Cubic | 0.698 |
| Vortex | 0.719 |

Table 4.2: Values of $\gamma$ fit via Eq. 4.29 for phase masks and PSFs studied in this thesis. Asterisks represent values of $\gamma$ calculated from a single point.

## 4.5 Experimental Validation and Comparison

The previous sections yielded new optimized phase masks which, numerically, are shown to improve imaging fidelity over the axicon, vortex, and cubic phase masks. These new masks are the azimuthal harmonic, the simulated annealing result, and the five half ring. In this section, the masks will be tested experimentally with the results compared to both the numeric results as well as to each other.

Each of the pupil phases, PSFs, MTFs, and phase transfer functions are shown in Fig. 4.25. Each PSF has a value of $LSR$ of $10^{-3}$. The azimuthal harmonic pupil is the only phase function that is continuous as the simulated annealing result has a discontinuity along the vertical axis, and the five ring has singularities or vorticies in which the phase varies azimuthally around a point. This quality may make the azimuthal harmonic the easiest to potentially manufacture. The simulated annealing result contains nulls along the vertical axis of the MTF. There are also low frequency nulls in both the azimuthal harmonic and simulated annealing nulls which are noticeable by the singularities in their phase transfer functions. There do not appear to be any nulls in the five ring PSF by visual inspection. The five ring PSF has the largest spatial extent which may limit the field of view of the imaging system more than the azimuthal harmonic or simulated annealing.

The integrated Strehl ratio for the azimuthal harmonic, simulated annealing, and five ring PSFs are 0.0256, 0.0261, and 0.0255. While the simulated annealing PSF has the highest value of Strehl, it also contains the most nulls which will lead to significant noise gain. The azimuthal harmonic and five ring PSF have similar values of Strehl, but the lack of nulls in the five ring make it more beneficial.

Each of the masks are tested using the experimental setup shown in Fig. 3.1. The Holoeye GAEA SLM is used with 4160x2464 pixels and a 3.74 $\mu$m pitch. A 16 bit SBIG

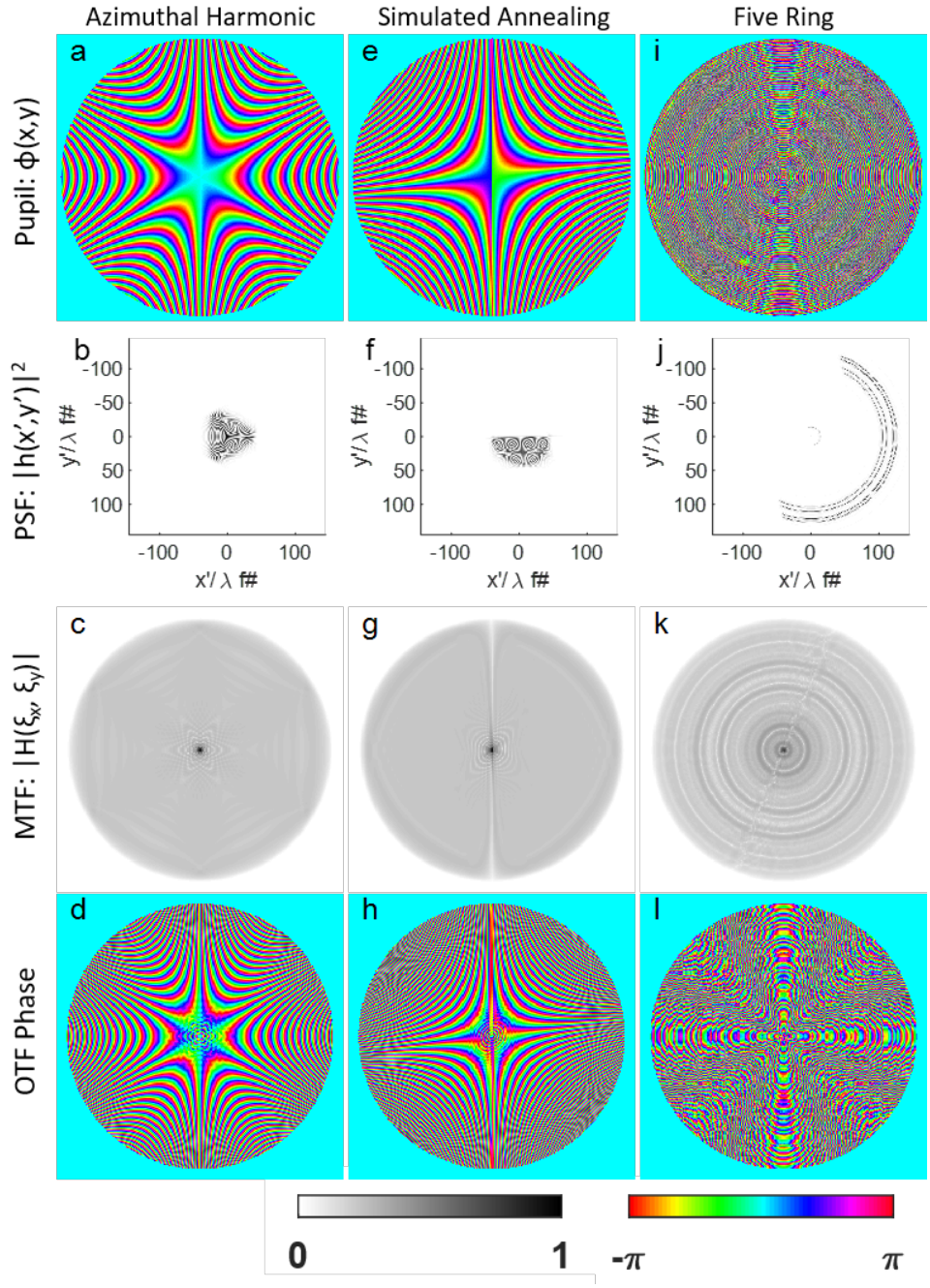


Figure 4.25: The pupil phase, PSF, MTF, and phase transfer function of a-d) the azimuthal harmonic PSF with $n = 3$ and 5 terms, e-h) the simulated annealing result, and i-l) the five half ring PSF optimized using the Gerchberg-Saxton phase retrieval algorithm.

STF-8300M CCD is used with 5.4 $\mu$m pitch. Two different diffuse targets were imaged: a clay tiger figurine and a resolution bar target. Both objects are shown in Fig. 4.26.

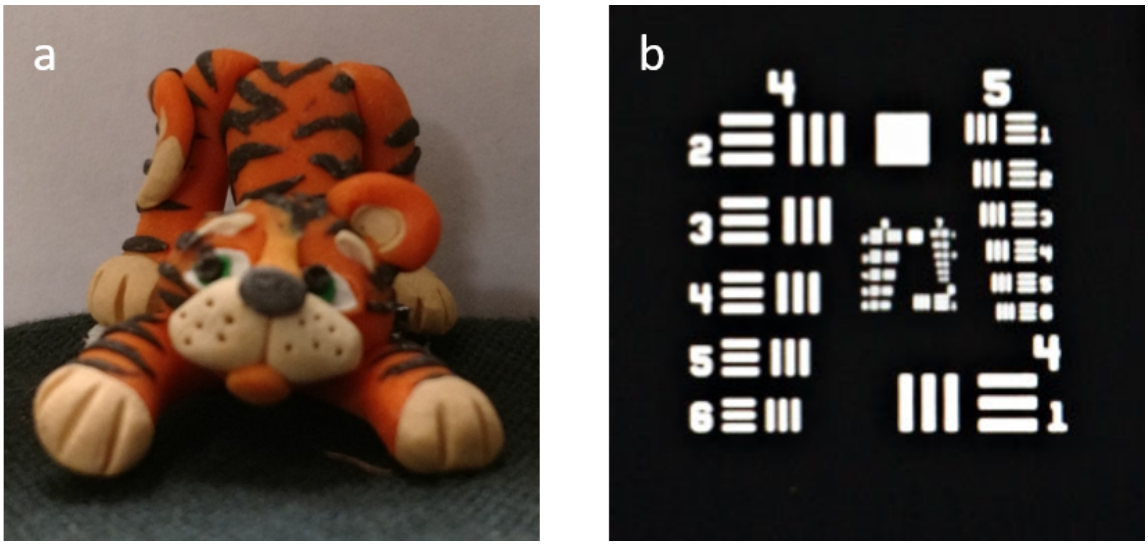


Figure 4.26: Objects imaged using the optimized phase masks: a) a clay tiger figurine and b) a transmissive resolution bar target.

Five images of the laser spot are recorded for each optimized phase mask on the SLM and for no phase. These are averaged and normalized to experimentally determine the PSF. Images are then taken of each object. Both are illuminated with a red LED attenuated by a narrow bandpass filter centered at 633 nm with a 10 nm full width half max to ensure quasi-monochromatic light. The bar target, a transmissive reticle, has a diffuser against it on the rear side. The resulting detected and restored images with the laser turned off are shown in Fig. 4.27 for the clay tiger and Fig. 4.28 for the bar target.

Each phase function was able to produce restored images of the tiger and bar target with varying degrees of success. From the tiger images, the azimuthal harmonic produced the worst fidelity images with heavy blurring and few high frequency features from the no phase image are discernible such as the knuckles or whiskers. The simulated annealing

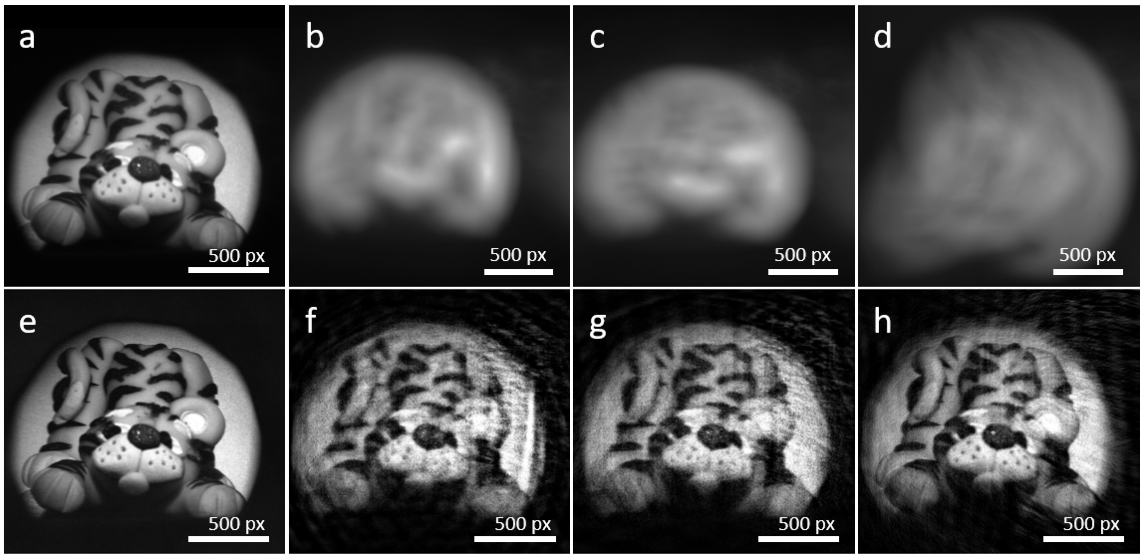


Figure 4.27: Detected images of the clay tiger with a) no phase, b) the azimuthal harmonic, c) the simulated annealing output, and d) the five ring function on the SLM. e-h) The restored images. Images b-c are shown on a log scale to display hard to see features. Scale bars show the length of 500 pixels on the sensor.

case is an improvement with sharper features and the tail becoming more noticeable. The five ring is the highest performing case which resulted in a sharp reconstruction. The images of the bar target give similar results with the azimuthal harmonic being the lowest performer. The simulated annealing result gives rise to significant artifacts which is the result of the low values in the vertical axis of the OTF. The five ring continues to be the higher performer with the bar target giving a near perfect restoration.

The detected image are each recorded with the same light levels and exposures (85 seconds for the tiger and 14 seconds for the bar target). Long exposures are due to low light levels, a low reflectance of the SLM, and poor diffractive efficiency at the desired diffractive order of the SLM. The exposure was set such that the no phase images have just saturated the sensor at their brightest points which for the tiger is the eyebrow and for

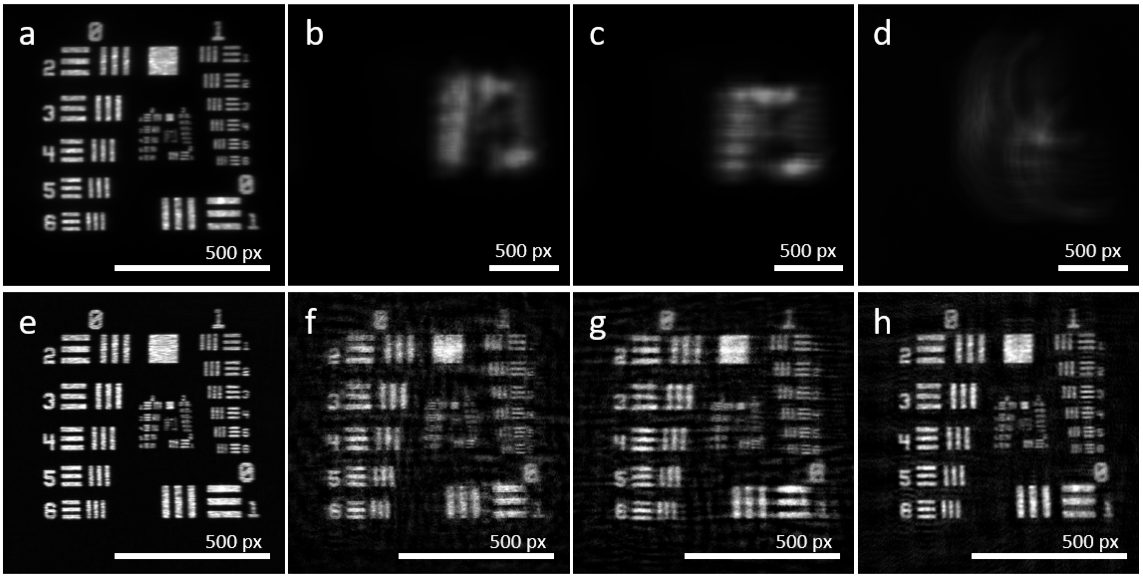


Figure 4.28: Detected images of the bar target with a) no phase, b) the azimuthal harmonic, c) the simulated annealing output, and d) the five ring function on the SLM. e-h) The restored images. Images b-c are shown on a log scale to display hard to see features. Scale bars show the length of 500 pixels on the sensor.

the bar tar the bottom right horizontal bars labeled “1”. Doing so achieves the maximum possible signal from each of the engineered masks as these images will use a fraction of the sensor’s dynamic range. For the tiger images, the azimuthal harmonic, simulated annealing and five ring cases have a peak signal 66.5%, 66.7%, and 47.8% of the saturation point. For the bar target these values are 23.4%, 27.6%, and 19.5%. If the full dynamic range of the sensor is used, the images could be improved and the final images have a dynamic range exceeding that of the sensor.

Average line profiles are taken of 3 sets of bars of the deconvolved images: the upper left horizontal bars, the adjacent vertical bars, and the solid square. The profiles are displays in Fig. 4.29 where the vertical axes are normalized where 0 and 1 represent the minimum and maximum counts of the sensor. Due to the chromatic aberration from the tilt of the SLM (even with the narrowband light), the horizontal bars are more resolved than the vertical. For the horizontal bars, despite the significant noise, the azimuthal harmonic mask produces sharp edges. Both the simulated annealing and five ring phase masks do a good job of producing the horizontal bars. For the vertical bars, the both the simulated annealing and azimuthal harmonic images produce a significantly reduced contrast. The reduction in performance from the simulated annealing result is expected from the low performing region of its OTF. The five ring case is once again the highest performing mask.

Quantitative metrics are extracted from the bar target image. Two measurements are sought: the relative edge response (RER) which is a measure of resolution and the noise gain (NG). As discussed in Se. 1.4, these metrics provide a good measurement of overall image quality. The RER is the normalized maximum edge slope of the new image calculated

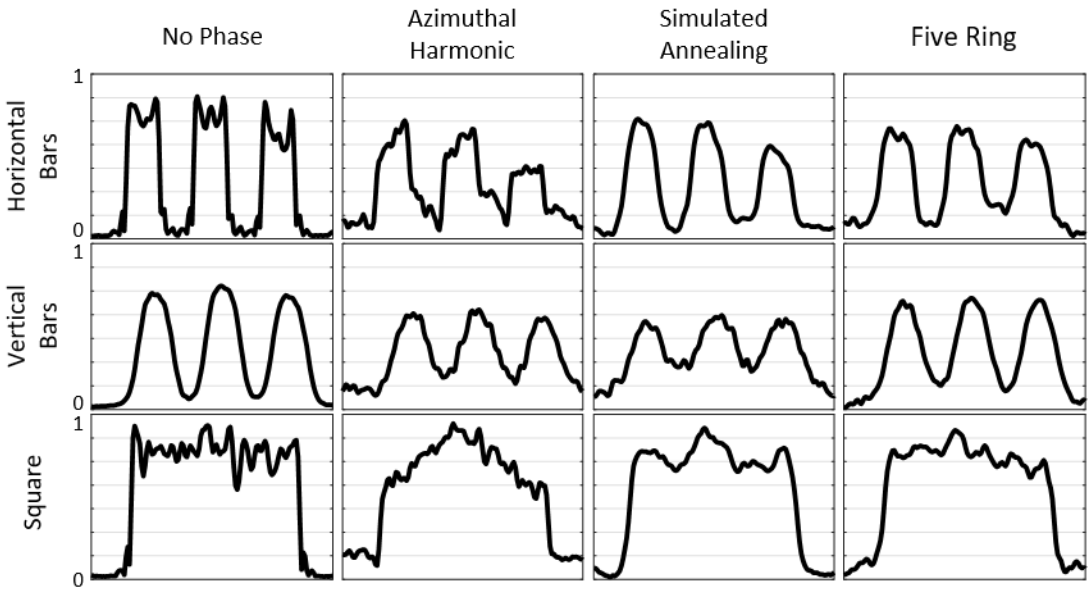


Figure 4.29: Average line profiles of the upper left horizontal bars, the adjacent vertical bars, and the solid square.

as

$$RER = \frac{max[dI/dr]}{max[dI_0/dr]} \tag{4.30}$$

where $I$ and $I_0$ are the pixel values of the deconvolved images with and without the phase mask at region of interest (the edge being measured), and $r$ is the direction perpendicular to the edge. The RER was calculated using the leading edge of the vertical bars shown in Fig. 4.29. This edge was used as opposed to the horizontal bars because the edge is blurred over a larger set of pixels allowing for a more accurate measurement which is less likely to be tampered by noise. The higher the value, the better with an ideal value of 1. The calculated values for the azimuthal harmonic, simulated annealing, and fiver ring images are 0.631, 0.604, and 0.926.

The NG is calculated as a normalized root mean square error of an expected uniformly

illuminated area of the image. A 140x140 pixel region inside the solid square at the top center of Fig. 4.28 (e-h). These areas are normalized such that the mean pixel count is 1. The NG is then calculated as

$$NG = \frac{\sqrt{\sum (I - \hat{I})^2 / N}}{\sqrt{\sum (I_0 - \hat{I}_0)^2 / N}} \tag{4.31}$$

where $\hat{I}$ and $\hat{I}_0$ are the mean values of the region for the phase mask, and no phase mask cases respectively. The lower the NG, the better with 1 being the ideal value. The resulting value for the azimuthal harmonic, simulated annealing, and fiver ring images are 4.09, 3.242, and 1.308. Both the RER and NG are visualized in the plot on Fig. 4.30. The five ring PSF is shown to have significant improvement in both edge response and noise gain over other optimized phase masks.

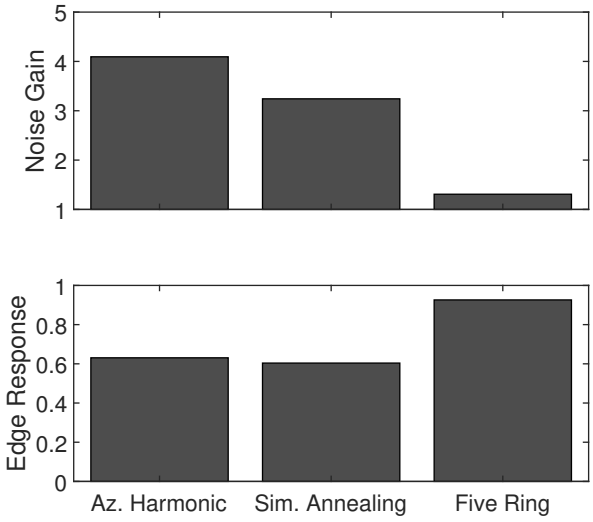


Figure 4.30: The noise gain (NG) and relative edge response (RER) for the azimuthal harmonic, simulated annealing, and five ring phase masks.

### 4.5.1 Images Saturated by Laser Source

Images were recorded of the tiger figurine with the laser present and are shown in Fig. 4.31 along with their deconvolutions. Due to the laser saturating the image, the deconvolved images have significant artifacts. A laser removal algorithm is implemented to replace the

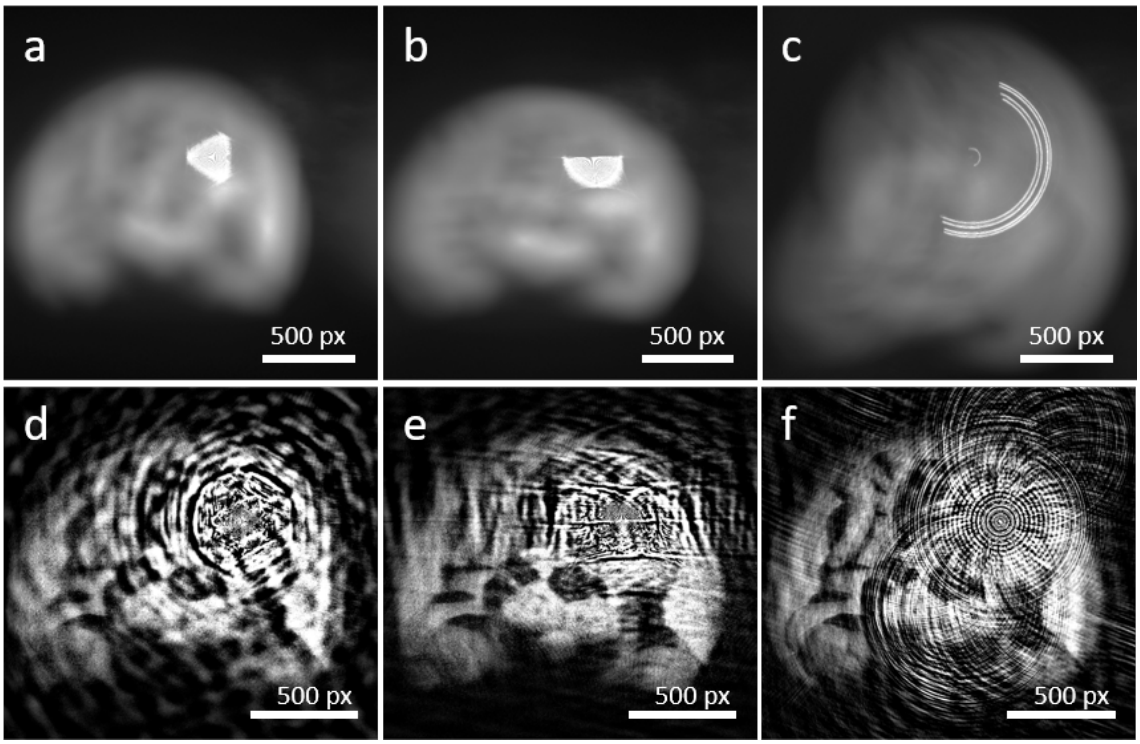


Figure 4.31: Detected images of the clay tiger with laser on for a) the azimuthal harmonic, b) the simulated annealing output, and c) the five ring function on the SLM. d-f) The restored images. The restored images contain artifacts due to the saturation from the laser source.

affected region with an estimate of the scene. First, the affected region is masked. The masked region is is replaced by minimizing the error of $\nabla^2 I(x', y') = 0$ using the perimeter of the masks as a fixed border constraint where $I(x', y')$ is the image. The new image is deconvolved to produce an image with fewer artifacts.

The process is shown for each detected image in Fig. 4.32. The mask extends beyond the saturated area as the laser still has intensity in these regions. The restored images show little difference from the detected images with no laser present. The algorithm benefits from the extended PSFs as the image will have no sharp features. The restored images are shown to have reduced artifacts.

Each mask results in a successful reconstruction of the image. Of note is that due to the small gaps in features from the azimuthal harmonic and simulated annealing cases, more of the image is lost to the laser subtraction than for the the half ring case.

The laser saturated images occur were recorded for relatively low laser power. The laser intensity was about 6 times the saturation point of the sensor for each image (would be 6000 times for the diffraction limited case). When the laser is more powerful, there are additional effects present including blooming, pixel cross-talk. In addition, speckle will become more intense than the desired signal. This speckle and other detector effect require additional processing would be required to reduce this effect.

## 4.6 Summary

In this chapter, three methods for solving the difficult task of optimizing pupil-phase functions were explored: a numeric-based differential evolution algorithm, a hardware-based simulated annealing algorithm, and a "PSF reverse engineering" method resulting in the half-ring PSFs.

The differential evolution algorithm is a genetic-like algorithm which randomly varies an initial population of phase functions to find a global optimal solution. Intermediate results optimizing to $LSR = 10^{-2}$ using an arbitrary set of basis functions. An azimuthal harmonic basis set was identified as a continuous basis set with relatively high values of

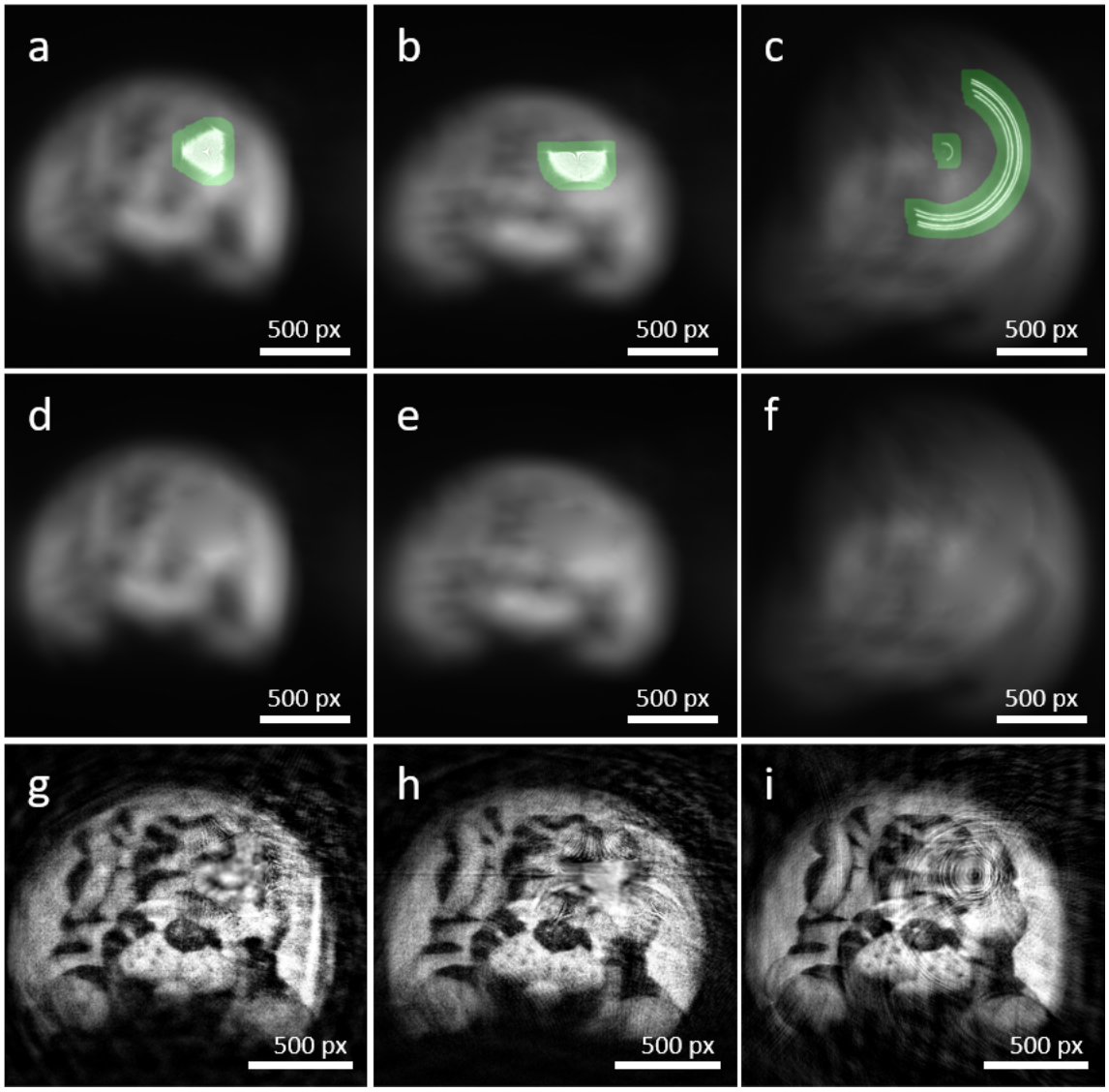


Figure 4.32: Detected images of the clay tiger with laser on with region to be removed asked for a) the azimuthal harmonic, b) the simulated annealing output, and c) the five ring function on the SLM. d-f) The images after the laser removal algorithm. g-i) The restored images. Artifacts are reduced from the laser removal algorithm.

Strehl ratio. This set was optimized for various numbers of terms using the differential evolution algorithm at $LSR = 10^{-3}$.

The simulated annealing algorithm was implemented for the hardware based optimization. The algorithm leveraged the electro-optically controlled SLM to create a hardware based feedback loop between the measurement of the PSF (CCD) and the pupil (SLM). The simulated annealing algorithm was used in lieu of the differential evolution algorithm to reduce the time required (from weeks to hours). A new input basis of "half-Zernike" functions were used which were even Zernike polynomial modified by the signum function to make them odd. Regardless, the algorithm resulted in a 13.8% improvement in the ratio of $Strehl/LSR$ from the input phase.

The third method, the PSF reverse engineering method, sought to design the PSF with ideal properties and solve the inverse problem of calculating the pupil function. The result was the half-ring PSFs which combined one or more semi-annuli. These PSFs were shown to greatly outperform those calculated through numeric means. The inverse problem was solved via holographic methods with the phase of the OTF as the phase mask of the aperture. A phase retrieval algorithm was implemented to further improve the accuracy of the phase function.

An azimuthal harmonic, output of the simulated annealing experiment, and the half ring PSF were each implemented in an experimental setup to image two diffuse targets. The half-ring PSF outperformed the other both the azimuthal harmonic and simulated annealing PSFs both qualitatively and quantitatively which shows the advantage of directly designing the PSF. In contrast, the half-ring pupil phase may provide a more challenging manufacturing task as the phase is more complex than the other two pupil phases.

Finally, each mask was used in experiment to image a target in the presence of satu-

rating laser radiation. The half ring continued to outperform the other as the saturated regions were more narrow and led to less information loss.

# Chapter 5

# Broadband Considerations

Previous sections looked at PSF engineered systems imaging either a monochromatic or quasi-monochromatic scene. In practice, the scene will be a continuous spectrum with little chance of knowing the spectral content before attempting to deconvolve the recorded image. This lack of knowledge makes it difficult properly model the PSF of the system and the image may no longer be spatially invariant. In this chapter the PSF as a function of wavelength will be discussed and how it affects image quality. Challenges with deconvolution and methods for mitigating them are also discussed. Finally a broadband imaging simulation is conducted using hyperspectral data sets. A seemingly naive processing method, assuming a uniform spectral content, is tested successfully in the simulation.

## 5.1 Broadband Imaging Theory

The Wiener filter was originally derived by minimizing the detected image and convolution between the estimated scene and the PSF in Eq. 1.9. This equation naively left out the spectral content which, for a panchromatic image, creates the under-constrained problem

of minimizing the equation

$$E = \int\int |S_e(\xi_x, \xi_y, \lambda) - [S_{tot}(\xi_x, \xi_y, \lambda)H(\xi_x, \xi_y, \lambda) + N(\xi_x, \xi_y)]|^2 d\xi_x d\xi_y. \tag{5.1}$$

To simplify the problem, an assumption can be made of the scene that the spectral content of the scene constant with and only changing in intensity. This assumption may be represented by the approximation:

$$I(x_0, y_0, \lambda) \approx \Lambda(\lambda) I(x_0, y_0) \tag{5.2}$$

where $I(x', y', \lambda)$, is the spectral radiance of the scene as a function of spatial coordinate, $I(x', y')$ is the scene radiance, and $\Lambda(\lambda)$ is the approximate spectral radiance of the entire scene [89]. If the function $\Lambda(\lambda)$ is known, Eq. 5.1 simplifies to the monochromatic case, though it is unlikely this function is known. In addition, the assumption maintains shift invariance in the detected image as each spot of the image would have the same PSF.

The accuracy of the approximation may not be good enough, especially if the scene being imaged is a combination of man made and natural objects. In addition, a PSF which varies greatly with wavelength would exaggerate any inaccuracies. In the following sections, previously studied PSFs are observed over a broadband range of wavelengths. A method for simulating panchromatic images using a hyperspectral data set is created and used to test the broadband performance of two pupil functions.

## 5.2 The Broadband PSF

Even if the imaging system had no dispersion and a lens had no chromatic focal length shift, the PSF would still vary as a function of wavelength. This is because the cutoff

frequency will still vary by $1/\lambda f\#$. The shorter the wavelength, the greater the cutoff frequency and the narrower the features of the PSF. In this section, the pupil function, PSF, and OTF will be studied as a function of wavelength. Doing so lays the groundwork for finding a PSF which is not greatly affected by a broadband scene and that allows for an improved deconvolution.

Previously, the pupil function was considered in terms of spatial coordinates. These coordinates may be represented instead in terms of spatial frequencies as

$$CTF(\xi_r, \psi, \lambda) = P(\xi_r \lambda f, \psi) = circ[\xi_r \frac{\lambda f}{R}] exp[i\Phi(\xi_r \lambda f, \psi)] \tag{5.3}$$

where $\xi_r$ is the radial spatial frequency coordinate, $f$ is the focal length, $\psi$ is the azimuthal angle, $\lambda$ is the wavelength, $R$ is the aperture radius, $\Phi(\xi_r \lambda f, \psi)$ is the phase function in spatial frequency coordinates, CTF is the coherent transfer function, and $circ(r)$ is the function

$$circ(r) = \begin{cases} 1 & r < 1 \\ & \\ 0 & r > 1 \end{cases}. \tag{5.4}$$

The coherent cutoff frequency can is found as $\xi_0 = 1/2\lambda f\#$, where $f\# = 1/2R$.

There are several methods for creating the phase mask. Here, a mask made from a single piece of etched glass is considered. The phase function is formed by altering the thickness, $d(r, \theta)$, of the mask such that

$$\Phi(r, \theta) = 2\pi \frac{n(\lambda) d(r, \theta)}{\lambda} \rightarrow d(r, \theta) = \Phi(r, \theta) \frac{\lambda}{2\pi n(\lambda)} \tag{5.5}$$

where $n(\lambda)$ is the index of refraction as a function of wavelength. Once made, the thickness of the glass is a fixed parameter. It will not vary as a function of wavelength. Lets consider

a mask designed for a central wavelength, $\lambda_c$, as

$$d(r,\theta) = \Phi_c(r,\theta)\frac{\lambda_c}{2\pi n(\lambda_c)}. \tag{5.6}$$

where $\Phi_c(r,\theta)$ is the desired phase function at the central wavelength. Then the phase as a function of wavelength is

$$\Phi(r,\theta) = \Phi_c(r,\theta)\frac{n(\lambda)}{n(\lambda_c)}\frac{\lambda_c}{\lambda} \tag{5.7}$$

The phase function may then be considered in spatial frequency coordinates as

$$\Phi(\xi_r\lambda f,\psi) = \Phi_c(\xi_r\lambda f,\psi)\frac{n(\lambda)}{n(\lambda_c)}\frac{\lambda_c}{\lambda} \tag{5.8}$$

Now consider the desired phase function at the central wavelength where the azimuthal and radial components are separable and the radial component is of a single power $l$ such that

$$\Phi_c(\xi_r\lambda f,\psi) = \Psi(\psi)(\frac{\xi_r\lambda f}{R})^l. \tag{5.9}$$

The phase function as a function of wavelength may then be simplified as

$$\begin{aligned}
\Phi(\xi_r\lambda f,\psi) &= \Phi_c(\xi_r\lambda f,\psi)\frac{n(\lambda)}{n(\lambda_c)}\frac{\lambda_c}{\lambda} \\
&= \Psi(\psi)(\frac{\xi_r\lambda f}{R})^l\frac{n(\lambda)}{n(\lambda_c)}\frac{\lambda_c}{\lambda} \\
&= \Psi(\psi)(\frac{\xi_r\lambda_c f}{R})^l\frac{n(\lambda)}{n(\lambda_c)}\frac{\lambda^{l-1}}{\lambda_c^{l-1}} \\
&= \Phi_c(\xi_r\lambda_c f,\psi)\frac{n(\lambda)}{n(\lambda_c)}\frac{\lambda^{l-1}}{\lambda_c^{l-1}}.
\end{aligned} \tag{5.10}$$

While several phase functions studied do not fit the assumption of a radial component

of a single order, many still do including the half axicon, and the single term azimuthal harmonic. The solution is also easy to compute for a computer program as $\Phi_c(\xi_r \lambda_c f, \psi)$ is constant. The final CTF function is then

$$CTF(\xi_r, \psi, \lambda) = circ[\xi_r \frac{\lambda f}{R}] exp[i\Phi_c(\xi_r \lambda_c f, \psi) \frac{n(\lambda)}{n(\lambda_c)} \frac{\lambda^{l-1}}{\lambda_c^{l-1}}]. \tag{5.11}$$

While the spectral content of the scene is unknown, a broadband point response function is calculated as

$$|\tilde{h}(x', y')|^2 = \int_{\lambda_a}^{\lambda_b} |h(x', y', \lambda)|^2 d\lambda \tag{5.12}$$

where $\lambda_a$ and $\lambda_b$ are a minimum and maximum wavelengths the response is to be observed. The function, which will be referred to as the broadband PSF, serves to show the response given a uniform spectral content. The Fourier transform of the broadband PSF gives a broadband transfer function.

The pupil, PSF, MTF, and broadband PSF and MTF are calculated in simulation for the half axicon and azimuthal harmonic phase functions. For these calculations, a wavelength range from 0.4 $\mu m$ - 0.7 $\mu m$ and a value of $f/2R = 5$ are used. No dispersion is added such that $n(\lambda_c)/n(\lambda) = 1$. The phase at the central wavelength for the azimuthal harmonic is

$$\Phi_c(\xi_r \lambda_c f, \psi) = 2 \times 2\pi \xi_r^2 (\frac{\lambda_c f}{R})^2 cos(5\psi) \tag{5.13}$$

and for the half axicon is

$$\Phi_c(\xi_r \lambda_c f, \psi) = 10 \times 2\pi \xi_r (\frac{\lambda_c f}{R}) \times sign(x). \tag{5.14}$$

The pupil, PSF, MTF, and broadband functions for the azimuthal harmonic is shown in

Fig. 5.1 and the half axicon in Fig. 5.2.

For the azimuthal harmonic PSF, the spatial extent of the PSF remains the same for each wavelength. The points within the star shape become larger with the wavelength with fewer of them present. A similar trend is present with the half axicon phase function the radii remaining constant, but the rings get thicker as a function of wavelength. For the broadband azimuthal harmonic PSF, the nodes from the individual wavelengths are blurred into lines. The broadband MTF has a different structure than any of the single wavelength MTF's with several spokes from the center. For the half axicon, the broadband PSF still resembles the same shape as individual wavelength PSFs. The same is true with the broadband MTF. The consistency of the half axicon PSF should lead to a better broadband deconvolution.

The effect of dispersion on the broadband performance has not yet been considered. Generally, dispersion is considered to be detrimental to an imaging system leading to chromatic aberrations, but may be used to correct issues with the azimuthal harmonic phase function. Consider a dispersion defined by $n(\lambda)/n(\lambda_c) = \lambda_c/\lambda$. The added dispersion alters the PSF shown in Fig. 5.1 resulting in the PSFs shown in Fig. 5.3.

At the selected wavelengths shown, the individual nodes of the PSF are aligned with one another at the cost of the spatial extent of the PSF decreasing as a function of wavelength. These nodes are distinct in the integrated PSF which results in a broadband MTF which is more consistent with those of the individual wavelength. Using the selected dispersion correction, $\Phi(\xi_r \lambda f, \psi) = \Phi(\xi_r \lambda_c f, \psi)$. This matches the same relationship as the half axicon pupil phase which may show an important trait of a well performing broadband PSF. For the azimuthal harmonic PSF, because of the change in the spatial extent as a function of wavelength, there will be some negative affect on the MTF. In addition, the dispersion

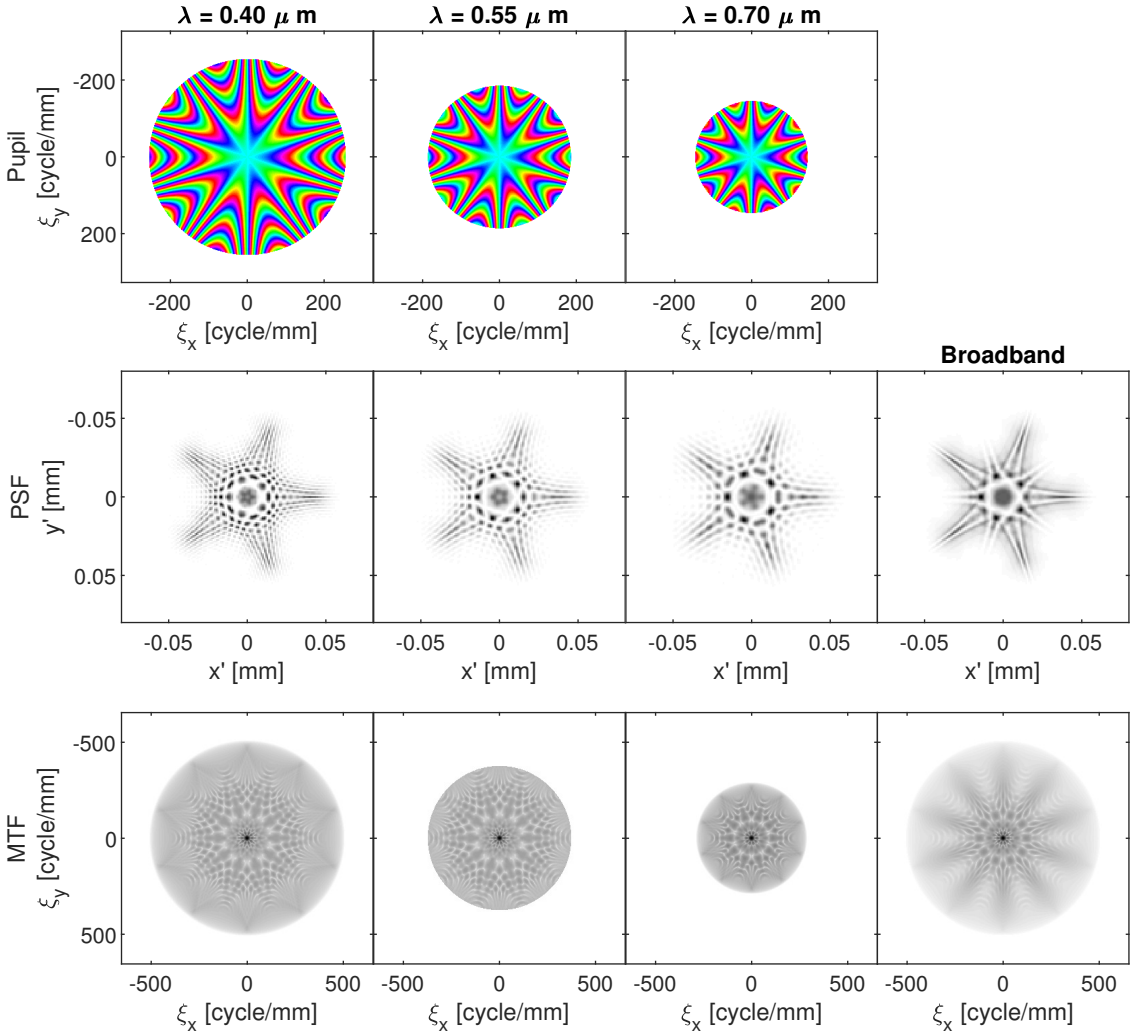


Figure 5.1: The pupil, PSF, and MTF at wavelengths 0.4 $\mu m$, 0.55 $\mu m$, and 0.7 $\mu m$ and the broadband integrated PSF and MTF for the azimuthal harmonic phase function.

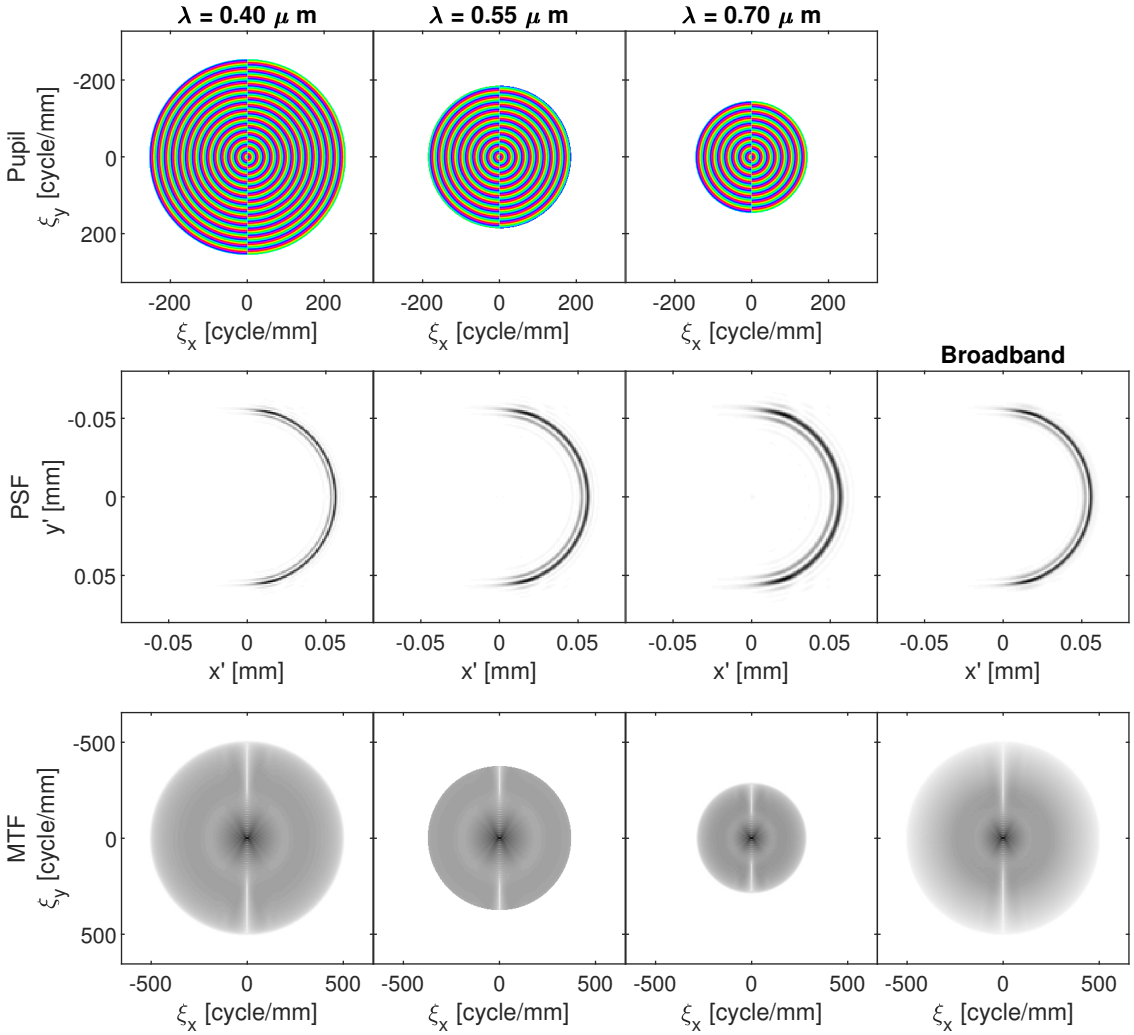


Figure 5.2: The pupil, PSF, and MTF at wavelengths 0.4 $\mu m$, 0.55 $\mu m$, and 0.7 $\mu m$ and the broadband integrated PSF and MTF for the half axicon phase function.

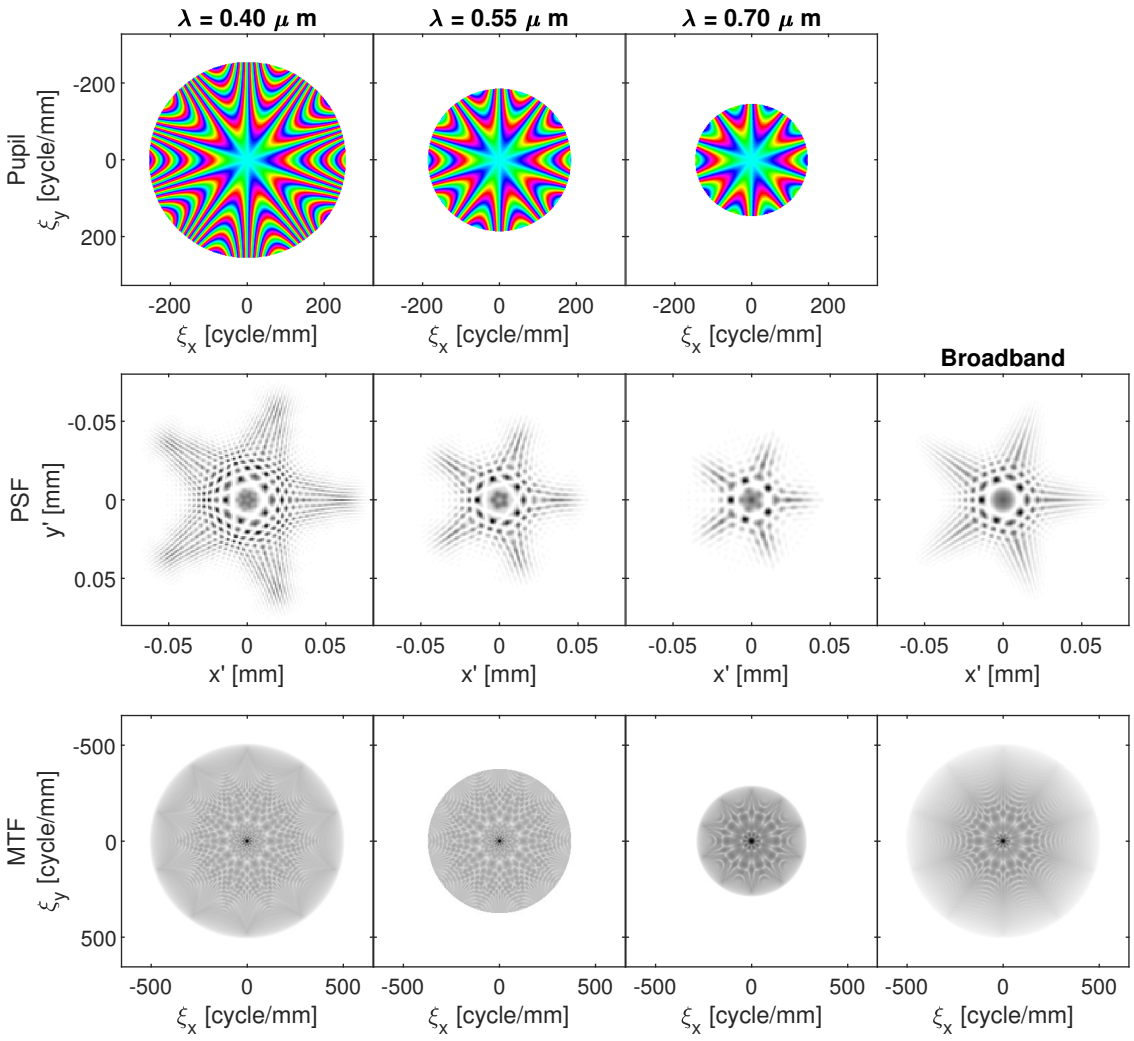


Figure 5.3: The pupil, PSF, and MTF at wavelengths 0.4 $\mu m$, 0.55 $\mu m$, and 0.7 $\mu m$ and the broadband integrated PSF and MTF for the azimuthal harmonic phase function with added corrective dispersion function.

curve is most likely not feasible with the assumption of a single dielectric material. The glass LASF35 produces a significantly lower dispersion ($0.06 \times \lambda_c/\lambda$) [90].

In total, the half axicon was shown to have consistency in the PSF over the visible wavelengths. The azimuthal harmonic PSF has feature with narrow spacing between them. As the wavelength shifts, these feature change size and translate so that when integrating over the visible spectrum, they blur together. Not only does this blurring greatly reduce the amplitude of the OTF, it changes the structure of the OTF which would prevent image reconstruction. The broadband phase function of the half axicon, $\Phi(\xi_r \lambda f, \psi) = \Phi(\xi_r \lambda_c f, \psi)$, was shown to be potentially desirable as it leads to these described traits. This was shown by altering the dispersion for the azimuthal harmonic function to produce the same broadband phase function. Though the features are no longer blurred together, the dispersion may not be possible and the spatial extent of the PSF varied greatly as a function of wavelength.

## 5.3 Broadband Imaging Simulation

To test broadband deconvolution, a panchromatic image is simulated using a hyperspectral data set. The simulation is shown graphically in Fig. 5.5. A data set containing 183 bands in the visible spectrum from 400 - 700 nm. The PSF at each band is calculated assuming a dispersion free glass with a central wavelength phase function defined by Eq. 5.14 and Eq. 5.13 for the half axicon and azimuthal harmonic PSFs. The bands are then summed to form a single panchromatic image. This image is quantized to 16-bits. While noise and turbulence models can also be added, the goal is to test the validity of deconvolving the scene with an estimated broadband PSF.

Detected images with the half axicon and azimuthal harmonic PSF are shown in

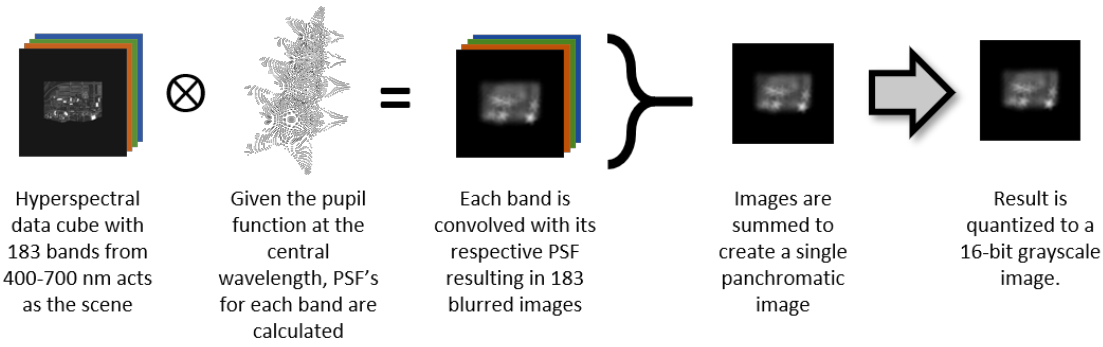


Figure 5.4: Process for simulating panchromatic images using a hyperspectral data set.

Fig. 5.5a and 5.5b. The simulate image with no phase mask is shown in Fig. 5.5c. No noise or turbulence models are added to the images, meaning these images have the equivalent to an infinite SNR. Any artifacts in reconstructing the images would then be due to a disparity between the estimated broadband OTF and the actual OTF of the system. A broadband PSF is created by assuming a uniform spectral radiance and integrating over the bandwidth 400 - 700 nm – the same broadband PSFs from Fig. 5.1 and 5.2. The blurred detected images are deconvolved with the broadband PSFs and are shown in Fig. 5.5d and 5.5e. Zoomed regions of the no phase and deconvolved images are shown in Fig. 5.5f-5.5k.

The azimuthal harmonic restoration is shown to have significant artifacts. While there is some blurring, the half axicon restoration are near perfect reconstructions. These results validate the expectations from the observations of the broadband PSF. These results also show a properly chosen PSF will be able to reconstruct images with similar performance to the monochromatic case.

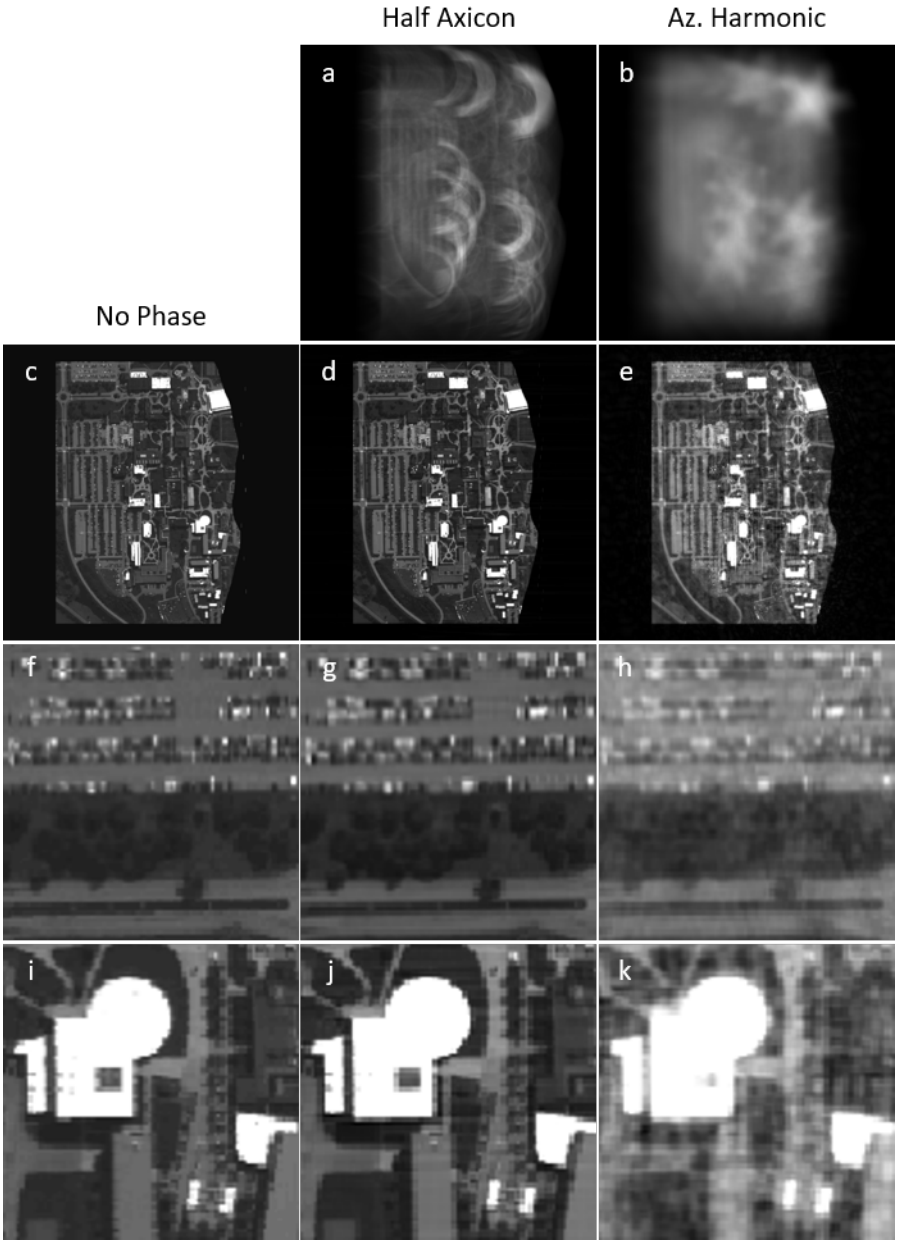


Figure 5.5: Simulated panchromatic images with a) a half axicon and b) azimuthal harmonic phase functions. c) Simulated panchromatic image with no phase function. d-e) Deconvolutions of a and b using a broadband PSF. f-k) Zoomed insets of c-e.

## 5.4 Summary

PSF engineering in the presence of a broadband scene was addressed. Regardless of chromatic aberrations or dispersion, the PSF should be expected to change as a function of wavelength due to the shifting spatial cutoff frequency. Assumptions allowing broadband scenes to maintain shift invariance were made and their limitations identified. A simplified pupil phase as a function wavelength was calculated for function where the azimuthal and radial portion are separable and the radial portion is of a single power. Examples of broadband PSFs were shown for the half-axicon (function of $r$) and the single term azimuthal harmonic (function of $r^2$) pupil phase were shown. Dispersion-free elements were assumed. The half axicon, which contains a single semi-annulus, was shown to maintain its structure. The azimuthal harmonic, which contains many features separated by narrow gaps, was blurred and lost most of its structure.

A simulation was developed using a hyperspectral data set as the scene. Each band was convolved with its respective PSF and summed to create a panchromatic image of the scene. Images were simulated for both the half-axicon and azimuthal harmonic phase function. A naive deconvolution was made assuming the scene has a uniform spectral radiance with varying magnitudes. The half-axicon provided a successful restoration of the scene with the azimuthal harmonic resulting in heavy noise and artifacts.

The work done in this chapter provides limitations on the broadband performance of the engineered PSFs. Narrow gaps in features have the potential to blur together, leading to drastic changes in the PSF and MTF. If using a half ring PSF with multiple annuli, there may be a requirement for a minimum separation between subsequent rings to prevent this.

Experimental images for a broadband scene are not possible using the SLM which is

highly diffractive and dispersive. This is a limitation of the experiment as it currently stands, not of the technique. Future work using should include testing broadband performance of thin diffractive masks manufactured for a compact imaging system. Such systems would include additional chromatic aberrations that should be compensated for in post-processing.

# Chapter 6

# Conclusion and Future Directions

## 6.1 Conclusion

This thesis has presented a novel computational imaging approach to sensor protection using point spread function engineering to redistribute laser light on the sensor effectively reducing its peak irradiance. The proposed system utilizes a linear phase element in the pupil of a traditional imaging system capable of modifying the wavefront of transmitted light instantaneously, over a large spectral bandwidth, and with a high damage threshold. As the mask can not discriminate light between harmful laser radiation and the desired scene, a post-processing step is required to remove saturated regions and to restore a sharp image. This method can reduce the peak irradiance by at least three orders of magnitude and has the additional benefit of being able to be combined with other laser suppression methods such as nonlinear optical limiters.

PSF engineering systems were studied in terms of an integrated Strehl ratio, a metric for evaluating image quality. Fundamental limits for the values of Strehl relative to the level of sensor protection were found. Performance of phase masks were also explored

relative to their even and odd symmetry with an odd symmetry found to be advantageous. A joint deconvolution method combining exposures of the same scene through different phase masks was also developed to reduce the effects of nulls in the transfer function and prevent excessive noise gain.

An experimental setup was designed to test the PSF engineered imaging system using a spatial light modulator as a digitally-controlled arbitrary phase mask. The spatial light modulator, a reflective and diffractive surface, provided challenges which would not be present with a static transparent phase mask. Methods for overcoming these challenges met and limitations on field of view and spectral bandwidth of the scene were made. Previously know axicon, cubic, and vortex phase functions were tested to image a resolution bar target in the presence of a laser to both validate the proposed imaging system and test if the odd cubic function outperforms the even axicon and vortex functions. Each mask successfully restored an image of the target while reducing the peak irradiance of the laser by a factor of 50. The cubic provided both high resolution and less noisy restored image. The joint deconvolution method was also validated by combining exposures using the vortex and axicon phase mask to greatly reduce the noise gain.

Numeric and analytic approaches were taken to optimize the phase function of the pupil element to provide even greater laser suppression without sacrificing fidelity of restored images. Three approaches were taken: (1) a numeric differential evolution algorithm, (2) a hardware based simulated annealing experiment, and (3) a PSF reverse engineering method. Three optimized phase masks stood out from these methods including an azimuthal harmonic, a simulated annealing output consisting of a weighted average of half Zernike polynomials, and a half ring PSF consisting of one or more concentric semi-annuli. These were each tested using the experimental setup to provide three orders of magnitude

suppression with the half ring PSF shown to provide substantially higher fidelity images. An algorithm for replacing regions of the image affected by the laser with estimates of the scene was shown to improve image restoration.

Finally broadband considerations were made for engineered PSFs. A half axicon and a azimuthal harmonic phase mask were tested to show their respective PSF as a function of wavelength with the assumption that the phase mask was made of a dielectric material of uniform index of refraction and varied thickness. The half axicon was shown to be more resilient to change with shifting wavelength suggesting higher broadband imaging performance. A potential correction of the azimuthal harmonic leveraging dispersion was found. The higher broadband imaging performance was validated in simulation for the half axicon.

## 6.2 Future Directions

The PSF engineered system was validated in a controlled laboratory setup. To further this technology, a compact system utilizing a thin transparent phase mask should be designed and tested. Masks made from lithographic techniques and from photo-aligned liquid crystals show promise. These materials should be tested for the broadband imaging case, as the spatial light modulator was limited to quasi-monochromatic illumination.

Effects of imaging in a true environment should also be tested. Effects of turbulence, motion blur, and vibration should be taken into consideration with potential to provide new image restorations algorithms to improve performance under these conditions. The added information gathered using a Bayer mask can also be taken into consideration. Optimization of phase masks may also include considerations on the complexity of the mask and manufacturing limitations.

# Appendix A

# Fourier Transform of a Circularly Symmetric Function

Consider a circularly symmetric function of the form

$$f(r,\theta) = \sum_{l=-\infty}^{\infty} f_l(r) e^{il\theta}. \tag{A.1}$$

The Fourier transform of the function may be calculated as a series of Hankel transforms. Let $\xi_r$ be the radial spatial frequency coordinate such that $\xi_r = \sqrt{\xi_x^2 + \xi_y^2}$ and let $\psi$ be the azimuthal direction such that $\psi = arctan[\xi_y/\xi_x]$.

$$\begin{aligned} FT[f(r,\theta)] &= \int_{-\infty}^{\infty}\int_{-\infty}^{\infty} f(r,\theta) exp[2\pi i(x\xi_x + y\xi_y)] dxdy & \text{(A.2)} \\ &= \int_{0}^{\infty}\int_{-\pi}^{\pi} f(r,\theta) exp[2\pi i \xi_r r cos(\theta - \psi)] r dr d\theta & \text{(A.3)} \\ &= \sum_l \int_{0}^{\infty}\int_{-\pi}^{\pi} f_l(r) exp(il\theta) exp[2\pi i \xi_r r cos(\theta - \psi)] r dr d\theta & \text{(A.4)} \end{aligned}$$

letting $\phi = \theta - \psi$ results in

$$= \sum_l exp(il\psi) \int_0^\infty \int_0^{2\pi} f_l(r) exp(il\phi) exp[2\pi i \xi_r r cos(\phi)] r dr d\phi. \tag{A.5}$$

Bessel's integral [91, Eq. 10.9.2] may be altered to simplify A.5

$$\begin{aligned}
\pi i^l J_l(z) &= \int_0^\pi exp[izcos(\theta)] cos(l\theta) d\theta \\
&= \frac{1}{2} \int_0^\pi exp[izcos(\theta)][exp(il\theta) + exp(-il\theta)] d\theta \\
&= \frac{1}{2}[\int_0^\pi exp[izcos(\theta)] exp(il\theta) d\theta + \int_0^\pi exp[izcos(\theta)] exp(-il\theta) d\theta] \\
&= \frac{1}{2}[\int_0^\pi exp[izcos(\theta)] exp(il\theta) d\theta + \int_{-\pi}^0 exp[izcos(\theta)] exp(il\theta) d\theta] \\
&= \frac{1}{2}[\int_{-\pi}^\pi exp[izcos(\theta)] exp(il\theta) d\theta \\
&= \frac{1}{2}[\int_{-\pi}^\pi exp[izcos(\theta)] exp(il\theta) d\theta
\end{aligned} \tag{A.6}$$

$$2\pi i^l J_l(z) = \int_{-\pi}^\pi exp[izcos(\theta)] exp(il\theta) d\theta \tag{A.7}$$

Combining Eq. A.5 and Eq. A.7 results in

$$= \sum_l exp(il\psi) \int_0^\infty f_l(r) 2\pi i^l J_l(2\pi\xi_r r) r dr \tag{A.8}$$

$$= 2\pi \sum_l i^l exp(il\psi) \int_0^\infty f_l(r) J_l(2\pi\xi_r r) r dr \tag{A.9}$$

$$= 2\pi \sum_l i^l exp(il\psi) \mathcal{H}_l[f_l(r)] \tag{A.10}$$

where $\mathcal{H}_l[f_l(r)]$ is the $l^{th}$ order Hankel transform of $f_l(r)$ [91, Eq. 10.22.76]. This formula

is useful for calculations in this thesis including the OTF and phase mask estimate for the half-ring PSF and for calculating the PSF of the azimuthal harmonic PSF.

The Fourier transform of a circular aperture is common and results in the diffraction limited PSF or Airy disk often discussed in this thesis. The aperture function is defined as

$$AP(r) = \begin{cases} 1 & r < R \\ 0 & otherwise \end{cases} \tag{A.11}$$

where $R$ is the radius of the aperture. The Fourier transform is calculated as a zero-order Hankel transform.

$$FT[AP(r)] = 2\pi\mathcal{H}_l[AP(r)] = 2\pi\int_0^R J_l(2\pi\xi_r r)rdr = 2\pi\frac{J_1(2\pi\xi_r R)}{2\pi\xi_r R} \tag{A.12}$$

# Appendix B

# Analytic Calculation of the Azimuthal Harmonic PSF

The goal of this work is to find the Fourier Transform, and in turn the PSF, of the azimuthal harmonic phase function with one term:

$$\Phi[r,\theta] = exp[iar^2 cos(n\theta)] \tag{B.1}$$

where $n$ is an odd integer, $r$ and $\theta$ are the radial and azimuthal coordinate, and $a$ is a constant.

Consider the circular harmonic decomposition of $\Phi[r,\theta]$ where

$$exp[iar^2 cos(n\theta)] = \sum_{j=-\infty}^{\infty} c_j(ar^2) exp(ij\theta). \tag{B.2}$$

and

$$c_j(ar^2) = \frac{1}{2\pi}\int_{-\pi}^{\pi} exp[iar^2 cos(n\theta)] exp[-ij\theta] d\theta. \tag{B.3}$$

By the Jacobi-Anger expansion ( [91, Sec. 10.12]), the values of $c_j$ may be expressed as

$$\begin{aligned} c_j(ar^2) &= \frac{1}{2\pi}\int_{\pi}^{\pi}\sum_{p=-\infty}^{\infty} i^p J_p[ar^2]e^{ipn\theta}e^{-ij\theta}d\theta \\ &= \frac{1}{2\pi}\sum_{p=-\infty}^{\infty} i^p J_p[ar^2]\int_{\pi}^{\pi} e^{i(pn-j)\theta}d\theta \\ &= \begin{cases} i^p J_p[ar^2] & j = np \\ 0 & otherwise \end{cases} \end{aligned} \tag{B.4}$$

Inserting Eq. B.4 into Eq. B.2 results in

$$exp[iar^2 cos(n\theta)] = \sum_{j=-\infty}^{\infty} i^j J_j[ar^2]exp(ijn\theta). \tag{B.5}$$

The PSF of an aperture with phase function defined by Eq. B.5 may be calculated by a Fourier transform as

$$\begin{aligned} FT\{AP(r)exp[iar^2cos(n\theta)]\} &= \int_0^1\int_{-\pi}^{\pi} e^{iar^2cos(n\theta)}e^{ik_r rcos(\theta-\psi)}rdrd\theta \\ &= \sum_{j=-\infty}^{\infty} i^j\int_0^1\int_{-\pi}^{\pi} J_j[ar^2]e^{ijn\theta}e^{ik_r rcos(\theta-\psi)}rdrd\theta \\ &= \sum_{j=-\infty}^{\infty} i^j\int_0^1 J_j[ar^2]G_j rdrd\theta. \end{aligned} \tag{B.6}$$

where $k_r = 2\pi\xi_r$, $AP(r)$ is a circular aperture function with radius normalized to 1, and

$$G_j = \int_{-\pi}^{\pi} e^{ijn\theta}e^{ik_r rcos(\theta-\psi)}d\theta. \tag{B.7}$$

Substituting $\beta = \theta - \psi$ in Eq. B.7 and once again using the Jacobi-Anger expansion results

in the following solution for $G_j$:

$$\begin{aligned} G_j &= e^{ijn\psi}\int_{-\pi}^{\pi} e^{ijn\beta}e^{ik_r r cos(\beta)}d\beta \\ &= e^{ijn\psi}\int_{-\pi}^{\pi} e^{ijn\beta}\sum_{p=-\infty}^{\infty} i^p J_p[k_r r]e^{ip\beta}d\beta \\ &= e^{ijn\psi}\sum_{p=-\infty}^{\infty} i^p J_p[k_r r]\int_{-\pi}^{\pi} e^{i(jn+p)\beta}d\beta \\ &= 2\pi i^{jn}e^{ijn\psi}J_{jn}[2\pi\xi_r] \end{aligned} \tag{B.8}$$

The Fourier Transform of the phase function may then be represented as

$$\begin{aligned} FT[AP(r)e^{iar^2cos(n\theta)}] &= \int_0^1\int_{-\pi}^{\pi} e^{iar^2cos(n\theta)}e^{ik_r r cos(\theta-\psi)}rdrd\theta \\ &= \sum_{j=-\infty}^{\infty} i^j\int_0^1 J_j[ar^2]G_j r dr \\ &= 2\pi\sum_{j=-\infty}^{\infty} i^{j(n+1)}e^{ijn\psi}\int_0^1 J_j[ar^2]J_{jn}[k_r r]rdr \\ &= 2\pi\int_0^1 J_0[ar^2]J_0[k_r r]rdr + 4\pi\sum_{j=1}^{\infty}(-1)^j cos(jn\psi)\int_0^1 J_j[ar^2]J_{jn}[k_r r]rdr \end{aligned} \tag{B.9}$$

The Hankel Transform may be calculated using the power series expansion of a Bessel function of the first kind [91, Eq. 10.2.2]

$$J_\nu(z) = (\tfrac{1}{2}z)^\nu\sum_{k=0}^{\infty}(-1)^k\frac{(\frac{1}{4}z^2)^k}{k!\Gamma(\nu+k+1)}. \tag{B.10}$$

The $J_j[ar^2]$ term may be expanded in Eq. B.9 resulting in

$$\begin{aligned} FT[e^{iar^2cos(n\theta)}] &= 2\pi \int_0^1 \sum_{l=0}^{\infty} \frac{(-1)^l(\frac{1}{4}ar^2)^l}{(l!)^2} J_0[k_r r] r dr + \\ & \quad 4\pi \sum_{j=1}^{\infty} (-1)^j cos(jn\psi) \int_0^1 (\frac{1}{2}ar^2)^j \sum_{l=0}^{\infty} \frac{(-1)^l(\frac{1}{4}ar^2)^l}{l!(j+l)!} J_{jn}[k_r r] r dr \\ &= 2\pi \sum_{l=0}^{\infty} \int_0^1 \frac{(-1)^l a^{2l} r^{4l}}{4^l (l!)^2} J_0[k_r r] r dr + \\ & \quad 4\pi \sum_{j=1}^{\infty} \sum_{l=0}^{\infty} cos(jn\psi) \int_0^1 \frac{(-1)^{l+j} a^{j+2l} r^{2j+4l+1}}{2^j 4^l l!(j+l)!} J_{jn}[k_r r] dr \end{aligned} \quad \text{(B.11)}$$

The integral may be calculated using [91, Eq. 10.22.10]

$$\begin{aligned} &\int_0^x t^{\mu} J_{\nu}(t)\, \mathrm{d}t = \\ &\qquad x^{\mu} \frac{\Gamma\left(\frac{1}{2}\nu + \frac{1}{2}\mu + \frac{1}{2}\right)}{\Gamma\left(\frac{1}{2}\nu - \frac{1}{2}\mu + \frac{1}{2}\right)} \times \sum_{k=0}^{\infty} \frac{(\nu + 2k + 1)\Gamma\left(\frac{1}{2}\nu - \frac{1}{2}\mu + \frac{1}{2} + k\right)}{\Gamma\left(\frac{1}{2}\nu + \frac{1}{2}\mu + \frac{3}{2} + k\right)} J_{\nu+2k+1}(x). \end{aligned} \quad \text{(B.12)}$$

Combining Eq. B.11 and B.12 results in the final solution for the PSF as:

$$\begin{aligned}
FT[AP(r)e^{iar^2cos(n\theta)}] &= 2\pi\sum_{l=0}^{\infty}\int_0^1 \frac{(-1)^l a^{2l} r^{4l}}{4^l (l!)^2} J_0[k_r r] r dr + \\
&\quad 4\pi\sum_{j=1}^{\infty}\sum_{l=0}^{\infty} cos(jn\psi)\int_0^1 \frac{(-1)^{l+j} a^{j+2l} r^{2j+4l+1}}{2^j 4^l l!(j+l)!} J_{jn}[k_r r] dr \\
&= 2\pi\sum_{l=0}^{\infty}\frac{a^{2l} k_r^{-(4l+2)}}{4^l (l!)^2}\int_0^{k_r} u^{4l+1} J_0(u)\, du + \\
&\quad 4\pi\sum_{j=1}^{\infty}\sum_{l=0}^{\infty}\frac{(-1)^j \cos(jn\psi) a^{j+2l} k_r^{-(2j+4l+2)}}{2^j 4^l l!(j+l)!}\int_0^{k_r} u^{2j+4l+1} J_{jn}(u)\, du \\
&= 2\pi\sum_{l=0}^{\infty}\sum_{p=0}^{\infty}\frac{(-1)^l a^{2l}}{4^l (l!)^2}\frac{\Gamma(p-2l)}{\Gamma(-2l)}\frac{(2p+1)(2l)!}{(2l+p+1)!}\frac{1}{k_r} J_{2p+1}(k_r) + \\
&\quad 4\pi\sum_{j=1}^{\infty}\sum_{l=0}^{\infty}\sum_{p=0}^{\infty}\frac{(-1)^{j+l} a^{j+2l}\cos(jn\psi)}{2^j 4^l l!(j+l)!}\frac{\Gamma\left(\frac{1}{2}j(n-2)-2l+p\right)}{\Gamma\left(\frac{1}{2}j(n-2)-2l\right)} \\
&\quad \times\frac{(jn+2p+1)\left(\frac{1}{2}j(n+1)+2l\right)!}{\left(\frac{1}{2}j(n+1)+2l+p+1\right)!}\frac{1}{k_r} J_{jn+2p+1}(k_r)\,.
\end{aligned}$$

As the value for $n$, $j$, $l$, and $p$ are all integers, the gamma function may be solved with the following relationships:

$$\Gamma[t] = (t-1)! \tag{B.13}$$

$$\Gamma[-t] = \infty \tag{B.14}$$

$$\Gamma[0] = \infty \tag{B.15}$$

$$\Gamma[1/2] = \sqrt{\pi}. \tag{B.16}$$

# Bibliography

[1] J. P. Geis. Directed energy weapons on the battlefield: A new vision for 2025. Technical Report ADA463429, Air War Coll Maxwell AFB AL, 2003.

[2] N. Bloembergen, C. K. N. Patel, P. Avizonis, R. G. Clem, A. Hertzberg, T. H. Johnson, T. Marshall, R. B. Miller, W. E. Morrow, E. E. Salpeter, A. M. Sessler, J. D. Sullivan, J. C. Wyant, A. Yariv, R. N. Zare, A. J. Glass, L. C. Hebel, G. E. Pake, M. M. May, W. K. Panofsky, A. L. Schawlow, C. H. Townes, and H. York. Report to the American Physical Society of the study group on science and technology of directed energy weapons. *Rev. Mod. Phys.*, 59:S1–S201, Jul 1987.

[3] V. Coffey. High-energy lasers: new advances in defense applications. *Optics and Photonics News*, 25(10):28–35, 2014.

[4] Lockheed martin to deliver laser weapon system to navy. https://news.lockheedmartin.com, Mar 2018. Lockheed Martin.

[5] S. McDonald. U.S. Navy to develop laser weapon that can 'destroy' small boats, hostile drones. *Newsweek*, Mar 2019.

[6] Gregory Foo, David M. Palacios, and Grover A. Swartzlander. Optical vortex coronagraph. *Opt. Lett.*, 30(24):3308–3310, Dec 2005.

[7] G. J Ruane and G. A Swartzlander. Optical vortex coronagraphy with an elliptical aperture. *Applied Optics*, 52(2):171–176, 2013.

[8] G. J Ruane, P. Kanburapa, J. Han, and G. A Swartzlander. Vortex-phase filtering technique for extracting spatial information from unresolved sources. *Applied Optics*, 53(20):4503–4508, 2014.

[9] G. Ritt, D. Walter, and B. Eberle. Research on laser protection: an overview of 20 years of activities at Fraunhofer IOSB. *Proc. SPIE*, 8896:88960G–88960G–15, 2013.

[10] G. Ritt, M. Koerber, D. Forster, and B. Eberle. Protection performance evaluation regarding imaging sensors hardened against laser dazzling. *Optical Engineering*, 54(5):053106, 2015.

[11] D. J. Hagan, S. Guha, E. W. Van Stryland, M. J. Soileau, and Y. Y. Wu. Self-protecting semiconductor optical limiters. *Opt. Lett.*, 13(4):315–317, Apr 1988.

[12] G. A. Swartzlander, B. L. Justus, A. L. Huston, A.J. Campillo, and C.T. Law. Characteristics of a low f-number broadband visible thermal optical limiter. *Journal of Nonlinear Optical Physics & Materials*, 02(04):577–611, 1993.

[13] B. L. Justus, A. J. Campillo, and A. L. Huston. Thermal-defocusing/scattering optical limiter. *Opt. Lett.*, 19(9):673–675, May 1994.

[14] J. W. Perry, K. Mansour, I. S. Lee, X. Wu, P. V. Bedworth, D. Ng C. Chen, S. R. Marder, P. Miles, T. Wada, M. Tian, and H. Sasabe. Organic optical limiter with a strong nonlinear absorptive response. *Science*, 273(5281):1533, Sep 13 1996.

[15] H-B. Lin, R. J. Tonucci, and A. J. Campillo. Two-dimensional photonic bandgap optical limiter in the visible. *Opt. Lett.*, 23(2):94–96, Jan 1998.

[16] J. Staromlynska, T. J. McKay, J. A. Bolger, and J. R. Davy. Evidence for broadband optical limiting in a pt:ethynyl compound. *J. Opt. Soc. Am. B*, 15(6):1731–1736, Jun 1998.

[17] I. C. Khoo, M. V. Wood, M. Y. Shih, and P. H. Chen. Extremely nonlinear photosensitive liquid crystals for image sensing and sensor protection. *Opt. Express*, 4(11):432–442, May 1999.

[18] V. P. Belousov, I. M. Belousova, E. A. Gavronskaya, V. A. Grigor'ev, O. B. Danilov, A. G. Kalintsev, N. G. Mironova, E. N. Sosnov, V. N. Zgonnik, and A. N. Ponomarev. Broadband optical limiters based on fullerene-containing media with a fast nonlinear response in the visible region. *J. Opt. Technol.*, 66(8):713, Aug 1999.

[19] D. I. Kovsh, S. Yang, D. J. Hagan, and E. W. Van Stryland. Nonlinear optical beam propagation for optical limiting. *Appl. Opt.*, 38(24):5168–5180, Aug 1999.

[20] L. Brzozowski and E. H. Sargent. Nonlinear distributed-feedback structures as passive optical limiters. *J. Opt. Soc. Am. B*, 17(8):1360–1365, Aug 2000.

[21] F. E. Hernández, S. Yang, E. W. Van Stryland, and D. J. Hagan. High-dynamic-range cascaded-focus optical limiter. *Opt. Lett.*, 25(16):1180–1182, Aug 2000.

[22] R. Lepkowicz, A. Kobyakov, D. J. Hagan, and E. W. Van Stryland. Picosecond optical limiting in reverse saturable absorbers: a theoretical and experimental study. *J. Opt. Soc. Am. B*, 19(1):94–101, Jan 2002.

[23] G. Contestabile, M. Presi, R. Proietti, N. Calabretta, and E. Ciaramella. A simple and low-power optical limiter for multi-ghz pulse trains. *Opt. Express*, 15(15):9849–9858, Jul 2007.

[24] J. Khoury, B. Haji-saeed, W. D. Goodhue, C. L. Woods, and J. Kierstead. Mems-based optical limiter. *Appl. Opt.*, 47(29):5468–5472, Oct 2008.

[25] I. M. Belousova, O. B. Danilov, and A. I. Sidorov. Nonlinear-optical laser-radiation limiters. *J. Opt. Technol.*, 76(4):223–233, Apr 2009.

[26] B. Haji-saeed, W. D. Goodhue, C. L. Woods, J. Kierstead, and J. Khoury. Optical-limiter mems dynamic range compression deconvolution. *Appl. Opt.*, 48(19):3771–3787, Jul 2009.

[27] M. Heinrich, F. Eilenberger, R. Keil, F. Dreisow, E. Suran, F. Louradour, A. Tünnermann, T. Pertsch, Stefan Nolte, and Alexander Szameit. Optical limiting and spectral stabilization in segmented photonic lattices. *Opt. Express*, 20(24):27299–27310, Nov 2012.

[28] W. T. Welford. Use of annular apertures to increase focal depth. *J. Opt. Soc. Am.*, 50(8):749–753, Aug 1960.

[29] M. Mino and Y. Okano. Improvement in the otf of a defocused optical system through the use of shaded apertures. *Appl. Opt.*, 10(10):2219–2225, Oct 1971.

[30] E. E. Fenimore. Coded aperture imaging: the modulation transfer function for uniformly redundant arrays. *Appl. Opt.*, 19(14):2465–2471, Jul 1980.

[31] S. R. Gottesman and E. E. Fenimore. New family of binary arrays for coded aperture imaging. *Appl. Opt.*, 28(20):4344–4352, Oct 1989.

[32] E. R. Dowski and W. T. Cathey. Extended depth of field through wave-front coding. *Appl. Opt.*, 34(11):1859–1866, Apr 1995.

[33] W. T. Cathey and E. R. Dowski. New paradigm for imaging systems. *Appl. Opt.*, 41(29):6080–6092, Oct 2002.

[34] G. Muyo and A. R. Harvey. Decomposition of the optical transfer function: wavefront coding imaging systems. *Opt. Lett.*, 30(20):2715–2717, Oct 2005.

[35] S. Chen, Z. Fan, H. Chang, and Z. Xu. Nonaxial strehl ratio of wavefront coding systems with a cubic phase mask. *Appl. Opt.*, 50(19):3337–3345, Jul 2011.

[36] Y. Y. Schechner, R. Piestun, and J. Shamir. Wave propagation with rotating intensity distributions. *Phys. Rev. E*, 54:R50–R53, Jul 1996.

[37] V. V. Kotlyar, V. A. Soifer, and S. N. Khonina. An algorithm for the generation of laser beams with longitudinal periodicity: Rotating images. *Journal of Modern Optics*, 44(7):1409–1416, 1997.

[38] S. R. P. Pavani and R. Piestun. High-efficiency rotating point spread functions. *Opt. Express*, 16(5):3484–3489, Mar 2008.

[39] S. R. P. Pavani, M. A. Thompson, J. S. Biteen, S. J. Lord, N. Liu, R. J. Twieg, R. Piestun, and W. E. Moerner. Three-dimensional, single-molecule fluorescence imaging beyond the diffraction limit by using a double-helix point spread function. *Proceedings of the National Academy of Sciences*, 106(9):2995–2999, 2009.

[40] S. Jia, J. C. Vaughan, and X. Zhuang. Isotropic three-dimensional super-resolution imaging with a self-bending point spread function. *Nature Photonics*, 8(4):302, 2014.

[41] Y. Shechtman, L. E. Weiss, A. S. Backer, M. Y. Lee, and W. E. Moerner. Multicolour localization microscopy by point-spread-function engineering. *Nature Photonics*, 10(9):590, 2016.

[42] S. N. Dixit, I. M. Thomas, B. W. Woods, A. J. Morgan, M. A. Henesian, P. J. Wegner, and H. T. Powell. Random phase plates for beam smoothing on the nova laser. *Appl. Opt.*, 32(14):2543–2554, May 1993.

[43] C. Oh and M. J. Escuti. Achromatic diffraction from polarization gratings with high efficiency. *Optics Letters*, 33(20):2287–2289, 2008.

[44] C. Dorrer. High-damage-threshold beam shaping using binary phase plates. *Opt. Lett.*, 34(15):2330–2332, Aug 2009.

[45] C. Dorrer, S. K.-H. Wei, P. Leung, M. Vargas, K. Wegman, J. Boulé, Z. Zhao, K. L. Marshall, and S. H. Chen. High-damage-threshold static laser beam shaping using optically patterned liquid-crystal devices. *Opt. Lett.*, 36(20):4035–4037, Oct 2011.

[46] E. Hasman, N. Davidson, and A. A. Friesem. Heterostructure multilevel binary optics. *Opt. Lett.*, 16(19):1460–1462, Oct 1991.

[47] N. Davidson, A. A. Friesem, and E. Hasman. Computer-generated relief gratings as space-variant polarization elements. *Opt. Lett.*, 17(21):1541–1543, Nov 1992.

[48] Z. Bomzon, V. Kleiner, and E. Hasman. Pancharatnam–berry phase in space-variant polarization-state manipulations with subwavelength gratings. *Opt. Lett.*, 26(18):1424–1426, Sep 2001.

[49] S. Banerji, M. Meem, A. Majumder, F. G. Vasquez, B. Sensale-Rodriguez, and R. Menon. Imaging with flat optics: metalenses or diffractive lenses? *Optica*, 6(6):805–810, Jun 2019.

[50] D. T. Nguyen, C. Meyers, T. D. Yee, N. A. Dudukovic, J. F. Destino, C. Zhu, E. B. Duoss, T. F. Baumann, T. Suratwala, J. E. Smay, and R. DyllaSpears. 3d-printed transparent glass. *Advanced Materials*, 29(26):1701181, 2017.

[51] C. Oh and M. J. Escuti. Achromatic diffraction from polarization gratings with high efficiency. *Opt. Lett.*, 33(20):2287–2289, Oct 2008.

[52] S. R. Nersisyan, N. V. Tabiryan, D. M. Steeves, and B. R. Kimball. Characterization of optically imprinted polarization gratings. *Appl. Opt.*, 48(21):4062–4067, Jul 2009.

[53] S. R. Nersisyan, N. V. Tabiryan, D. M. Steeves, and B. R. Kimball. The promise of diffractive waveplates. *Opt. Photon. News*, 21(3):40–45, Mar 2010.

[54] S. V. Serak, D. E. Roberts, J-Y. Hwang, S. R. Nersisyan, N. V. Tabiryan, T. J. Bunning, D. M. Steeves, and B. R. Kimball. Diffractive waveplate arrays. *J. Opt. Soc. Am. B*, 34(5):B56–B63, May 2017.

[55] C. Pfeiffer and A. Grbic. Metamaterial huygens' surfaces: Tailoring wave fronts with reflectionless sheets. *Phys. Rev. Lett.*, 110:197401, May 2013.

[56] L. De Sio, D. E. Roberts, Z. Liao, J. Hwang, N. Tabiryan, D. M. Steeves, and B. R. Kimball. Beam shaping diffractive wave plates [invited]. *Appl. Opt.*, 57(1):A118–A121, Jan 2018.

[57] John H. McLeod. The axicon: A new type of optical element. *J. Opt. Soc. Am.*, 44(8):592–597, Aug 1954.

[58] G. J. Ruane, G. A. Swartzlander, S. Slussarenko, L. Marrucci, and M. R. Dennis. Nodal areas in coherent beams. *Optica*, 2(2):147–150, Feb 2015.

[59] Rafael C. G. and R. E. Woods. *Digital image processing*. Upper Saddle River, NJ: Prentice Hall, 2012.

[60] J. M. Irvine. National imagery interpretability rating scales (NIIRS): overview and methodology. In *Airborne Reconnaissance XXI*, volume 3128, pages 93–104. International Society for Optics and Photonics, 1997.

[61] J. C. Leachtenauer, W. Malila, J. Irvine, L. Colburn, and N. Salvaggio. General image-quality equation: GIQE. *Appl. Opt.*, 36(32):8322–8328, Nov 1997.

[62] S. T. Thurman and J. R. Fienup. Application of the general image-quality equation to aberrated imagery. *Appl. Opt.*, 49(11):2132–2142, Apr 2010.

[63] J. Goodman. *Introduction to Fourier Optics*. McGraw-hill, 2008.

[64] R. T. Brigantic, M. C. Roggemann, K. W. Bauer, and B. M. Welsh. Image-quality metrics for characterizing adaptive optics system performance. *Appl. Opt.*, 36(26):6583–6593, Sep 1997.

[65] R. M. Herman and T. A. Wiggins. Production and uses of diffractionless beams. *J. Opt. Soc. Am. A*, 8(6):932–942, Jun 1991.

[66] L. Allen, M. W. Beijersbergen, R. J. C. Spreeuw, and J. P. Woerdman. Orbital angular momentum of light and the transformation of laguerre-gaussian laser modes. *Phys. Rev. A*, 45:8185–8189, Jun 1992.

[67] K. T. Gahagan and G. A. Swartzlander. Optical vortex trapping of particles. *Opt. Lett.*, 21(11):827–829, Jun 1996.

[68] Alison M. Yao and Miles J. Padgett. Orbital angular momentum: origins, behavior and applications. *Adv. Opt. Photon.*, 3(2):161–204, Jun 2011.

[69] D. G. Voelz. *Computational fourier optics: a MATLAB tutorial*. SPIE Press Bellingham, WA, 2011.

[70] R. G. Paxman, T. J. Schulz, and J. R. Fienup. Joint estimation of object and aberrations by using phase diversity. *JOSA A*, 9(7):1072–1085, 1992.

[71] C. Zhou, S. Lin, and S. Nayar. Coded aperture pairs for depth from defocus. In *2009 IEEE 12th International Conference on Computer Vision*, pages 325–332, Sept 2009.

[72] J. Li, C-H. Wen, S. Gauza, R. Lu, and S-T. Wu. Refractive indices of liquid crystals for display applications. *Journal of Display Technology*, 1(1):51–61, Sept 2005.

[73] Z. C. Zhang, Z. You, and D. P. Chu. Fundamentals of phase-only liquid crystal on silicon (LCOS) devices. *Light-Science and Applications*, 3(10):e213, 2014.

[74] Meadowlak spatial light modulators - reflective xy series. http://www.phototechnica.co.jp/wp-content/uploads/2016/12/SLM-XY512x512-Series-Reflective_2016.11_ph.pdf, 2016.

[75] Holoeye spatial light modulators. https://holoeye.com/spatial-light-modulators/.

[76] V. Arrizón, E. Carreón, and M. Testorf. Implementation of fourier array illuminators using pixelated SLM: efficiency limitations. *Optics Communications*, 160(4):207 – 213, 1999.

[77] G. Milewski, D. Engström, and J. Bengtsson. Diffractive optical elements designed for highly precise far-field generation in the presence of artifacts typical for pixelated spatial light modulators. *Appl. Opt.*, 46(1):95–105, Jan 2007.

[78] H. Zhang, J. Xie, J. Liu, and Y. Wang. Elimination of a zero-order beam induced by a pixelated spatial light modulator for holographic projection. *Appl. Opt.*, 48(30):5834–5841, Oct 2009.

[79] D. Palima and V. R. Daria. Holographic projection of arbitrary light patterns with a suppressed zero-order beam. *Appl. Opt.*, 46(20):4197–4201, Jul 2007.

[80] D. Palima and V. R. Daria. Effect of spurious diffraction orders in arbitrary multifoci patterns produced via phase-only holograms. *Appl. Opt.*, 45(26):6689–6693, Sep 2006.

[81] M. A. Vorontsov and V. P. Sivokon. Stochastic parallel-gradient-descent technique for high-resolution wave-front phase-distortion correction. *J. Opt. Soc. Am. A*, 15(10):2745–2758, Oct 1998.

[82] M. A. Vorontsov, G. W. Carhart, M. Cohen, and G. Cauwenberghs. Adaptive optics based on analog parallel stochastic optimization: analysis and experimental demonstration. *J. Opt. Soc. Am. A*, 17(8):1440–1453, Aug 2000.

[83] J. C. Lagarias, J. A. Reeds, M. H. Wright, and P. E. Wright. Convergence properties of the Nelder–Mead simplex method in low dimensions. *SIAM Journal on optimization*, 9(1):112–147, 1998.

[84] R. Storn and K. Price. Differential evolution–a simple and efficient heuristic for global optimization over continuous spaces. *Journal of global optimization*, 11(4):341–359, 1997.

[85] C. C. Olson, R. T. Schermer, and F. Bucholtz. Tailored optical force fields using evolutionary algorithms. *Opt. Express*, 19(19):18543–18557, Sep 2011.

[86] W. T. Cathey. Phase holograms, phase-only holograms, and kinoforms. *Appl. Opt.*, 9(6):1478–1479, Jun 1970.

[87] J. R. Fienup. Phase retrieval algorithms: a comparison. *Appl. Opt.*, 21(15):2758–2769, Aug 1982.

[88] R. W. Gerchberg. A practical algorithm for the determination of phase from image and diffraction plane pictures. *Optik*, 35:237–246, 1972.

[89] M. Bolcar. *Phase diversity for segmented and multi-aperture systems.* PhD thesis, University of Rochester, 2008.

[90] Schott AG. Optical glass data sheets. https://www.us.schott.com/advanced_optics, 2019.

[91] *NIST Digital Library of Mathematical Functions.* http://dlmf.nist.gov/, Release 1.0.23 of 2019-06-15. F. W. J. Olver, A. B. Olde Daalhuis, D. W. Lozier, B. I. Schneider, R. F. Boisvert, C. W. Clark, B. R. Miller and B. V. Saunders, eds.